2015

Xenopus DPPA2 is a Direct Inhibitor of Microtubule Polymerization Required for Nuclear Assembly

John Zhao Xue

XENOPUS DPPA2 IS A DIRECT INHIBITOR OF MICROTUBULE POLYMERIZATION REQUIRED FOR NUCLEAR ASSEMBLY

A Thesis Presented to the Faculty of

The Rockefeller University

In Partial Fulfillment of the Requirements for

The degree of Doctor of Philosophy

by

John Zhao Xue

June 2015

XENOPUS DPPA2 IS A DIRECT INHIBITOR OF MICROTUBULE POLYMERIZATION REQUIRED FOR NUCLEAR ASSEMBLY

John Z. Xue, Ph.D.

The Rockefeller University 2015

The eukaryotic nucleus mediates the genomic functions of information storage and gene expression, but must be completely rebuilt after every open mitosis as well as during fertilization. Nuclear abnormalities are observed in many tissue malignancies and congenital disorders, but the causes and effects of such pathologies remain poorly understood. Here we use cell-free *Xenopus* egg extracts to investigate the contribution of the DNA-binding protein Dppa2 to nuclear assembly. In Dppa2-depleted extracts, nuclei are small and deformed, assemble incomplete nuclear envelopes and fail DNA replication. We show that Dppa2 directly depolymerizes microtubules, and must be localized on DNA to tune local microtubule dynamics for proper nuclear assembly. In the absence of Dppa2, excess microtubules compromise nuclear shape, while ectopically abolishing microtubules retards nuclear expansion. Dppa2 can be bypassed with an appropriate dose oDppa2 nocodazole, but only during a narrow, defined time window. This reveals strict spatial and temporal demands for regulated microtubule dynamics during nuclear formation. We further study the effect of Dppa2 on dynamic microtubule growth reconstituted with purified tubulin, and find that Dppa2 stimulates microtubule catastrophe. This effect is dependent on GTP hydrolysis, and we explore the possibility that Dppa2 activates the intrinsic GTPase activity of microtubule polymers.

Acknowledgements

Thank you to Hiro, who has been in equal parts brilliant, patient, fastidious and humbling. You are generous with your time, and while I try to emulate your knack for spotting the iPhone 4 detail ('It changes everything'), I still have plenty of catching up to do. There is no doubt in my mind that I would be a lesser scientist under anyone else.

Cheers, Christian, the very model of a modern scientist. It's fair to say that I wouldn't know how to do any experiments without you having been around, and I learned mostly from you that all the different flavors of science are interesting. Thank you to Cristina, I think you and I agree on pretty much everything, and our tête-à-têtes made long flights and even longer experiments fly by. Thank you Dave for keeping the microscope room tidy (j/k). You get the big picture, never sweat (most of) the small stuff and can quote C. J. Cregg from memory. Jess for making me do a push-up on that dark day when I took your kickboxing class but then making up for it with cocktails. Chris for mortgage advice and a sunny "What's up" every morning. No thanks to Boo, for setting an impossible standard and spoiling Hiro for the schmuck students who had to follow her. I always look forward to the slide Mike opens lab meeting with. Simona to reminisce with about that college in East Anglia. Alex and Lisa were Platonic ideals of how a postdoc should know everything ever published, saved a great deal of time for the rest of us. By no means least, Adriana got more done in a day than I could in a week, and always bore my complaining with a smile. You rock.

Acknowledgements

Thank you to Eileen for the groundwork without which this thesis would just be Appendix D. I'm grateful to Abbe, Tommy and Matt for putting up with my so-called 'mentoring' skills; I note none of you stayed. I thank Yoshiaki Azuma, Mary Dasso, Rebecca Heald, Hiroshi Kimura, Satoru Mochida, Ryoma Ohi, Yuta Shimamoto and Dale Shumaker for reagents, Alison and Kaye for microscopy, and Sozanne for being a terrific collaborator.

I'm grateful to the Dean's Office, Dean Strickland, Emily, Cris, Kristen, Marta, Stephanie. Your hard work keeps us Number One. My Faculty Advisory Committee, Fred Cross and David Allis, has stuck with me these 7 years and thought up more than a few of the experiments in these pages for me to take credit for. This work was supported by The David Rockefeller Graduate Program and the National Institutes of Health (R01-GM075249).

My friends. Claire taught me much about the Opium War, Lei is the rare genius that never needs to show off. Radhika has been my role model from day one. Having Supawat around is great because he's so scary good at science, it makes you fish that paper back out of the trash. Miss the kebabs with Neel, Zeeshan, Sid and Harvir. Christine for Shostakovich Appreciation. Beer tastes better after sports with Pradeep, Alex, Dasha and Joe.

My brother Max taught me to cheer up. My parents subsidized my expenses and gave me a Cas9 plasmid. I don't say it often enough, but thank you.

Table of Contents

List of Figures

List of Figures

List of Tables

List of Abbreviations

BAF	barrier-to-autointegration factor
Cdk	cyclin-dependent kinase
ChIP	chromatin immunoprecipitation
CPC	chromosomal passenger complex
CSF	cytostatic factor
DCR	Dppa2/4 conserved region
Dppa2	developmental pluripotency associated 2
ES cell	embryonic stem cell
FISH	fluorescence in situ hybridization
FRAP	fluorescence recovery after photobleaching
GAP	GTPase-activating protein
GMPCPP	guanylyl-(α,β)-methylene-diphosphonate
GST	glutathione S transferase
INCENP	inner centromere protein
LBR	lamin B receptor
LINC	linker of nucleoskeleton and cytoskeleton
MAP	microtubule-associated protein
MBP	maltose-binding protein
MBT	mid-blastula transition
MCAK	mitotic centromere-associated kinesin
NPC	nuclear pore complex
Op18	oncoprotein 18
RCC1	regulation of chromosome condensation 1
RNAi	RNA interference
SAC	spindle assembly checkpoint
SAP	SAF (scaffold-attachment factor) A/B, Acinus and PIAS (protein inhibitor of activated STATs)
TIRF	total internal reflection fluorescence
TPX2	targeting protein for Xklp2 (Xenopus kinesin-like protein 2)

Chapter 1. Introduction

1.1. Natural variation in nuclear morphology

Eukaryotic genomes are packaged into nuclei, which shield chromosomes from physical stresses and simultaneously mediate the genomic functions of DNA replication, transcription and pre-mRNA processing (Figure 1-1). A striking diversity of nuclear morphologies is observed in nature, but only in rare cases do we understand how this variation is achieved or what function it serves. Abnormal nuclear morphology has long been associated with cellular aging and many disease states, but the role of nuclear abnormality in pathogenesis remains unclear.

Nuclear size

Nuclear size can vary greatly, even among closely related species such as *Xenopus laevis* and *Xenopus tropicalis*. While *X. laevis* erythrocytes have a nuclear volume of 10 μm^3, erythrocyte nuclei in *X. tropicalis* are three-fold smaller at 3 μm^3 (Horner and Macgregor, 1983). Generally speaking, nuclear size scales roughly with genome size, but this association is not necessarily causal. Although the nuclei of diploid *X. tropicalis* contain roughly half as much DNA as pseudotetraploid *X. laevis*, when *X. tropicalis* sperm are incubated in cytoplasmic extracts prepared from the larger *X. laevis* eggs, they swell to much larger sizes and are indistinguishable from *X. laevis* sperm (Levy and Heald, 2010). The reciprocal experiment gives an equivalent result, where *X. laevis* sperm assemble into much smaller nuclei in *X. tropicalis* egg extracts. It turns out that in *Xenopus* eggs and embryos, nuclear size is determined purely cytoplasmically by limiting concentrations of the nuclear transport factors importin α and Ntf2 (Levy and Heald, 2010).

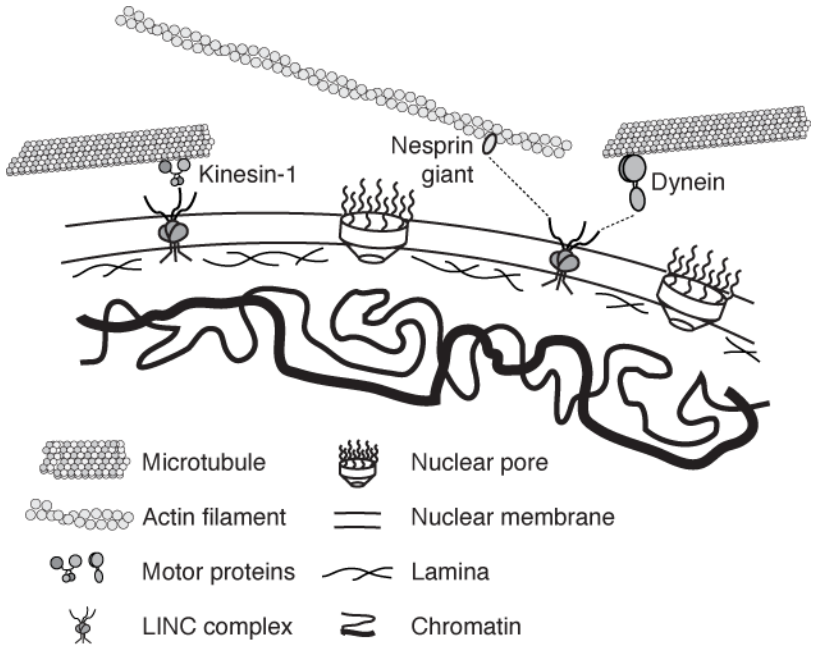

Figure 1-1. The nucleus, cytoskeleton and LINC complex

A double membrane segregates the nuclear interior from the cytoplasm, strengthened by the lamina network. Heterochromatin is associated with the nuclear periphery and euchromatin with the nucleoplasm, although highly expressed genes tend to reside near nuclear pore complexes. The LINC complex is a trimer of SUN and KASH domain proteins with the KASH peptide spanning the outer nuclear membrane (Sosa et al., 2012). KASH proteins such as the nesprins bind directly to actin cables and to microtubules through kinesin and dynein motors.

Depletion studies have shown that modulating rates of nuclear transport is a common means of regulating nuclear size (Gant et al., 1999; Jevtić et al., 2014). The best-studied cargos involved in this mechanism are the lamins, which form the lamina matrix that lends structural support to nuclear expansion. However, different cargos may be important in different contexts, for example lamin-null mouse embryonic stem (ES) cells do not show obvious nuclear size deficiencies (Kim et al., 2011). Similarly, an increase in nuclear size following depletion of the nucleoporin Nup188 is due to increased translocation of integral membrane proteins (Theerthagiri et al., 2010). In growing cells, nuclei tend to expand with cell volume and maintain a constant nuclear/ cytoplasmic (N/C) ratio. When this ratio is perturbed, for example by centrifugation of dividing fission yeast to yield daughter cells with different cell volumes, nuclear growth rates will self-correct until the normal N/C ratio is restored (Neumann and Nurse, 2007).

The nucleus is connected to the actin and microtubule cytoskeleton through a network of nuclear-membrane-spanning proteins containing SUN and KASH domains, collectively termed the linker of nucleoskeleton and cytoskeleton (LINC) complex (Figure 1-1). The LINC complex mediates nuclear migration (Luxton et al., 2010) and transduces force across the nuclear envelope, for instance harnessing microtubule-dependent forces to power meiotic chromosome movement (Yamamoto et al., 1999; Chikashige et al., 2006; Hiraoka and Dernburg, 2009; Sato et al., 2009; Wynne et al., 2012). This force transduction potential can also regulate nuclear morphology. Deletion of the actin-binding domain of the KASH protein Nesprin-2 Giant causes gross enlargement of epithelial nuclei, suggesting that actin attachment normally restricts nuclear size (Lüke et al., 2008).

Nuclear shape

The archetypal image of the nucleus is that of a smooth sphere or ovoid, and while largely true this does not apply to all cells. Unusual nuclear shapes are frequently the result of nuclear envelope pliability; for example, the absence of type-A lamins in ES cells leads to greater nuclear deformability (Pajerowski et al., 2007). Similarly, many white blood cells have large nuclei that occupy most of the cell volume and are frequently lobulated. In neutrophils, which like ES cells lack type-A lamins, deformation of the nucleus allows the cells to extravasate through tight tissue junctions (Rowat et al., 2013).

As with nuclear size, nuclear shape is also influenced by the cytoskeleton. This was clearly demonstrated in a study using HL-60 leukemia cells, which undergo granulocytic differentiation in response to retinoic acid. In the differentiation process, upregulation of lamin B receptor (LBR) causes nuclear lobulation, but lobulation is suppressed by the microtubule-depolymerizing drug nocodazole (Olins and Olins, 2004). In the *Drosophila* embryo, whose nuclei are spherical in the syncytial stage but elongate at the onset of cellularization, the shape change is similarly inhibited by nocodazole treatment (Brandt et al., 2006). There is also emerging evidence that actin inside the nucleus can polymerize, with implications for regulating nuclear shape and potentially cell invasiveness (Bohnsack et al., 2006; Navarro-Lérida et al., 2015).

Nuclear organization

The nuclear interior is highly organized, and spatial relocalization of genic loci can facilitate gene activation or repression in a variety of developmental contexts (Light et al., 2013; Harr et al., 2015). Improved resolution in chromatin immunoprecipitation

(ChIP) and proximity-based chromosome conformation capture methods has revealed the partitioning of chromatin into open and closed compartments, which have conserved boundaries and correlate with replication timing, epigenetic modifications and heterochromatin status (Filion et al., 2010; Pope et al., 2014). A number of terminally differentiated cell types display particularly striking nuclear organization patterns observable even under low-power light microscopy. In both rod photoreceptor cells and olfactory neurons, heterochromatin retracts from the nuclear periphery and aggregates in the center of the nucleus, due to silencing of LBR and/or lamin A/C. In rod cells this arrangement is proposed to convert nuclei into microlenses that reduce photon loss for vision in low light, while in olfactory neurons it enforces monoallelic expression of olfactory receptors by sequestering inactive alleles (Clowney et al., 2012; Eberhart et al., 2013).

Nuclear morphology in disease

Nuclear size, shape and organization frequently impact cellular function, and many diseases are associated with abnormal nuclear morphology. Nuclear abnormalities remain the primary pathological feature in cancer diagnosis (Jevtić et al., 2014). Mutations in nuclear envelope proteins underlie many congenital disorders, collectively termed ‘nuclear envelopathies’, especially the diverse muscular dystrophies, progerias and lipodystrophies caused by lamin mutations. Mouse and tissue culture models expressing mutant nuclear envelope genes show changes in histone modifications, DNA damage and signal transduction (Scaffidi and Misteli, 2006, 2008; Burke and Stewart, 2014). The tissue-specific nature of many nuclear envelopathies is striking given the ubiquitous expression of these proteins. A large fraction of laminopathies afflicts skeletal and

cardiac muscle, possibly because weakened nuclei are more easily damaged by tissue shear stress, and also fail to respond to mechanotransduction cues (Davidson and Lammerding, 2013). Similarly, lipodystrophies afflict adipose tissues which express relatively low levels of lamin A, rendering nuclei more susceptible to deformation.

An unrelated class of nuclear abnormalities, namely micronuclei, can arise from errors in mitotic division. Cells arrested in mitosis with nocodazole cannot form kinetochore-microtubule attachments, and once nocodazole is washed out a fraction of chromosomes will fail to achieve proper amphitelic attachment prior to anaphase. This results in lagging chromosomes, which are slower to decondense and go on to assemble defective nuclear envelopes (Afonso et al., 2014). Lagging chromosomes that are not resorbed into the primary nucleus end up as isolated micronuclei, which display DNA replication errors and can be a source of DNA breaks and genomic instability (Crasta et al., 2012; Hatch et al., 2013).

1.2. Microtubule and chromosome dynamics during cell division

During open mitosis the dismantling and reassembly of the nucleus offers an opportunity to reshape nuclear architecture. For example, in cancer cells a single mitosis is sufficient to reshuffle the contacts between genomic loci and the nuclear envelope (Kind et al., 2013), which is accelerated by epigenetic instability in these cells (Harr et al., 2015). Chromosomes are subjected to strong spindle forces that drive their segregation; direct measurements in grasshopper cells estimated each kinetochore to experience a stall force of 10-50 pN (Nicklas, 1983). These forces are sufficient to break dicentric chromosomes formed during so-called ‘breakage-fusion-bridge’ cycles, which start upon deprotection of a chromosome end due to erosion or loss of one if its telomeres. Replication of this

chromosome produces a pair of deprotected sister chromatids, which fuse end-to-end through non-homologous end joining. The dicentric fusion chromosome will attach to both spindle poles in metaphase, and forms a bridge across the cleavage plane that is stretched and eventually broken in anaphase. This distributes a deprotected chromosome to each daughter cell, frequently containing unbalanced translocations, and starts a new breakage-fusion-bridge cycle (Gisselsson et al., 2000). These DNA breaks are particularly deleterious since DNA damage occurring during mitosis is not repaired efficiently (Giunta et al., 2010; Orthwein et al., 2014). Until nuclear assembly is complete, chromosomes are vulnerable to both environmental insult and the mitotic apparatus.

Mitotic control of microtubule assembly

Upon entry into M phase, global microtubule dynamics are increased by the activity of cyclin-dependent kinase 1 (Cdk1), which promotes catastrophe and sets an upper limit on microtubule length (Verde et al., 1990; Belmont et al., 1990). Spindle microtubules are typically nucleated from centrosomes, but this is not an essential requirement (Khodjakov et al., 2000; Basto et al., 2006; Courtois et al., 2012; Walczak and Heald, 2008), and a spindle can self-organize around DNA-coated beads in the absence of both centrosomes and kinetochores (Heald et al., 1996; Gaetz et al., 2006). To accomplish this, chromatin activates two spindle assembly pathways, namely the RanGTP and the chromosomal passenger complex (CPC) pathways. RanGTP is generated on chromatin by RCC1 (regulation of chromosome condensation 1), which is bound to nucleosomes and activates nucleotide exchange by the small G protein Ran (Nemergut et al., 2001; Kaláb et al., 2002; Makde et al., 2010; Kaláb and Heald, 2008). RanGTP liberates spindle assembly

factors such as TPX2 (targeting protein for Xklp2) and NuMA (nuclear mitotic apparatus protein) from repression by importins (Gruss et al., 2001; Nachury et al., 2001; Wiese et al., 2001). The CPC is a complex, composed of INCENP (inner centromere protein), Survivin, Dasra/Borealin and the kinase Aurora B, and is recruited to chromosomes during mitosis by binding of Survivin to the phosphorylated histone H3 tail (Wang et al., 2010; Kelly et al., 2010; Yamagishi et al., 2010). Aurora B activity is stimulated by enrichment on chromatin, and suppresses the microtubule destabilizing factors MCAK (mitotic centromere-associated kinesin) and Op18 (oncoprotein 18; (Sampath et al., 2004; Gadea and Ruderman, 2006; Kelly et al., 2007). These pathways confer spatial specificity to spindle assembly by limiting microtubule polymerization to the vicinity of microtubules. Spindle morphology is then further shaped by the collaborative action of motor proteins and microtubule crosslinkers (Gaetz et al., 2006; Loughlin et al., 2010).

Nuclear assembly at mitotic exit

Once chromosome segregation is complete, spindle assembly signals are extinguished. A number of spindle assembly factors – including TPX2, HURP (hepatoma upregulated protein) and NuSAP (nucleolar and spindle-associated protein) – are degraded by the anaphase-promoting complex (Song and Rape, 2010; Song et al., 2014), while mitotic phosphorylation is removed by phosphatase activity (Wurzenberger and Gerlich, 2011). Phosphatases directly promote nuclear assembly by dephosphorylating nuclear envelope and nuclear pore complex (NPC) proteins (Laurell et al., 2011; Asencio et al., 2012). Similar to its role in spindle assembly, Ran promotes nuclear assembly by relieving the inhibitory effect of importins, and Ran-coated beads can assemble functional nuclear envelopes with NPCs (Zhang and Clarke, 2000; Hetzer et al., 2000; Walther et al., 2003b;

Harel et al., 2003b). In conjunction with Ran, the nucleoporin ELYS (embryonic large molecule derived from yolk sac) nucleates assembly of the ~60 MDa NPC, and is recruited to chromosomes by direct interaction with nucleosomes (Fernandez and Piano, 2006; Franz et al., 2007; Inoue and Zhang, 2014; Zierhut et al., 2014). In contrast, the CPC inhibits chromosome decondensation and consequently nuclear formation, until it is removed from chromatin in late anaphase and relocalizes to the spindle midzone (Mora-Bermúdez et al., 2007; Ramadan et al., 2007; Kelly et al., 2010). Missegregated chromosomes that lag near the spindle equator are therefore exposed to high CPC activity and subject to delayed nuclear reformation (Afonso et al., 2014).

Spindle microtubules are disassembled at the same time as nuclear assembly begins (Figure 1-2A), and there is evidence that the former can interfere with the latter. Regions of high microtubule density obstruct the recruitment of inner membrane proteins, for example LBR is initially excluded by spindle fibers. As spindle microtubules are disassembled LBR is recruited to the poleward-facing surface of chromatin, while it remains excluded from the equator-facing surface by dense midzone microtubules (Chaudhary and Courvalin, 1993). Nuclear membranes are contiguous with the endoplasmic reticulum (ER), and the ER marker Sec61β shows an identical exclusion by microtubules, while membrane recruitment is accelerated by nocodazole treatment (Lu et al., 2011). On the other hand, the nuclear membrane protein barrier-to-autointegration factor (BAF) is not excluded by bulk microtubules (Haraguchi et al., 2008), possibly because its strong DNA-binding activity is able to overcome passive exclusion. Nonetheless, examination by electron microscopy still revealed gaps in the nascent BAF envelope occupied by microtubules (Haraguchi et al., 2008). In addition to presenting a

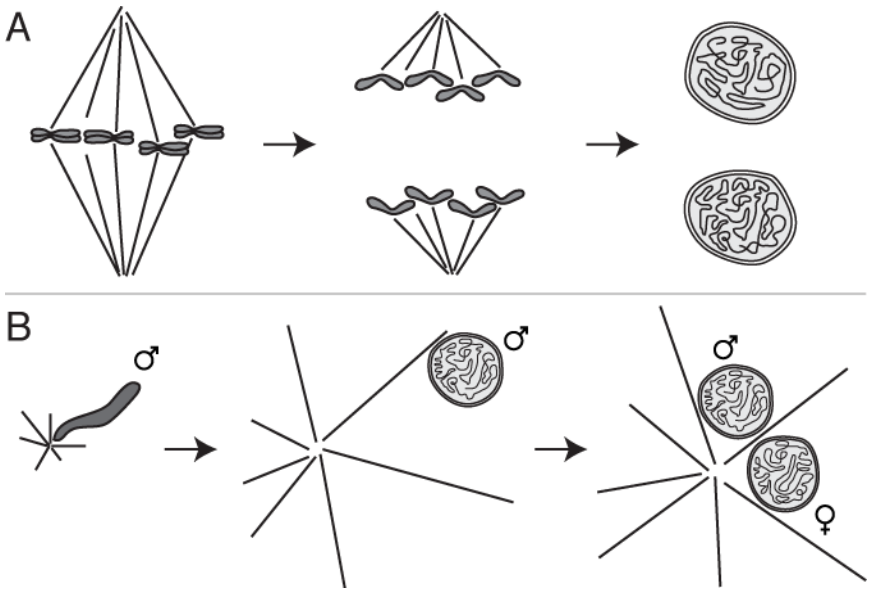

Figure 1-2. Nuclear assembly during mitosis and fertilization

(A) During mitotic exit spindle disassembly is coordinated with chromosome decondensation and nuclear envelope formation. During fertilization completion of female meiosis II follows largely the same events, with disassembly of the meiotic spindle and assembly of the maternal pronucleus; the only major difference is that one meiotic daughter cell is extruded as a polar body (not pictured).

(B) Fertilization also requires the dramatic conversion of compact sperm chromatin into decondensed spherical pronuclei. Concomitantly, astral microtubules nucleated from sperm centrosomes capture both sperm and egg pronuclei and transport them toward one another at the center of the egg. ♂, sperm chromosomes and pronucleus, ♀, female pronucleus.

physical obstacle to nuclear envelope closure, microtubule- and motor protein-dependent forces may damage nascent nuclei. Such forces are important during nuclear envelope breakdown at mitotic entry, when dynein binds and contributes to tearing of the nuclear envelope (Beaudouin et al., 2002; Salina et al., 2002). Membranes are then quickly cleared away from mitotic chromosomes by microtubule-binding transmembrane proteins, including SUN1/2 and REEP3/4 (Schlaitz et al., 2013; Turgay et al., 2014).

Conversely, some motor proteins positively promote nuclear assembly, for example the chromokinesin Kid which maintains compaction of the anaphase/telophase chromosome mass (Ohsugi et al., 2008). Loss of Kid activity causes chromosomes to separate, resulting in multinucleated daughter cells. The ER membranes that form the nuclear envelope are also shaped by microtubules. ER tubules can attach to the sides and tips of moving microtubules, as well as move relative to microtubules through the action of motor proteins (Waterman-Storer and Salmon, 1998; Wang et al., 2013). Microtubules may therefore be important for delivering membranes to telophase chromosomes during nuclear assembly. A similar microtubule-dependent mechanism is thought to deliver nucleoporins to nascent nuclei (Ewald et al., 2001). Emerging evidence suggests that interactions between membranes and microtubules are tuned in a cell-cycle-dependent manner. Interactions between dynein and ER membranes are suppressed in mitosis by phosphorylation of the dynein light intermediate chain (Niclas et al., 1996). Similarly, the transmembrane protein STIM1 binds the microtubule tip-tracking protein EB1 (end-binding protein 1) to direct ER growth along microtubule tracks, but this interaction is disrupted during mitosis by phosphorylation of STIM1 to prevent membranes invading the spindle (Grigoriev et al., 2008; Smyth et al., 2012).

Fertilization and pronuclear assembly

A specialized version of nuclear assembly takes place during fertilization. In vertebrate animals, mature egg cells are arrested in metaphase of meiosis II. Mature sperm are the products of a complex set of reactions that take place during spermatogenesis, in which sperm nuclei adopt highly specific morphologies and histones on sperm DNA are widely replaced first by transition proteins and then by protamines (Wright, 1999; Jenkins and Carrell, 2012). Protamines promote hypercompaction of sperm chromatin due to their highly charged surfaces and capacity for extensive disulfide bonding. When fertilization occurs, sperm chromatin is decompacted and protamines are exchanged for egg histones. Simultaneously, a calcium wave releases the egg into interphase (Reber et al., 2008). Both sperm and egg haploid genomes then assemble into pronuclei (Figure 1-1B). This process is essentially the same as nuclear assembly following mitotic chromosome segregation, involving chromosome decondensation, membrane recruitment and nuclear pore complex assembly.

Fertilization is also accompanied by dramatic cytoskeletal rearrangements. The haploid female meiotic spindle is disassembled in the same manner as mitotic spindles (Figure 1-2A). Meanwhile, the sperm nucleus is associated with a centrosome which rapidly nucleates a large microtubule aster, responsible for capturing both male and female pronuclei and transporting them to meet each other in the center of the egg (Figure 1-2B). In the giant *X. laevis* egg, this aster must span a millimeter-scale distance (Wühr et al., 2009; Mitchison et al., 2012), with a size and density that could perturb nuclear assembly if its dynamics are not tightly regulated.

Nuclear assembly in the early embryo

The cell cycle in embryonic systems can differ markedly from that in somatic cells. Mammalian ES cells display shortened gap phases and constitutive activation of E2F target genes, and more than half of each cell cycle is devoted to S phase (Stead et al., 2002). The situation is even more extreme in the early embryos of *Xenopus*, *Danio* and *Drosophila*, which dispense completely with gap phases and essentially alternate between M and S phases (Murray and Kirschner, 1989; Edgar and Datar, 1996; Yarden and Geiger, 1996). These cycles take place under the control of maternal proteins stockpiled in the egg prior to fertilization, and obviate the need for zygotic transcription until the mid-blastula transition (MBT). In particular, the first 13 divisions of the *Drosophila* embryo each take less than 10 minutes to complete, driven by high levels of maternal Cdc25 (Edgar and Datar, 1996; Di Talia et al., 2013). We speculate that these rapid cell cycles may also be facilitated by specific adaptations during mitosis. The early *Drosophila* embryo is syncytial, eliminating the cortical and plasma membrane remodeling that accompany cytokinesis. *Xenopus* and *Danio* embryos have a different adaptation, where nuclear envelope assembly begins before chromosome segregation is complete, enclosing each telophase chromosome inside a micronucleus known as a karyomere. Karyomeres will eventually fuse into a single primary nucleus, but in the meantime allow DNA replication to start early, shortening the time needed until the next M phase (Richards, 1917; Lemaitre et al., 1998; Abrams et al., 2012).

The *Xenopus* egg extract system

Cell-free extracts can be prepared from unfertilized *Xenopus laevis* eggs by centrifugation, isolating the cytosolic fraction with minimal dilution (Murray, 1991; Hartl

et al., 1994; Groen et al., 2011). In the presence of calcium-chelating agents, this extract retains cytostatic factor (CSF)-mediated metaphase arrest (Watanabe et al., 1991). Adding excess calcium together with exogenous DNA, in the form of demembranated sperm, plasmid or phage DNA, mimics fertilization and releases extracts into interphase. This recapitulates nuclear and microtubule aster assembly, and has been a key source of mechanistic insights into the nuclear assembly process (Lohka and Masui, 1983; Forbes et al., 1983).

Among the advantages of *Xenopus* egg extracts is precise control of the cell cycle, since extracts can be arrested at defined cell cycle stages and allow highly synchronized nuclear assembly. Their cell-free nature allows precise titration of specific proteins, which can be immunodepleted with antibodies and introduced at known concentrations more predictably than through transfection and RNA interference (RNAi). This is especially useful for essential or toxic proteins, whose levels cannot be easily modulated in cultured cells or living organisms.

1.3. Regulation of microtubule polymerization

Dynamic instability of microtubules

Tubulin cannot be properly folded in bacteria (Gao et al., 1993) and is highly toxic when overexpressed in eukaryotic cells (Johnson et al., 2011). The study of tubulin biochemistry has therefore largely relied on native tubulin obtained from animal brain homogenates by cycles of polymerization and depolymerization, followed by removal of microtubule-associated proteins (MAPs) by ion exchange chromatography (Borisy et al., 1975; Murphy and Borisy, 1975). Microtubules interconvert between growing and shrinking states at their linear ends (Figure 1-3), even when the ensemble population of

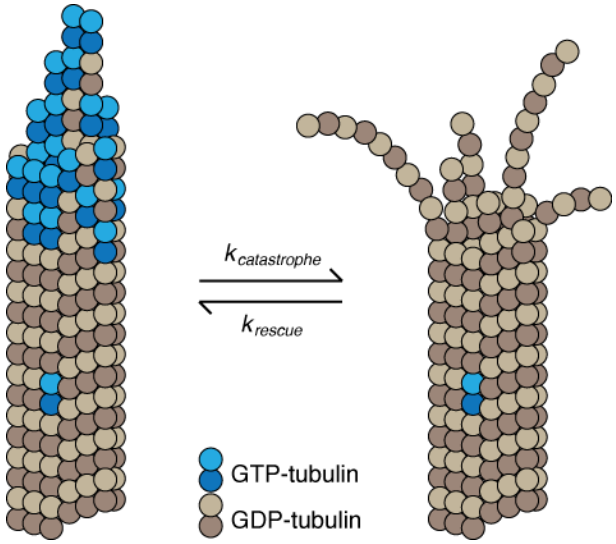

Figure 1-3. Dynamic instability of microtubules

GTP-tubulin is incorporated at growing microtubule ends, forming a stabilizing cap that protects against catastrophe. GTP is hydrolyzed in the microtubule lattice, and depolymerization takes place when the GTP cap is lost.

microtubules is polymerizing, a property termed ‘dynamic instability’ (Mitchison and Kirschner, 1984a, 1984b; Horio and Hotani, 1986). This behavior is unique among polymers, and has thus far only been observed in eukaryotic tubulins and the bacterial actin homolog ParM (Garner et al., 2004), and notably not eukaryotic actin.

The length distribution of a population of microtubules is predicted by four empirical parameters, namely speed of microtubule growth, speed of microtubule shrinkage, frequency of converting from shrinking to growing (‘rescue’ events) and frequency of converting from growing to shrinking (‘catastrophe’). Because tubulin monomers are obligate heterodimers of α-tubulin and β-tubulin, the linear microtubule polymer has polarity. The ‘plus’ end, where β-tubulin is exposed, polymerizes more rapidly and displays higher rates of rescue and catastrophe. At steady state, this difference produces a net addition of tubulin monomers at the plus end and net loss at the minus end, giving rise to ‘treadmilling’ as monomers lost from the minus end are reincorporated at the plus end (Margolis and Wilson, 1981; Rodionov and Borisy, 1997).

The GTP cap model

The energy required for dynamic instability is derived from GTP hydrolysis. Although both α- and β-tubulin bind GTP, nucleotide is only exchanged at the ‘E’ (exchangeable) site on β-tubulin, and assembly of one mole of α/β-tubulin heterodimer is associated with hydrolysis of one mole of GTP (MacNeal and Purich, 1978). When tubulin is polymerized in the presence of a non-hydrolyzable analog of GTP, guanylyl-(α,β)-methylene-diphosphonate (GMPCPP), microtubule growth occurs at normal rates but catastrophe is abolished (Hyman et al., 1992). GTP-tubulin in the microtubule lattice is

therefore a stabilizing influence, and catastrophe only takes place once GTP is hydrolyzed to GDP (Figure 1-2).

Because GTP hydrolysis occurs in the microtubule lattice (MacNeal and Purich, 1978), the highest concentration of GTP-tubulin is found in the growing tip, while the core of the lattice contain GDP. An analogous ATP cap is found in actin filaments (Korn et al., 1987). Microtubules are hollow tubes comprised of 13 protofilaments, each a linear array of tubulin monomers arranged head-to-tail (Figure 1-3). The conformation of GTP-tubulin favors straight protofilaments, whereas GDP-tubulin has weaker lateral contacts and promotes protofilament curvature (Wang and Nogales, 2005; Alushin et al., 2014). Thus loss of the GTP cap promotes depolymerization. This was elegantly demonstrated by using ultraviolet lasers to sever microtubules at core regions, revealing GDP-capped plus ends that then immediately underwent catastrophe and depolymerized rapidly (Walker et al., 1989; Tran et al., 1997). In addition, GTP hydrolysis in the microtubule lattice is incomplete, leaving behind GTP remnants in the microtubule core that act as seed regions for rescue events during microtubule shrinkage (Dimitrov et al., 2008; Tropini et al., 2012).

Regulators of microtubule dynamics

The dynamics of purified tubulin can be vastly altered by MAPs that promote or suppress polymerization (Murphy and Borisy, 1975; Kinoshita et al., 2001), and microtubule dynamics in vivo represent the sum of many competing regulatory activities. A non-exhaustive list of microtubule dynamics regulators is given in Table 1-1.

Rates of microtubule growth and rescue increase with tubulin concentration while catastrophe rate increases (Walker et al., 1988), and so microtubule regulators such as the

Table 1-1. Regulators of microtubule dynamics

Mechanism	Effect on MT dynamics	Examples
Sequestering free tubulin, bending protofilaments	Promote catastrophe	Op18/stathmin (Jourdain et al., 1997; Ravelli et al., 2004), kinesin-13/MCAK (Desai et al., 1999; Moores et al., 2002)
Delivering tubulin to microtubule ends, stabilizing transition state during growth	Increase growth rate, decrease catastrophe and rescue frequencies	XMAP215 (Brouhard et al., 2008)
Tip-tracking microtubule stabilizers	Suppress catastrophe	EB1, EB3 (Komarova et al., 2009), adenomatous polyposis coli (Kita, 2006)
Tip-tracking microtubule destabilizers	Reduce growth rate, promote catastrophe	Kinesin-8 (Gupta et al., 2006; Varga et al., 2006)
Severing enzymes		Katanin (Hartman et al., 1998), translational elongation factor 1 α (Shiina et al., 1994), spastin (Evans et al., 2005; Roll-Mecak and Vale, 2005)

stathmin family that sequester tubulin heterodimers will inhibit microtubule assembly (Jourdain et al., 1997; Ravelli et al., 2004). On the other hand, the microtubule polymerase XMAP215 binds tubulin heterodimers but delivers them to microtubule ends, catalyzing microtubule growth (Brouhard et al., 2008). Microtubule-severing enzymes such as katanin break microtubules at internal sites, creating a new plus and minus end with each turnover (Hartman et al., 1998). Other microtubule-binding proteins may stabilize particular conformations and transition states to promote polymerization or depolymerization. Both stathmins and kinesin-13 motor proteins introduce curvature into protofilaments, increasing catastrophe frequency (Ravelli et al., 2004; Moores et al., 2002). Notably, while microtubules assembled from purified tubulin are far less dynamic than microtubules in vivo, addition of a single KinI motor (XKCM1) together with the microtubule polymerase XMAP215 is sufficient to confer physiological rates of microtubule assembly and dynamics (Kinoshita et al., 2001).

1.4. Expression and function of Dppa2

Identification of *Xenopus* Dppa2 as a regulator of nuclear assembly

Developmental pluripotency associated 2 (Dppa2), was identified in the Funabiki lab by Eileen M. Woo and Lisa Postow from independent proteomic screens for DNA-binding proteins in *Xenopus* egg extracts (Postow et al., 2008; Woo, 2010). Further characterization by Eileen Woo revealed that *Xenopus* Dppa2 localizes uniformly to chromatin in both interphase and metaphase, and is SUMOylated upon binding to DNA in a manner dependent on the SUMO E3 ligase PIASy. Overexpression experiments found that a ten-fold excess of Dppa2 abolishes metaphase spindle microtubules, while

depletion of Dppa2 resulted in assembly of abnormal, misshapen nuclei (Woo, 2010). These observations formed the starting point for the results described in this thesis.

Dppa2 is a poorly-described protein expressed exclusively in embryonic cells

Dppa2, also known as *embryonic stem cell-associated transcript 15-2* (*ECAT15-2*) and *embryo-cancer sequence A* (*ECSA*), is a vertebrate-specific gene originally identified from its restricted expression in the mouse embryo and pluripotent cells (Bortvin et al., 2003). The Dppa2 protein contains a DNA-binding domain known as the SAP (SAF-A/B, Acinus and PIAS) motif (Aravind and Koonin, 2000; Suzuki et al., 2009). In mammals, Dppa2 is closely linked to a paralog Dppa4 (Maldonado-Saldivia et al., 2007), and the two genes also share homology in their C termini, termed the Dppa2/4 conserved region (DCR; Figure 1-4). However, only a single Dppa2 ortholog is found in amphibian, reptile and marsupial lineages (Siegel et al., 2009), suggesting that the duplication event leading to the presence of both Dppa2 and Dppa4 in mammals occurred after the divergence between mammals and other vertebrate lineages.

Relatively little is known about the function of Dppa2 or its relatives in any lineage, although it is frequently used as a marker for pluripotency. RNAi-mediated depletion experiments suggest that mammalian Dppa2 and Dppa4 contribute to self-renewal in embryonic stem (ES) cells (Ivanova et al., 2006; Du et al., 2010). Dppa2 was also reported to act as a reprogramming factor in the generation of induced pluripotent stem cells (Buganim et al., 2012). Both overexpression and morpholino-mediated knockdown of *Xenopus* Dppa2 resulted in abnormal development and embryonic lethality (Siegel et al., 2009). In mice, Dppa2 and Dppa4 double knockout embryos can survive

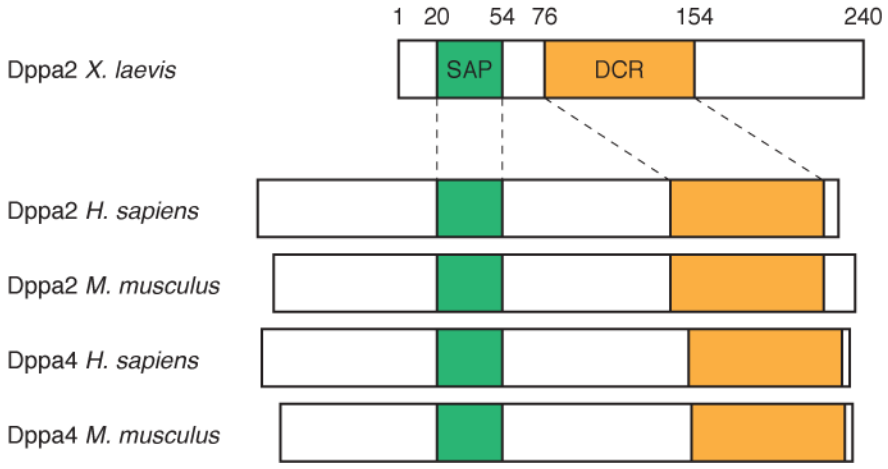

Figure 1-4. Domain structure of Dppa2

Alignment of *Xenopus laevis* Dppa2 drawn to scale against Dppa2 and Dppa4 in *Homo sapiens* and *Mus musculus*.

until birth, at which time they die from skeletal or respiratory defects, although neither Dppa2 nor Dppa4 is detectable in skeletal or lung tissues (Madan et al., 2009; Nakamura et al., 2011). It was therefore postulated that mammalian Dppa2 and Dppa4 regulate embryonic development by controlling early cell differentiation programs. Consistent with this hypothesis, Dppa2-knockout ES cells showed increased DNA methylation at the promoters of homeobox transcription factors, and Dppa2 was found at these loci by ChIP, suggesting that Dppa2 could act as a transcriptional activator (Nakamura et al., 2011).

Dppa2 is also one of a number of pluripotency-associated genes that are reactivated in cancers (Feinberg et al., 2006), hence one its alternative names *embryo-cancer sequence A*. In a panel of primary tumor samples, Dppa2 was detected in melanoma, follicular lymphoma, mesothelioma and 30% of non-small cell lung carcinomas (John et al., 2008). Moreover, overexpression of either Dppa2 or Dppa4 was sufficient to transform human tissue culture cells grown in soft agar or transplanted into mouse xenograft models (Tung et al., 2013). In the latter study, the oncogenic activity of Dppa2 depended partially on both its SAP and DCR motifs.

Although Dppa2 has been localized to specific genomic loci by ChIP (Nakamura et al., 2011), the SAP domain can also bind DNA non-specifically (Aravind and Koonin, 2000). In vitro studies performed with recombinant Dppa4 protein found that while its SAP motif could bind plasmid DNA directly, its C terminus containing the DCR motif interacted with core histones (Masaki et al., 2010). Both domains were required for stable association with chromatin, and fluorescence recovery after photobloeaching (FRAP) experiments found Dppa4 to have similar binding kinetics to chromatin as linker histones (Masaki et al., 2010).

Chapter 2. Dppa2 is required for nuclear assembly and inhibits microtubule polymerization

2.1. Nuclear assembly in *Xenopus* egg extracts

At the transition from M phase to interphase, chromosomes switch from driving microtubule assembly to promoting nuclear formation. First, RanGTP changes targets from spindle assembly factors to nuclear envelope and pore proteins (Zhang and Clarke, 2000; Hetzer et al., 2000; Walther et al., 2003b; Harel et al., 2003b). Second, CPC-dependent microtubule assembly and chromosome compaction are silenced by removal of the CPC from chromosomes (Ramadan et al., 2007; Kelly et al., 2010; Afonso et al., 2014). Third, chromatin directly recruits ER membranes and nucleoporins (Anderson and Hetzer, 2007; Inoue and Zhang, 2014; Zierhut et al., 2014). Much is now known about the mechanisms of each of these steps, but the spatial and temporal coupling between the large-scale cellular reactions of spindle assembly and nuclear formation is still poorly understood. The specialized processes of fertilization and pronuclear formation have received particularly little attention. We set out therefore to investigate male pronuclear assembly and sperm aster dynamics using *Xenopus* egg extracts.

Our typical pronuclear assembly assay was performed by adding demembranated sperm to CSF-arrested metaphase extracts together with calcium, mimicking fertilization. Sperm bring a limited complement of proteins, and rely on proteins stored in egg cytosol for microtubule and nuclear envelope assembly. We attempted to visualize these processes by live imaging, using fluorescently-labeled tubulin and lipophilic membrane dyes. Unfortunately, the dyes bleached rapidly and their signals were not well resolved (Figure 2-1A). However, we did observe that the dense microtubules of the sperm aster

Figure 2-1. Live imaging of nuclear assembly in *Xenopus* egg extracts

(A) Live imaging of membranes. 500 sperm nuclei were added per microliter of CSF-arrested egg extract together with 0.3 mM $CaCl_2$. After 4 min incubation at 20 °C, 4 μl of the nuclear assembly reaction was squashed under an 18×18 mm coverslip and observed at room temperature under 20× objective. DNA was visualized by inclusion of Hoechest 33342 (0.5 μg/ml; blue), membranes with 3,3'-dihexyloxacarbocyanine iodide ($DiOC_6$; 1 μg/ml; green) and microtubules with rhodamine-labeled bovine tubulin (0.5 μM; red).

(B) Live imaging of NPC assembly. Experiment performed as in (A), but visualizing nuclear envelopes using an antibody recognizing phenylalanine-glycine repeat nucleoporins (mAb414; 10 μg/ml) labeled with Alexa 488 succinimidyl ester (green).

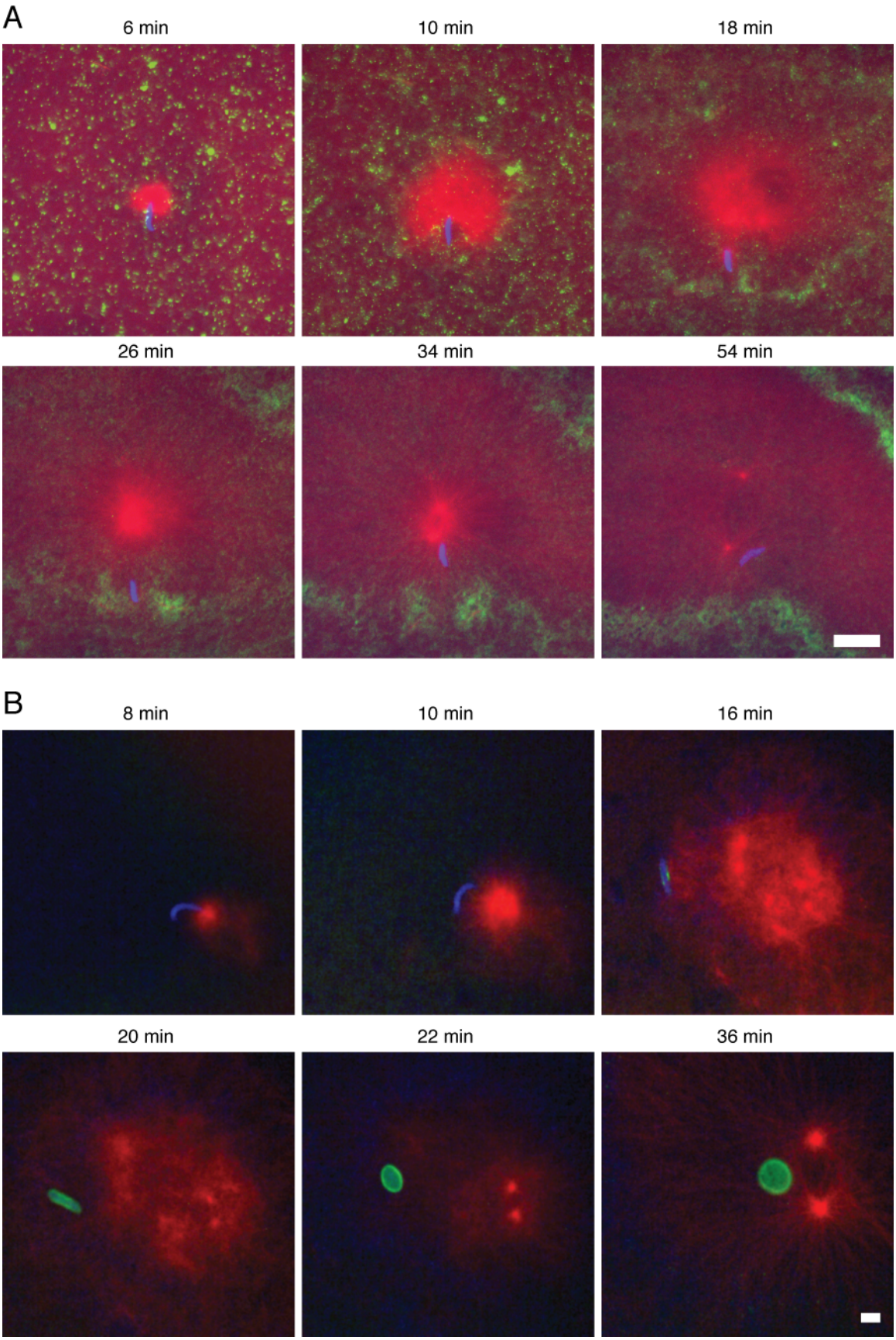
A
6 min
10 min
18 min
26 min
34 min
54 min
B
8 min
10 min
16 min
20 min
22 min
36 min

initially push both sperm and bulk membranes outward, with membranes passively accumulating in a ring around the periphery of the aster. At around 15 to 20 minutes, concomitant with downregulation of Cdk1 activity, the size of the aster stabilizes and becomes less dense. Thereafter, the sperm nucleus reverses the direction of its motion and moves back toward the center of the aster, which is the mechanism by which male and female pronuclei are transported to meet one another in the center of the fertilized egg (Figure 1-2B). We expect this motion to begin only once the sperm has acquired a nuclear envelope to which dynein can anchor for minus-end-directed transport. Consistent with this timing, the first signs of nuclear pore complex assembly are visible around 16 to 20 min, and transport towards the center of the aster begins at around 22 min (Figure 2-1B).

We encountered two major drawbacks with live imaging experiments. First, sperm were easily photodamaged and often failed normal nuclear assembly (Figure 2-1A) and second, we were limited to imaging a small number of nuclei per field of view. We therefore switched to removing samples from nuclear assembly reactions at defined time points, which we could fix and image in large numbers without photodamage (Figure 2-2).

2.2. Dppa2 is essential for nuclear assembly

Previous work in the lab by Eileen Woo had shown that nuclei assembled in Dppa2-depleted (ΔDppa2) extracts had pinched, deformed morphology and swelled irregularly. We decided to examine this phenotype quantitatively, measuring both nuclear size and morphology, the former by calculating average cross-sectional area and the latter by calculating average roundness. Roundness is defined as the ratio between the minor and

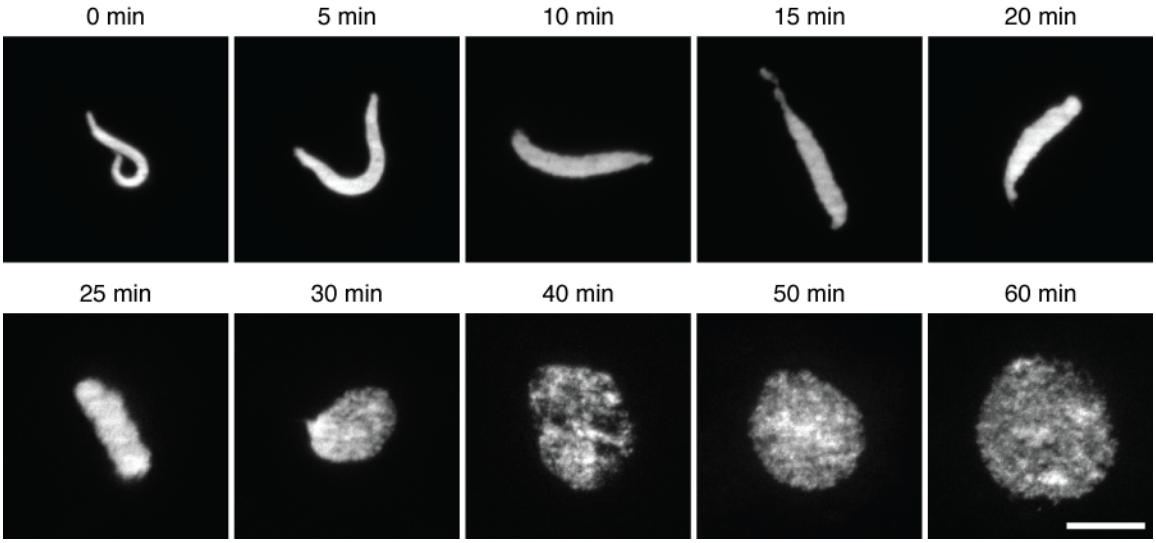

Figure 2-2. Typical nuclear assembly assay

Sperm nuclei were added to CSF-arrested extracts together with calcium to induce release into interphase and initiate pronuclear assembly. At the indicated time points, 1 µl of the assembly reaction was squashed under an 18 × 18 mm coverslip with 3 µl fixative containing formaldehyde and Hoechst 33342. Scale bar, 10 µm.

Figure 2-3. Dppa2 is required for proper nuclear size and shape

(A) Recombinant FLAG-tagged Dppa2 was purified from *E. coli* and analyzed by Coomassie staining.

(B) CSF-arrested metaphase egg extracts were mock-depleted with non-specific IgG or polyclonal anti-Dppa2 antibodies (10 μg rabbit IgG per 100 μl Dynabeads per 100 μl extract), and analyzed by western blotting with anti-Dppa2 (5 μg/ml) and anti-Aurora B (5 μg/ml) antibodies. Recombinant FLAG-tagged Dppa2 was added back to ΔDppa2 extracts, and migrates more slowly than native Dppa2 due to the negatively charged FLAG tag.

(C) 500 sperm nuclei were added per microliter of CSF-arrested egg extract together with 0.3 mM $CaCl_2$. Nuclei were fixed by squashing 1 μl of the nuclear assembly reaction with 3 μl fixative containing formaldehyde and Hoechst under an 18×18 mm coverslip. Three samples were taken at each time point and imaged under 40× objective. Scale bar, 10 μm.

(D) Nuclear area and roundness were calculated using the 'Analyze Particles' command in ImageJ. >30 nuclei were measured per condition per time point. Violin plots indicate kernel density function estimated using R, overlaid with boxplots indicating quartiles, whiskers marking full range and lines connecting median values.

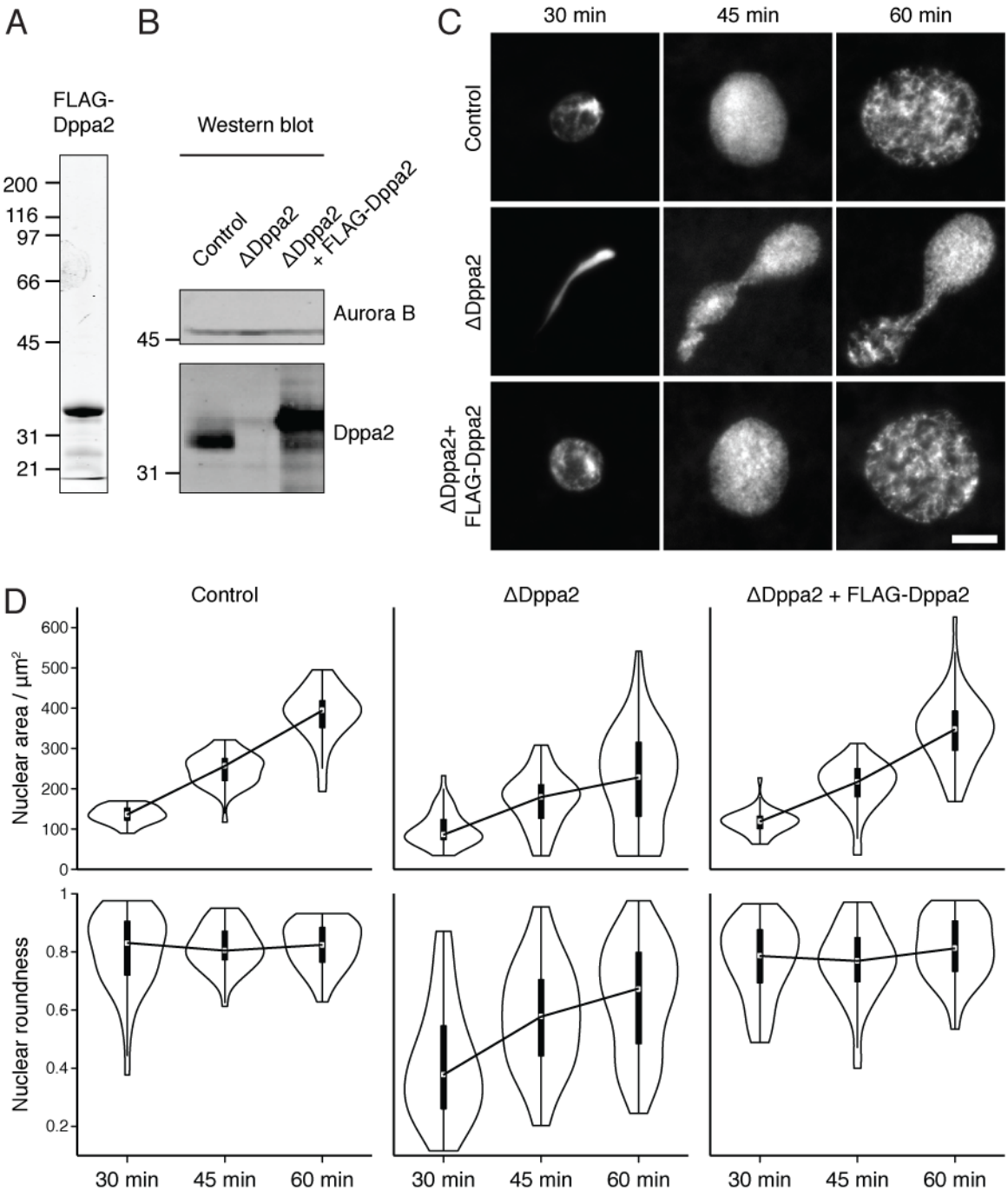
A
FLAG-Dppa2
200
116
97
66
45
31
21
B
Western blot
Control
ΔDppa2
ΔDppa2 + FLAG-Dppa2
Aurora B
Dppa2
45
31
C
30 min
45 min
60 min
Control
ΔDppa2
ΔDppa2+ FLAG-Dppa2
D
Control
ΔDppa2
ΔDppa2 + FLAG-Dppa2
Nuclear area / μm²
600
500
400
300
200
100
0
Nuclear roundness
1
0.8
0.6
0.4
0.2
30 min
45 min
60 min

major axes of a best-fit ellipse. This analysis revealed that nuclei assembled in ΔDppa2 extracts were smaller and departed from normal spherical morphology (Figure 2-3). The defect was rescued by adding back recombinant FLAG-tagged Dppa2 protein, indicating that the phenotype in ΔDppa2 extracts was specific to loss of Dppa2.

Immunofluorescence analysis showed that nuclei assembled in ΔDppa2 extracts had defective nuclear envelopes, with reduced incorporation of lamin B3, the major lamin in *Xenopus* eggs (Lourim et al., 1996), and fewer NPCs (Figure 2-4). These nuclei also failed to complete DNA replication, as judged by incorporation of both radiolabeled and fluorescent nucleotides (Figure 2-5). In particular, DNA replication in ΔDppa2 extracts was uneven, with regions of the nucleus failing to incorporate any nucleotides while other regions appeared normal. The unreplicated regions stained strongly for dimethylation of histone H4 at lysine 20 (H4K20me2), a modification that contributes to recruitment of origin replication complexes and may be a marker of replication stress (Botuyan et al., 2006; Kuo et al., 2012).

2.3. Cell cycle progression and sperm remodeling are not perturbed in ΔDppa2 extracts

We wished to rule out a delay in exiting M phase as the cause of the nuclear defects observed in ΔDppa2 extracts. We found that Cdk1 activity, as judged by histone H1 kinase activity, was downregulated with normal timing in ΔDppa2 extracts (Figure 2-6A), as was mitotic histone H3 serine 10 phosphorylation (H3S10ph; Figure 2-6, B and C). We were also concerned that sperm remodeling, in which sperm chromatin is decompacted and protamines exchanged for histones prior to nuclear assembly (Wright, 1999), might be compromised. However, histone H2B was loaded normally (Figure 2-7,

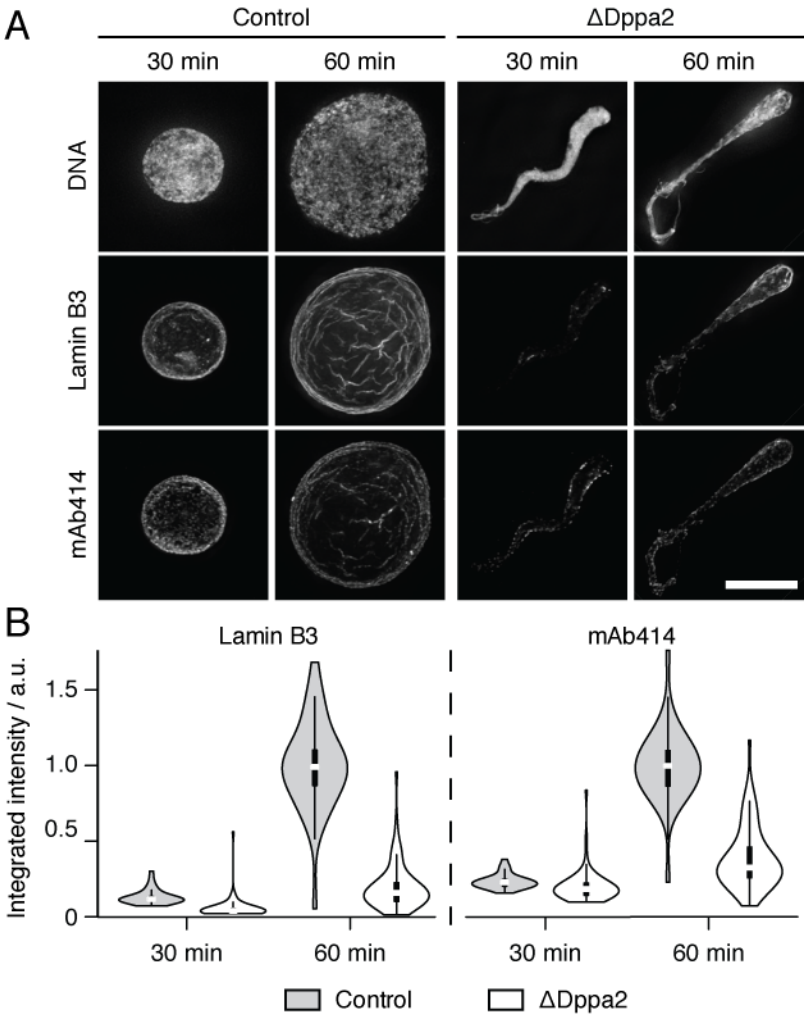

Figure 2-4. Dppa2 depletion leads to nuclear envelope defects

(A) Nuclear assembly reactions were fixed with formaldehyde at the indicated time points, spun onto coverslips, treated with methanol post-fix and stained with anti-lamin B3 antibody (gift of Dale Shumaker; 1/200 dilution) and mAb414 (0.2 μg/ml). Scale bar, 10 μm.

(B) Quantification of integrated fluorescence intensity from (A). Each column indicates mean and standard error from >30 nuclei.

Figure 2-5. DNA replication is impaired in ΔDppa2 extracts

(A) Nuclei were assembled in extracts supplemented with [a-^{33}P]dCTP (1 kBq/μl), At the indicated time points, 15 μl samples were quenched, extracted with phenol/ chloroform and subjected to agarose gel electrophoresis. The dried gel was visualized by fluorography.
Upper band, DNA replication intermediates; lower band, completed replication.

(B) Quantification of signal intensity representing completed replication from (A). Graph shows mean and standard error from 3 independent experiments.

(C) Nuclei assembled in the presence of Cy3-dUTP (10 μM) were spun down and stained with anti-H4K20me2 antibody (gift of Hiroshi Kimura, clone 2E2; 1 μg/ml). Scale bar, 10 μm.

(D) Quantification of integrated dUTP fluorescence intensity from (B). Each column indicates mean and standard error from >30 nuclei.

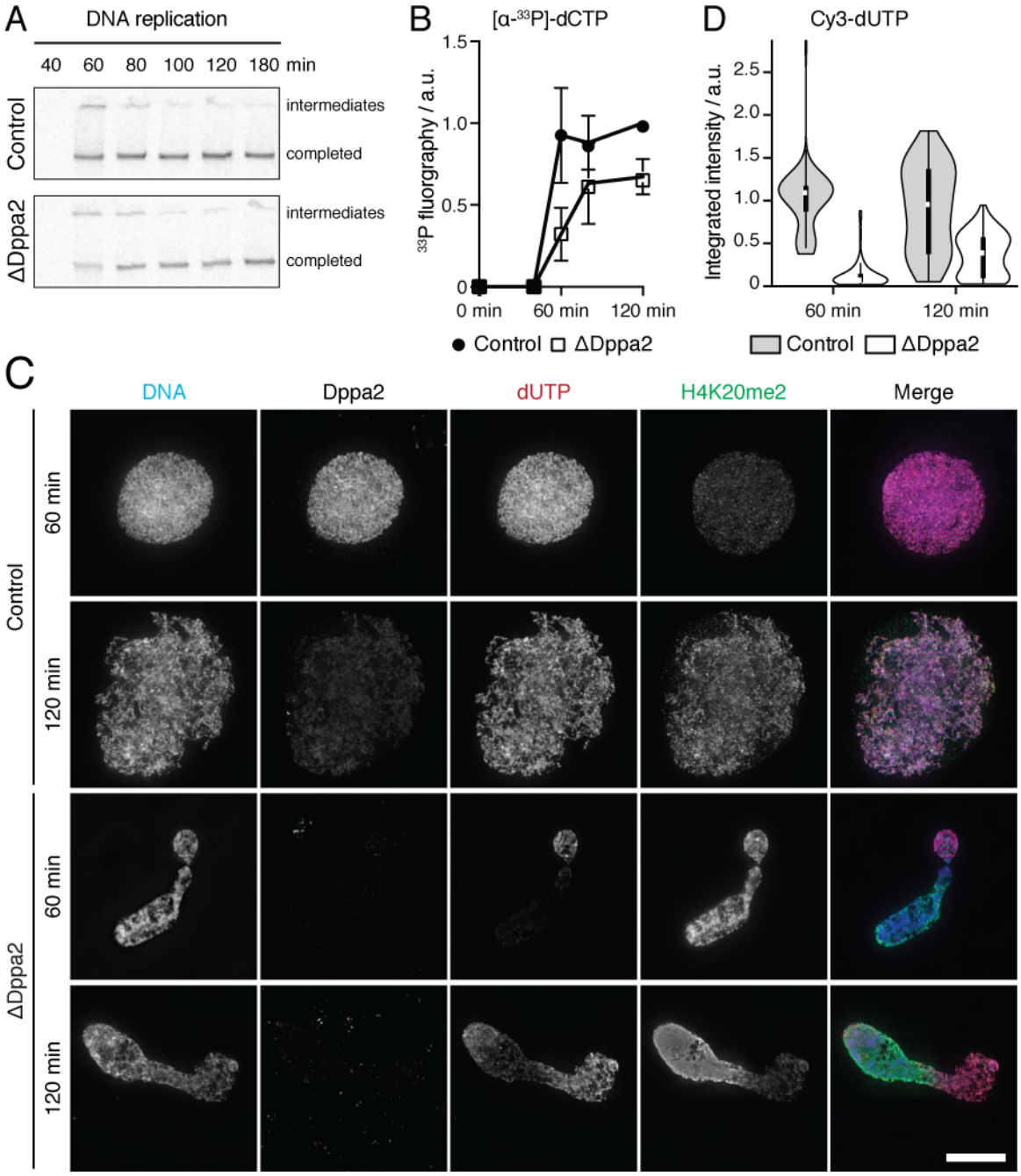
A
DNA replication
40 60 80 100 120 180 min
Control
intermediates
completed
ΔDppa2
intermediates
completed
B
[α-33P]-dCTP
33P fluorgraphy / a.u.
1.5
1.0
0.5
0
0 min
60 min
120 min
Control ΔDppa2
D
Cy3-dUTP
Integrated intensity / a.u.
2.5
2.0
1.5
1.0
0.5
0
60 min
120 min
Control ΔDppa2
C
DNA
Dppa2
dUTP
H4K20me2
Merge
Control
60 min
120 min
ΔDppa2
60 min
120 min

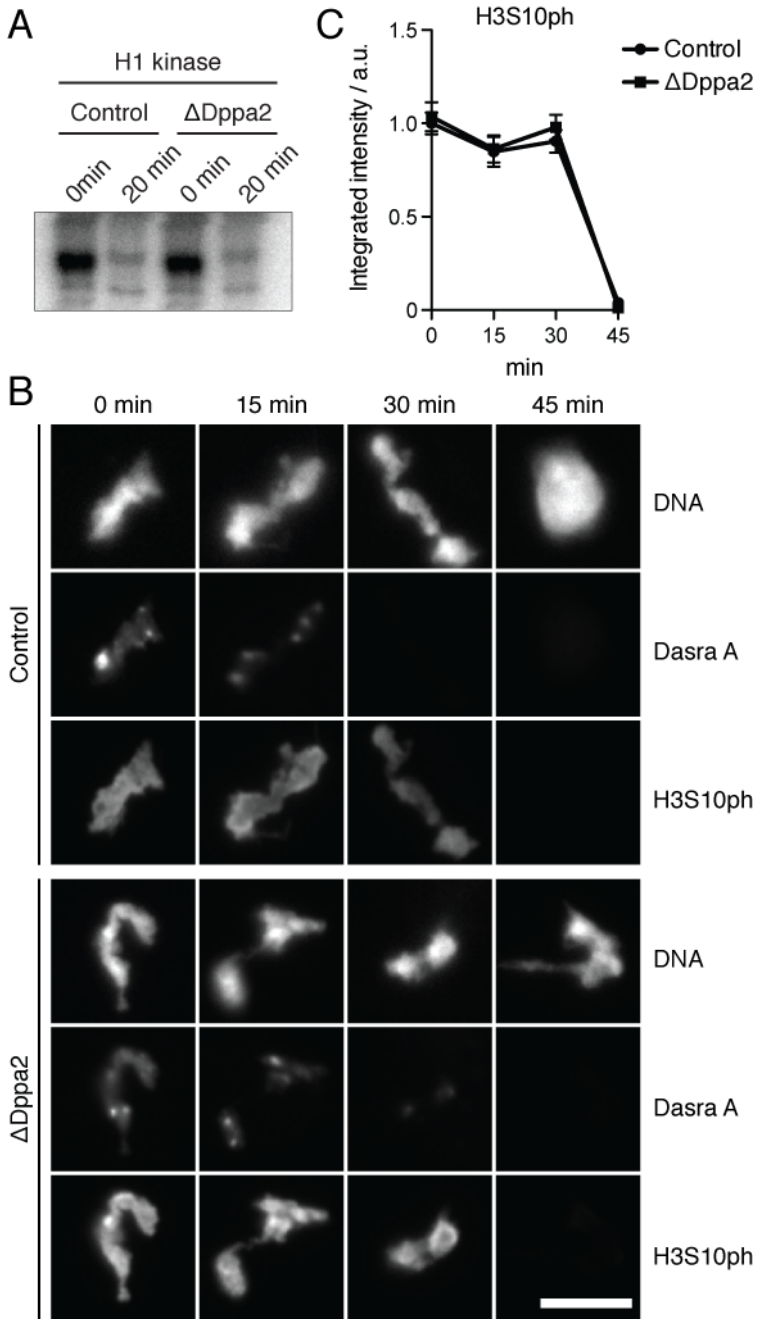

Figure 2-6. Cell cycle progression is not perturbed in ΔDppa2 extracts

(A) Histone H1 kinase activity assay performed at 0 and 20 min after calcium addition.

(B) Sperm were incubated in metaphase extracts for 45 min, then released into interphase by adding calcium. At the indicated time points, nuclei were spun onto coverslips and stained with anti-H3S10ph antibody (gift of Hiroshi Kimura, clone 7G1G7; 1 μg/ml).

(C) Quantification of integrated fluorescence intensity from (B). Each point represents mean and standard error of >12 nuclei.

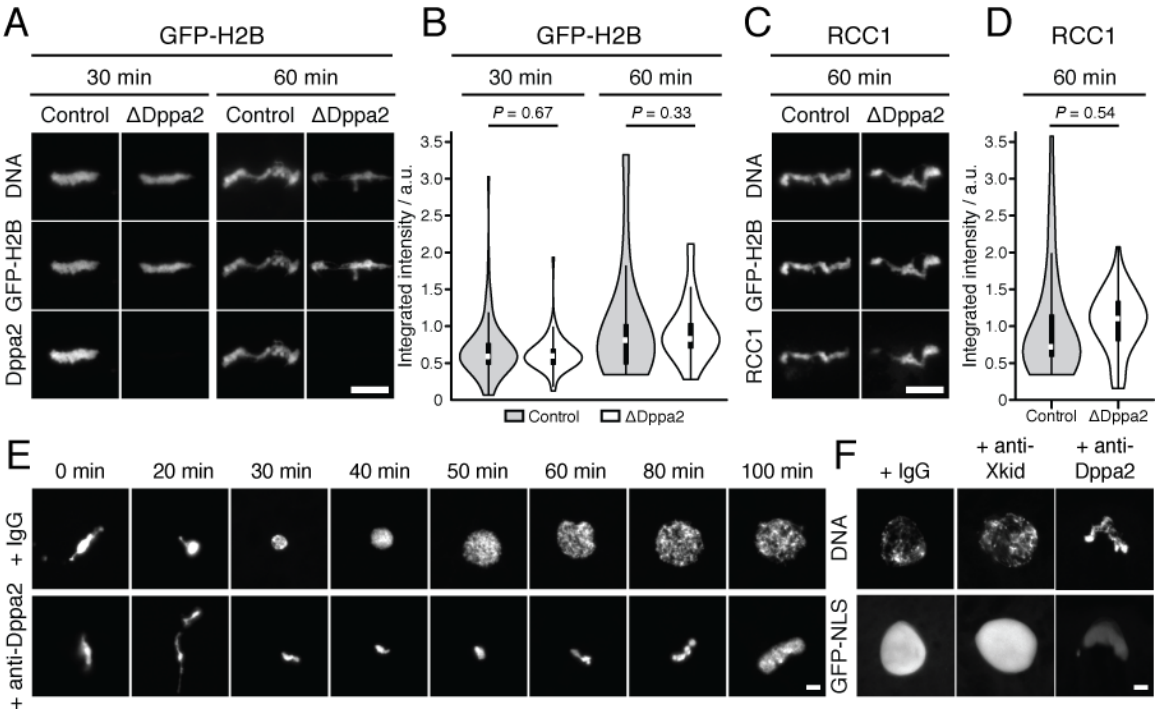

Figure 2-7. Sperm remodeling is not perturbed in ΔDppa2 extracts

(A) Egg extracts were cycled through interphase and back into metaphase in the presence of in-vitro-transcribed mRNA to synthesize GFP-H2B. Sperm were incubated in these extracts, then spun down and stained with anti-GFP antibodies (Roche 11814460001; 2 μg/ml)

(B) Quantification of integrated fluorescence intensity from (B); two-tailed t test.

(C) Immunofluorescence staining of RCC1 loading.

(D) Quantification of (C); two-tailed t test.

(E) Sperm were pre-incubated in metaphase extracts for 45 min, followed by addition of calcium and IgG or anti-Dppa2 antibodies (0.2 mg/ml).

(F) Sperm were pre-incubated in metaphase extracts for 45 min, followed by addition of calcium and IgG, anti-Xkid or anti-Dppa2 antibodies. Nuclear import was monitored with GST-GFP-NLS and visualized after 1 h 40 min.

Scale bars, 10 μm.

A and B). In a complementary experiment, sperm were allowed to remodel normally by incubation in undepleted metaphase extracts, before inhibiting Dppa2 by adding anti-Dppa2 antibody together with calcium to initiate nuclear assembly. In this experiment, inhibiting Dppa2 function still elicited a strong nuclear assembly defect while inhibiting another DNA-binding protein, Xkid, did not (Figure 2-7C).

We have not systematically profiled whether Dppa2 depletion alters the proteomic landscape of proteins bound to chromatin. However, levels of RCC1 and the CPC, two leading candidates that are known to regulate nuclear assembly (Zhang and Clarke, 2000; Hetzer et al., 2000; Ramadan et al., 2007; Kelly et al., 2010), were not affected (Figure 2-8A). We also confirmed that abnormal nuclear shape observed in ΔDppa2 extracts is not a downstream consequence of DNA replication defects, since blocking replication with recombinant non-degradable geminin or aphidicolin did not produce nuclear shape defects in control extracts, while abnormal nuclear shape persisted in ΔDppa2 extracts (Figure 2-8, B and C).

2.4. Dppa2 inhibits microtubule polymerization

When sperm are added to metaphase extracts together with calcium, there is a phase of rapid microtubule nucleation from sperm centrosomes that peaks around 15 minutes, after which microtubules become less dense (Figure 2-1). The same transition can be observed in fixed samples, although from 20 min onwards the aster microtubules become too sparse to be visible under our fixation conditions. We observed that the initial phase of rapid microtubule assembly from sperm centrosomes was enhanced in ΔDppa2 extracts (Figure 2-9, A and B). This suggested that Dppa2 negatively regulated microtubule

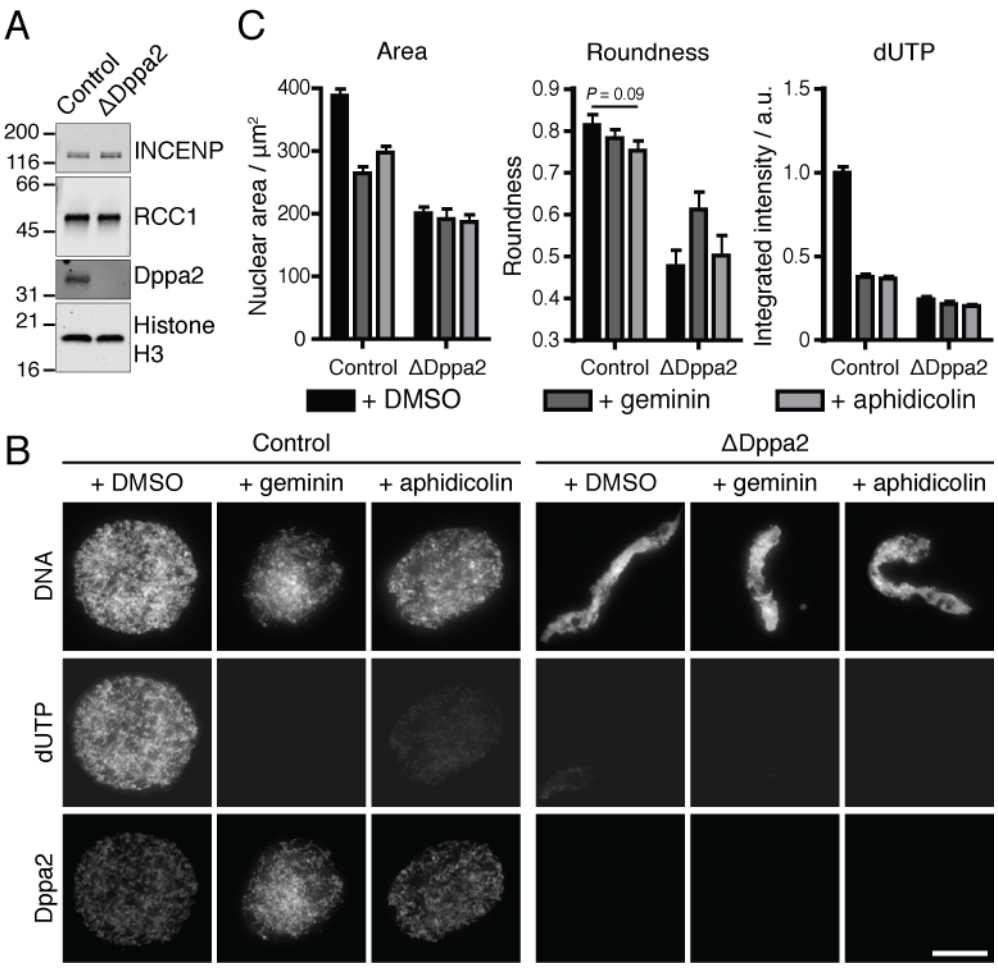

Figure 2-8. Nuclear defects in ΔDppa2 extracts are not caused by abnormal loading of RCC1 or CPC, nor by failed DNA replication

(A) Sperm chromosomes were biotinylated (Funabiki and Murray, 2000) in control and ΔDppa2 extracts and purified for western blotting with anti-RCC1 (gift of Rebecca Heald; 1 μg/ml) and anti-INCENP (5 μg/ml) antibodies.

(B) Nuclei were assembled in extracts supplemented with Cy3-dUTP (10 μM) and non-degradable geminin (8 μM), aphidicolin (40 μM) or DMSO. Scale bar, 10 μm.

(C) Quantification of nuclear size and shape from (B). Each column indicates mean and standard error of >20 nuclei. Inhibition of replication led to minor reduction of nuclear size but no significant reduction in nuclear roundness (comparing control extracts: DMSO vs. geminin, $P = 0.37$; DMSO vs. aphidicolin, $P = 0.09$ by two-tailed unpaired t-test).

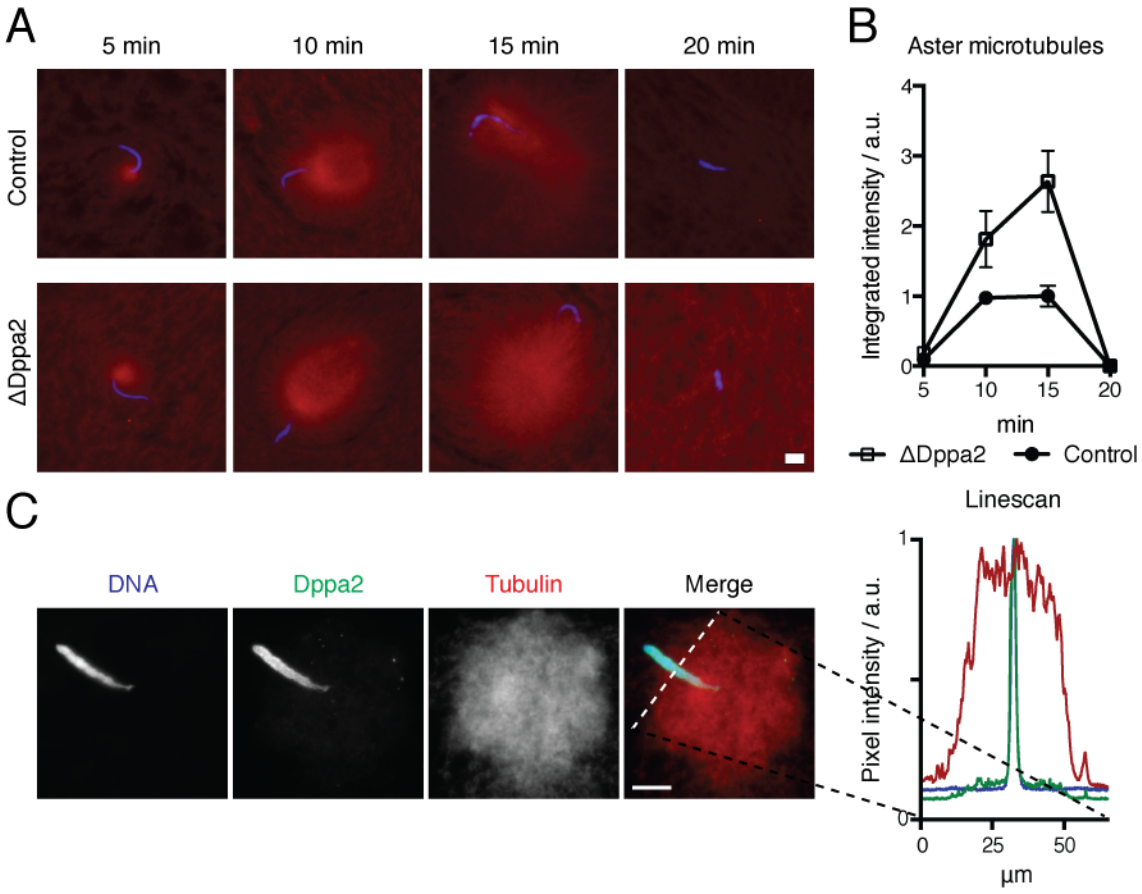

Figure 2-9. Aster microtubule assembly is enhanced in ΔDppa2 extracts

(A) Sperm were added together with calcium to metaphase extracts supplemented with rhodamine-labeled tubulin (0.5 μM), and fixed at the indicated time points.

(B) Quantification of tubulin fluorescence intensity from (A). Each point represents mean and standard error of >30 asters.

(C) Sperm nuclei and asters were spun down for immunofluorescence 12 min after calcium addition.

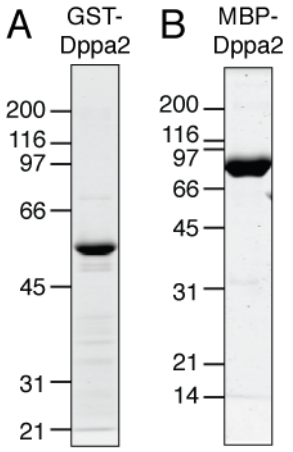

Figure 2-10. Purity of GST- and MBP-tagged Dppa2 proteins

Recombinant GST-Dppa2 (A) and MBP-Dppa2 (B) were purified from *E. coli* and analyzed by Coomassie staining.

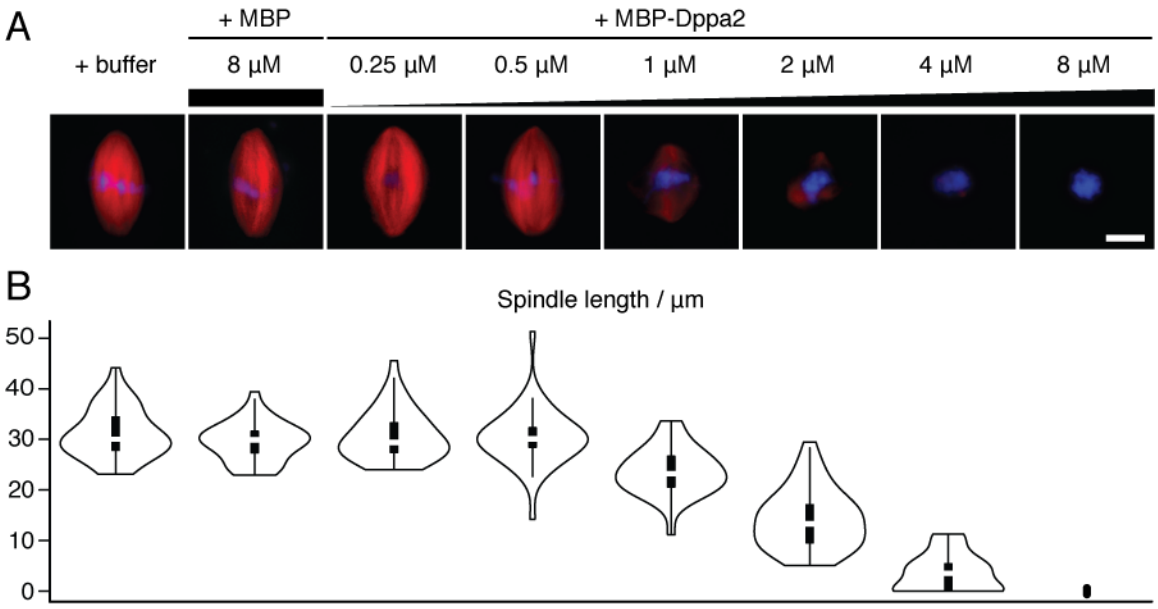

Figure 2-11. Dppa2 inhibits spindle microtubule assembly

(A) Interphase nuclei were assembled by adding sperm and calcium to metaphase extracts containing rhodamine-tubulin and incubating at 20 °C for 1 h 20 min. These nuclei were then cycled back into metaphase by adding an equal volume of fresh CSF-arrested extract, together with recombinant MBP or MBP-tagged Dppa2 proteins to the final concentrations indicated. Spindles were imaged 60 min after adding fresh metaphase extract. Scale bar, 10 μm.

(B) Quantification of spindle length, 30 spindles per condition.

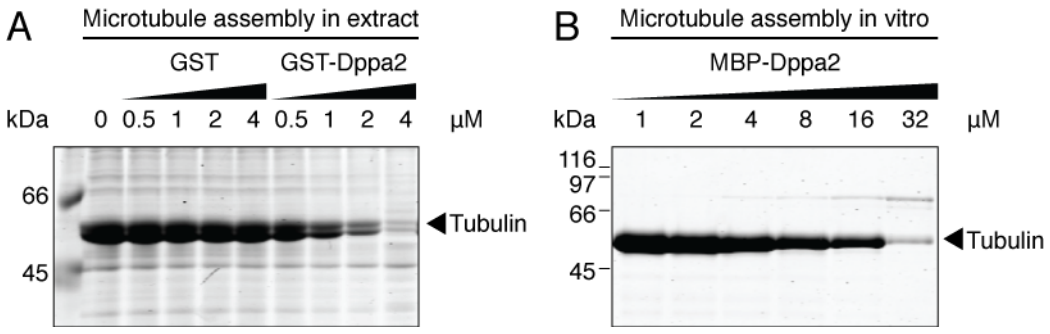

Figure 2-12. Dppa2 inhibits microtubule assembly in the absence of chromatin

(A) Microtubule polymerization was induced by adding DMSO (5%) to metaphase extracts supplemented with recombinant GST or GST-tagged Dppa2 proteins, and incubating at 20 °C for 30 min. Microtubule polymer was pelleted by centrifugation and analyzed by SDS-PAGE.

(B) Purified bovine tubulin was treated with DMSO (5%) and incubated at 37 °C for 30 min in the presence of recombinant MBP-Dppa2. Microtubule polymer was pelleted and analyzed by SDS-PAGE.

assembly during this phase, although Dppa2 remained localized to chromatin and was not detectable on microtubules (Figure 2-9C).

Next we tested the effects of overexpressing Dppa2. For these experiments we purified fusion proteins of Dppa2 with either GST (glutathione S transferase) or MBP (maltose-binding protein), since these tags conferred increased solubility at high concentrations (Figure 2-10). Adding excess recombinant Dppa2 to metaphase extracts destabilized spindle microtubules in a dose-dependent manner (Figure 2-11), confirming that Dppa2 could actively suppress microtubule polymerization.

We expected that like the RanGTP and CPC pathways, Dppa2 would only be able to regulate microtubule assembly when bound to chromatin. This hypothesis can be tested by directly stimulating microtubule polymerization in egg extracts with DMSO. To our surprise, recombinant Dppa2 was still able to inhibit DMSO-induced microtubule polymerization in the absence of chromatin (Figure 2-12A). Recombinant Dppa2 protein also inhibited DMSO-induced polymerization of purified tubulin (Figure 2-12B), indicating that it has intrinsic activity to suppress microtubule assembly. However, we do not exclude the possibility that Dppa2 activity is modulated in vivo by cofactors and/or posttranslational modifications.

Chapter 3. Nuclear assembly requires spatiotemporally-balanced microtubule dynamics

3.1. Dppa2 functionally opposes the CPC

The previous chapter showed that Dppa2 promotes nuclear formation while suppressing microtubule assembly. This contrasts with the CPC, which inhibits nuclear formation but promotes microtubule polymerization (Ramadan et al., 2007, Sampath et al., 2004). We found that the CPC indeed functionally opposes Dppa2 in both these activities. The increase in microtubule assembly observed in ΔDppa2 extracts was reduced to control levels when the CPC was co-depleted with anti-INCENP antibodies (Figure 3-1, A and B). Co-depletion of the CPC also rescued the nuclear roundness defect of ΔDppa2 extracts, although it did not rescue nuclear size (Figure 3-1, C and D).

We considered that Dppa2 might be a novel suppressor of the well-established CPC pathway, or possibly acted somewhere downstream of the CPC, thereby explaining their mutual antagonism. However, this was not the case. While excess Dppa2 abolished spindle microtubules, it did not do so by repressing the CPC since neither CPC substrate phosphorylation nor localization were affected (Figure 2-6B and Figure 3-2, A – C). Consistent with this observation, we had previously seen that histone H3 serine 10 phosphorylation, which is a major CPC target, was unaffected in ΔDppa2 extracts (Figure 2-6, B and C). Moreover, Dppa2 continued to suppress microtubule polymerization even in CPC-depleted extracts (Figure 3-2D). This confirms that while inhibition of microtubule polymerization and stimulation of nuclear assembly by Dppa2 appears to be counterbalanced by equal and opposite CPC activities, Dppa2 acts entirely independently of the CPC.

Figure 3-1. CPC co-depletion rescues ΔDppa2 phenotypes of microtubule assembly and nuclear shape

(A) Dilution series of mock-depleted extracts is shown alongside ΔCPC and ΔDppa2 depletion to indicate >94% depletion efficiency.

(B) Sperm were added together with calcium to extracts supplemented with rhodamine-tubulin. Asters were visualized after 15 min.

(C) Quantification of microtubule fluorescence intensity from (A). Each point represents mean and standard error of >30 asters.

(D) Nuclear assembly in ΔCPC and ΔDppa2 extracts.

(E) Quantification of nuclear cross-sectional area and roundness from (C). Each point represents mean and standard error of >30 nuclei.

Scale bars, 10 μm.

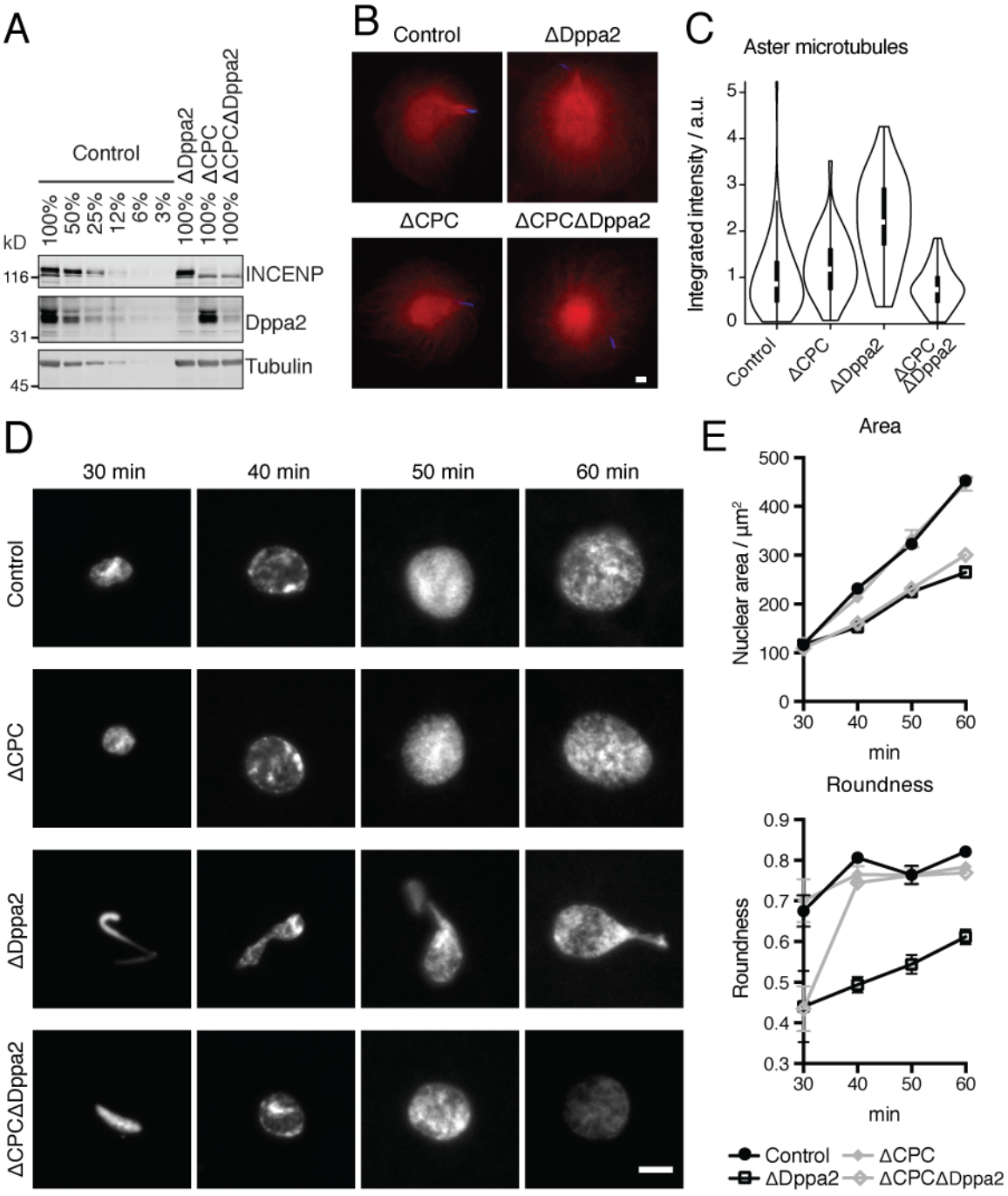
A
Control
100%
50%
25%
12%
6%
3%
ΔDppa2
100%
ΔCPC
100%
ΔCPCΔDppa2
100%
kD
116
INCENP
31
Dppa2
45
Tubulin
B
Control
ΔDppa2
ΔCPC
ΔCPCΔDppa2
C
Aster microtubules
Integrated intensity / a.u.
0
1
2
3
4
5
Control
ΔCPC
ΔDppa2
ΔCPC ΔDppa2
D
30 min
40 min
50 min
60 min
Control
ΔCPC
ΔDppa2
ΔCPCΔDppa2
E
Area
Nuclear area / μm²
0
100
200
300
400
500
30
40
50
60
min
Roundness
Roundness
0.3
0.4
0.5
0.6
0.7
0.8
0.9
30
40
50
60
min
Control
ΔCPC
ΔDppa2
ΔCPCΔDppa2

Figure 3-2. Dppa2 does not act through the CPC

(A) Metaphase spindles were assembled in extracts supplemented with buffer or 4 μM recombinant Dppa2 protein, then spun down for immunofluorescence to detect CPC localization (anti-Dasra antibody; 6 μg/ml) or CPC substrate phosphorylation (anti-H3S10ph antibody; gift of Hiroshi Kimura, clone 7G1G7; 1 μg/ml). A parallel set of samples was treated with nocodazole to collapse chromatin into identical structures for quantitative comparison.

(B) Quantification of nocodazole-treated samples from (A). Columns indicate mean and standard error of >30 chromatin structures.

(C) Metaphase spindles assembled as in (A), stained with anti-MCAK antibody (gift of Ryoma Ohi; 0.2 μg/ml) to detect the CPC-dependent centromeric localization of MCAK (Lan et al., 2004).

(D) Control and ΔCPC extracts were treated with recombinant MBP-tagged Dppa2 and DMSO (5%) to induce microtubule assembly. Microtubule polymer was pelleted and analyzed by SDS-PAGE.

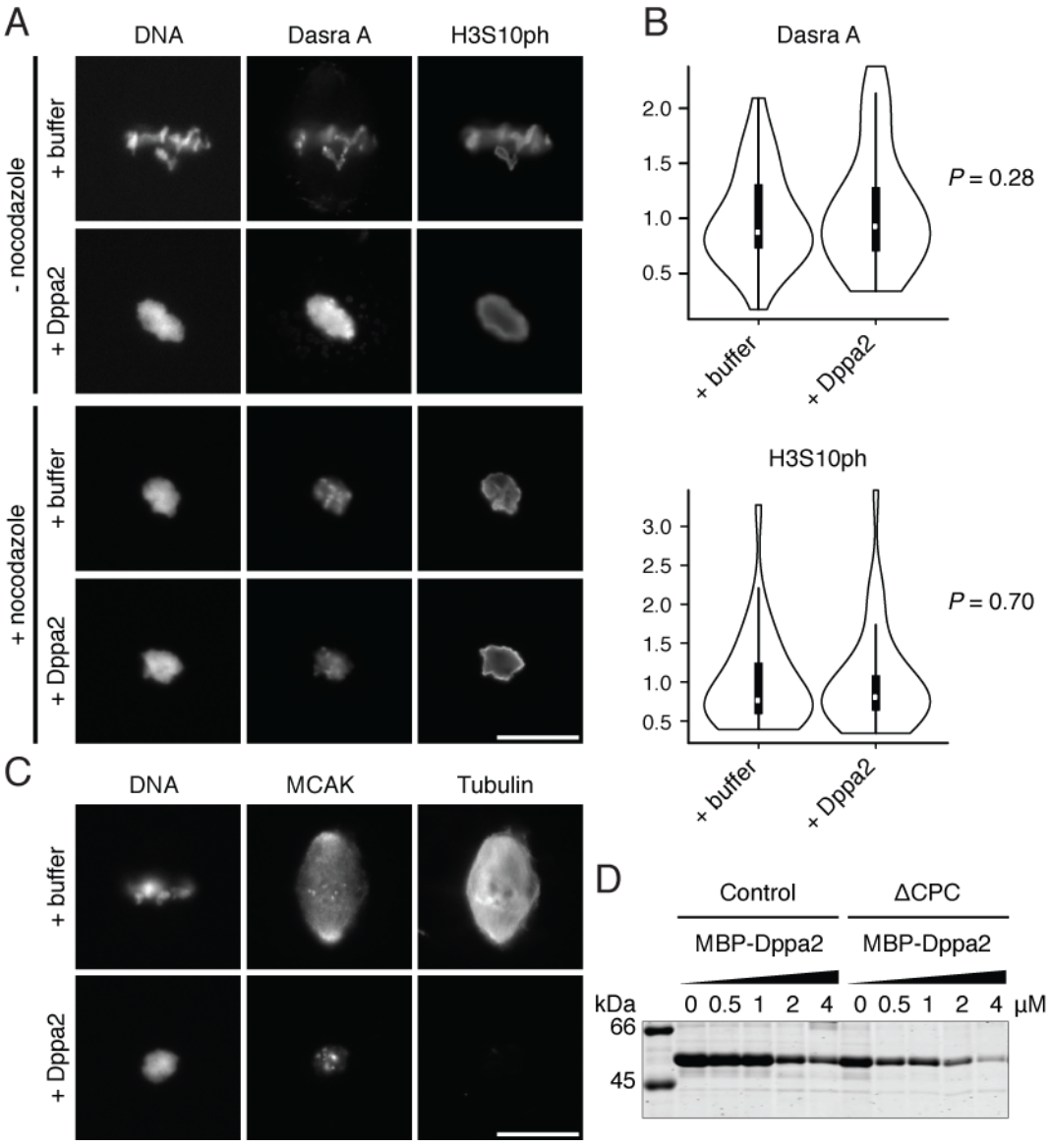
A
DNA
Dasra A
H3S10ph
- nocodazole
+ buffer
+ Dppa2
+ nocodazole
+ buffer
+ Dppa2
B
Dasra A
2.0
1.5
1.0
0.5
P = 0.28
+ buffer
+ Dppa2
H3S10ph
3.0
2.5
2.0
1.5
1.0
0.5
P = 0.70
+ buffer
+ Dppa2
C
DNA
MCAK
Tubulin
+ buffer
+ Dppa2
D
Control
ΔCPC
MBP-Dppa2
MBP-Dppa2
kDa
0 0.5 1 2 4 0 0.5 1 2 4 μM
66
45

3.2. Nuclear defects in ΔDppa2 extracts are caused by excess microtubule assembly

We hypothesized that excess microtubules in ΔDppa2 extracts (Figure 2-9) could directly perturb nuclear assembly by obstructing nuclear envelope closure (Chaudhary and Courvalin, 1993; Lu et al., 2011; Beaudouin et al., 2002; Salina et al., 2002). This model predicts that ectopically destabilizing microtubules would reverse the nuclear assembly defect. Indeed treatment with 16 μM nocodazole restored normal nuclear shape in ΔDppa2 extracts. Conversely, stabilizing excess microtubules with 10 μM taxol mimicked Dppa2 depletion and led to comparable defects in nuclear size and shape (Figure 3-3).

Although nocodazole treatment rescued nuclear shape in ΔDppa2 extracts, it failed to rescue nuclear size in ΔDppa2 extracts and furthermore reduced nuclear size in control extracts (Figure 3-3). This was not a non-specific effect of nocodazole treatment, since depolymerizing microtubules with the drug colcemid or the recombinant protein Op18 also resulted in smaller nuclei (Figure 3-4A). The reduction in nuclear size caused by depolymerizing microtubules was not caused by activation of the spindle assembly checkpoint (SAC) and delay in exiting M phase, because the SAC is suppressed in *Xenopus* egg extracts unless much higher concentrations of DNA are present than those used in our nuclear assembly assays (Minshull et al., 1994). SAC-mediated arrest would maintain high Cdk1 activity as well as Cdk1-dependent phosphorylation of histone H3 threonine 3 (H3T3ph) by the kinase Haspin (Ghenoiu et al., 2013). However, depolymerizing microtubules did not affect normal dephosphorylation of H3T3, and both

nocodazole and taxol treatment resulted in decreased nuclear size even in ΔCPC extracts where the SAC is inactive (Figure 3-4C).

Our results suggested that completely abolishing microtubule assembly was detrimental to nuclear expansion and led to reduced nuclear size. To address this possibility we titrated down the amount of nocodazole, so as to allow some microtubules to survive. This was achieved at the low dose of 0.4 μM, which reduced microtoubule assembly sufficiently to rescue nuclear shape in ΔDppa2 extracts, while not completely eliminating microtubules. Consistent with our prediction, this concentration of nocodazole no longer had the same negative impact on nuclear size (Figure 3-5, A and B). This dose of nocodazole also successfully rescued DNA replication in ΔDppa2 extracts (Figure 3-5C), and so we concluded that functional nuclear assembly depends on a strict balance of microtubule dynamics. Excess microtubules can lead to abnormal nuclear shape and loss of roundness, but the presence of some microtubules is still required to promote nuclear expansion.

3.3. Dppa2 activity is required in a narrow time window during nuclear assembly

In previous figures nocodazole was present in extracts from the beginning of each experiment. However, the major phase of microtubule polymerization associated with nuclear assembly occurs between 10 and 20 min after calcium addition (Figure 2-9A). We hypothesized that the function of Dppa2 could be to fine-tune microtubule assembly during this time window, when the nuclear envelope is not fully formed (Figure 2-1) and hence more vulnerable to microtubule-dependent shear stress. In agreement with this hypothesis, we found that the requirement for Dppa2 in ensuring normal nuclear shape

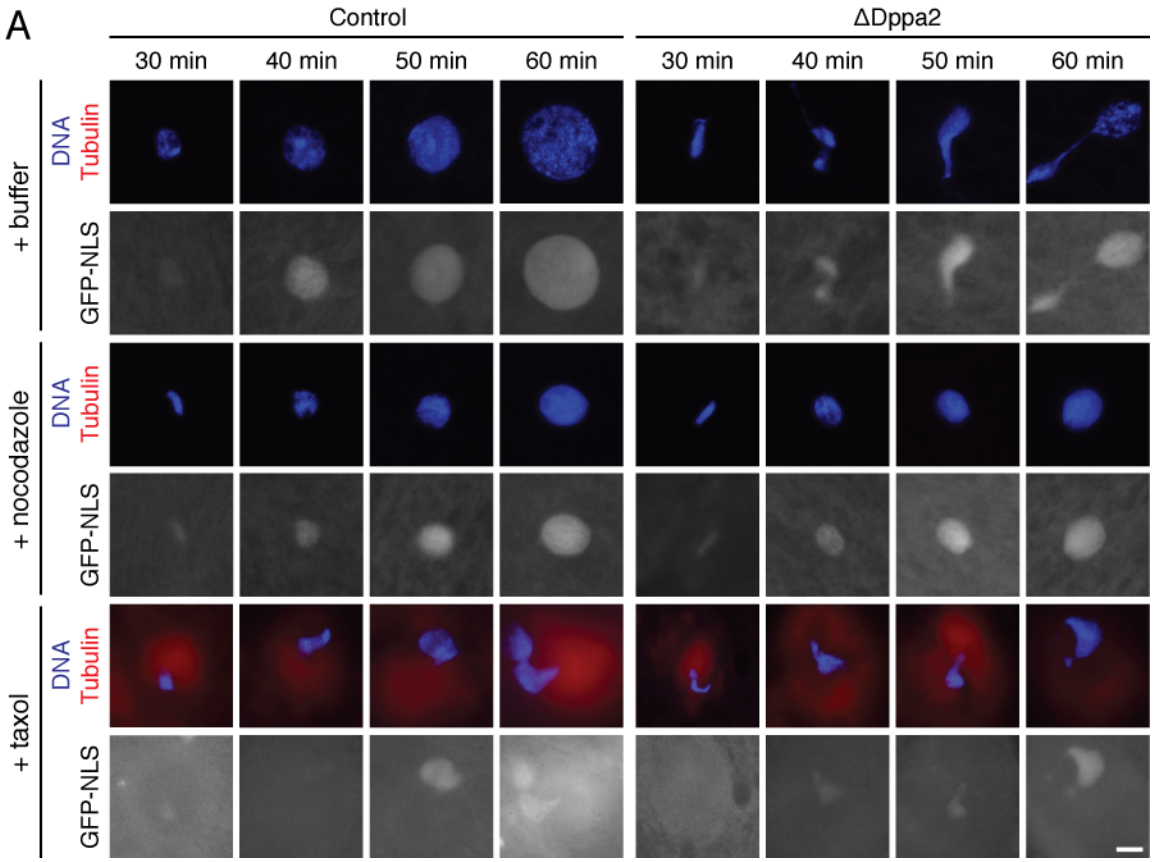

Figure 3-3. Nuclear shape defects in ΔDppa2 extracts are rescued by nocodazole and mimicked by taxol

(A) Nuclei were assembled in extracts treated with nocodazole (16 μM) or taxol (10 μM). Extracts were supplemented with rhodamine-labeled tubulin (red) and GST-GFP-NLS to monitor nuclear import. Scale bar, 10 μm.

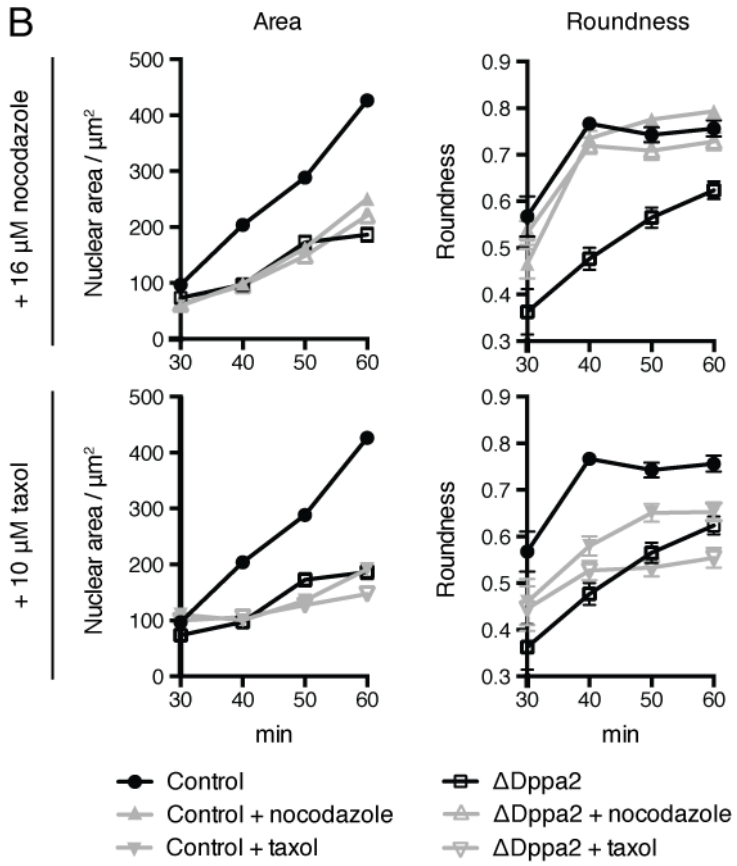

(B) Quantification of nuclear area and roundness from (A). Data from nocodazole- and taxol-treated samples are shown on separate axes, control data are replicated on both. Each point represents mean and standard error of >30 nuclei.

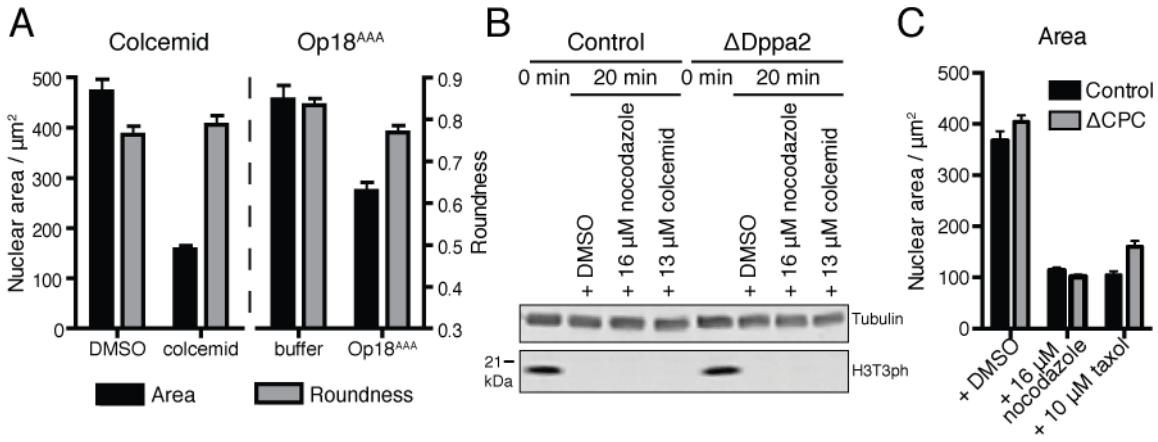

Figure 3-4. Destabilizing microtubules inhibits nuclear expansion without activating the spindle assembly checkpoint

(A) Nuclei were assembled in extracts treated with colcemid (13 µM) or recombinant GST-tagged Op18^{AAA} (4 µM). Nuclear area and roundness were measured after 60 min. Each column represents mean and standard error of >20 nuclei.

(B) Sperm were added to extracts together with calcium and the drugs indicated. Timely exit from M phase was assessed by western blotting with anti-H3T3ph (Millipore 07-424; 1/10,000) and anti-α-tubulin (Sigma T9026; 1/20,000) antisera.

(C) Nuclear assembly in control and ΔCPC extracts treated with nocodazole or taxol. Each column represents mean and standard error of >30 nuclei.

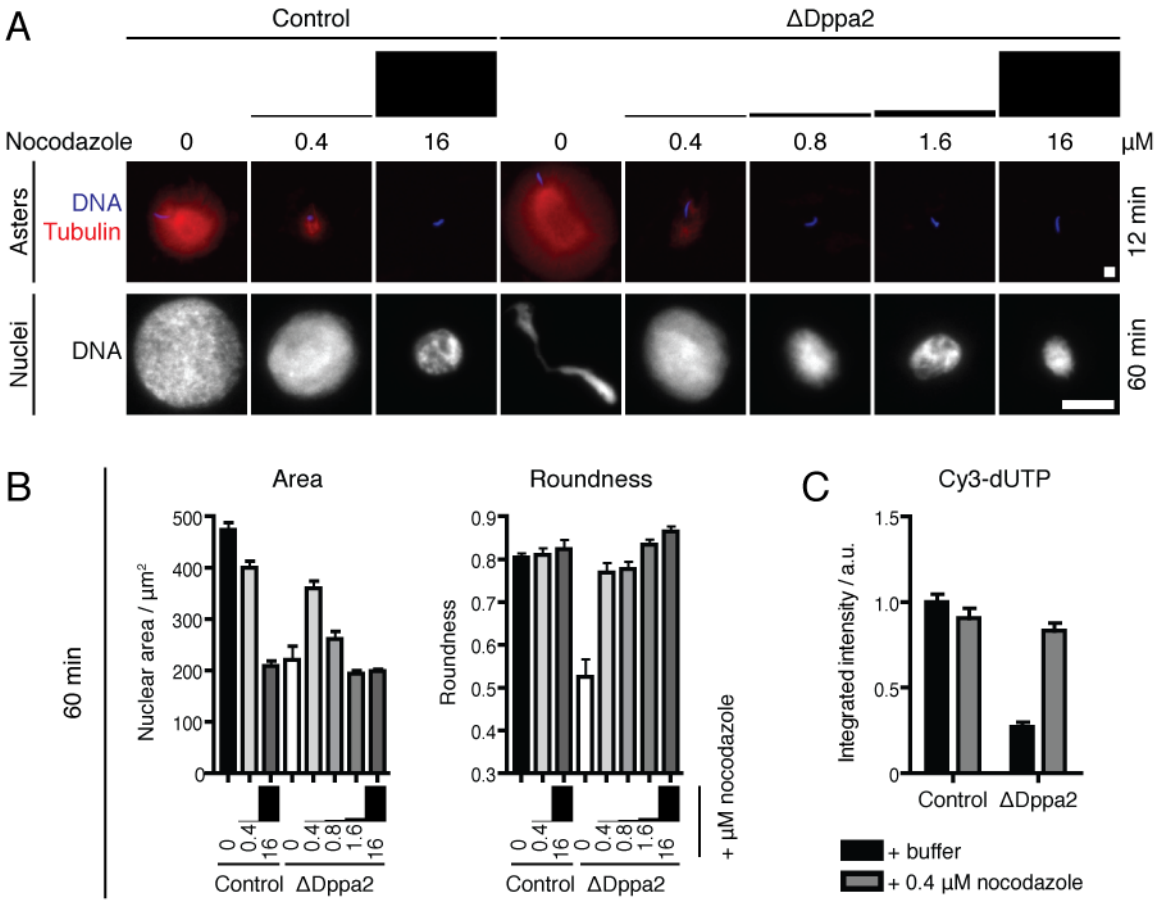

Figure 3-5. Nuclear assembly requires finely balanced microtubule dynamics

(A) Nuclei were assembled in extracts supplemented with the indicated concentrations of nocodazole. Asters were visualized at 12 min after calcium addition, nuclei at 60 min. Scale bars, 10 μm.

(B) Quantification of nuclear area and roundness from (A). Each column represents mean and standard error of >30 nuclei.

(C) Nuclei assembled in extracts supplemented with Cy3-dUTP were spun down after 60 min. Each column represents mean and standard error of >30 nuclei.

could no longer be bypassed by nocodazole if nocodazole treatment was delayed for 30 min (Figure 3-6A). Similarly, ectopic microtubules induced with taxol no longer perturbed nuclear formation after 30 min (Figure 3-6B). We propose therefore that nuclear assembly is sensitive to microtubule dynamics during a restricted time window, after which it is irreversibly committed to normal or abnormal morphology and expansion regardless of microtubule status.

This window of sensitivity coincides with the burst of dense aster microtubule growth at the transition from M phase to interphase. In egg extracts prematurely released into interphase before sperm are added, this burst does not take place since Cdk1 activity is already low by the time sperm centrosomes are exposed to extract. We discovered that in this regime, nuclei assembled in ΔDppa2 extracts are indistinguishable from control extracts. Indeed, nuclear assembly appeared to be insensitive also to nocodazole or taxol treatment (Figure 3-7). We propose therefore that the burst of aster growth that normally accompanies fertilization and pronuclear formation sensitizes the nuclear assembly process to perturbations in microtubule dynamics, necessitating Dppa2 as an extra safeguard to buffer microtubule dynamics around nascent nuclei. In interphase extracts, microtubules are comparatively sparse and stable (Figure 2-1, late time points) and do not subject nuclei to the same push and pull forces as highly dynamic M phase microtubules, which could explain why altering microtubule dynamics have less impact on nuclear assembly in this regime.

However, we also noted that nuclei assembled in interphase extracts without this burst of microtubule growth are misshaped even in control extracts treated with nocodazole (Figure 3-7), suggesting that the rapid phase of microtubule polymerization

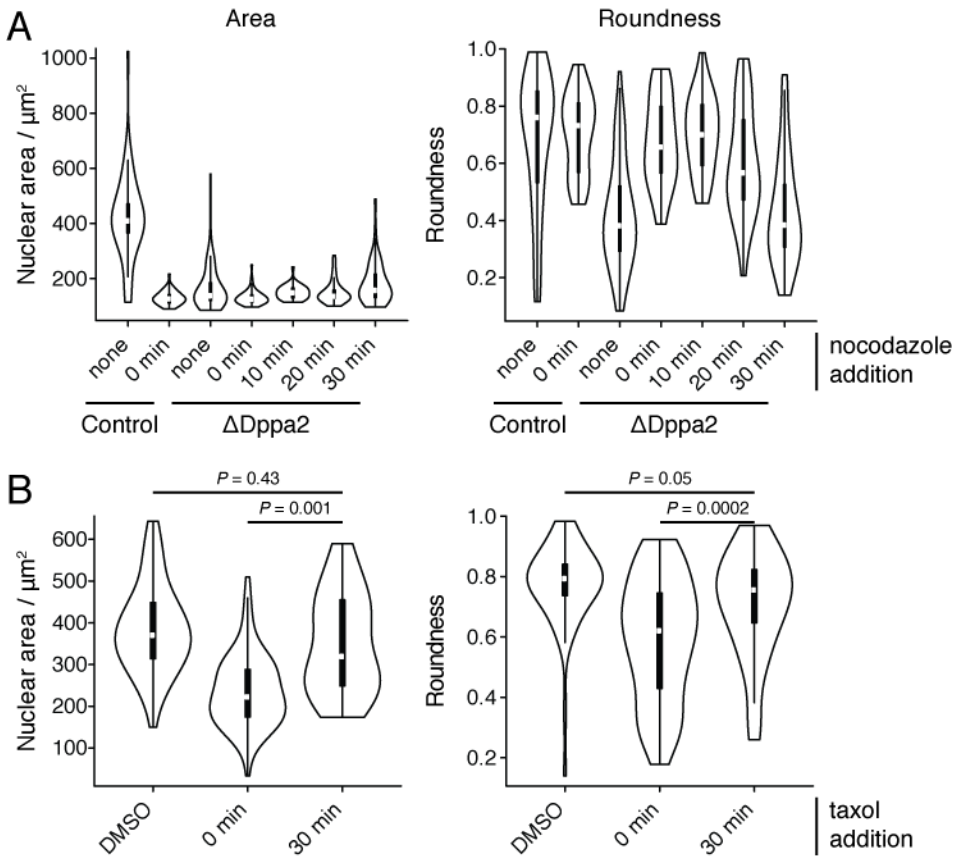

Figure 3-6. Nuclear assembly is sensitive to altered microtubule dynamics during a narrow time window

(A) Sperm and calcium were added to metaphase extracts, followed by 16 μM nocodazole at the indicated time points. Nuclei were imaged 60 min after calcium addition, n > 30 for each condition.

(B) Sperm and calcium were added to metaphase extracts, followed by 10 μM taxol at the indicated time points. Nuclei were imaged 60 min after calcium addition, n > 30 for each condition.

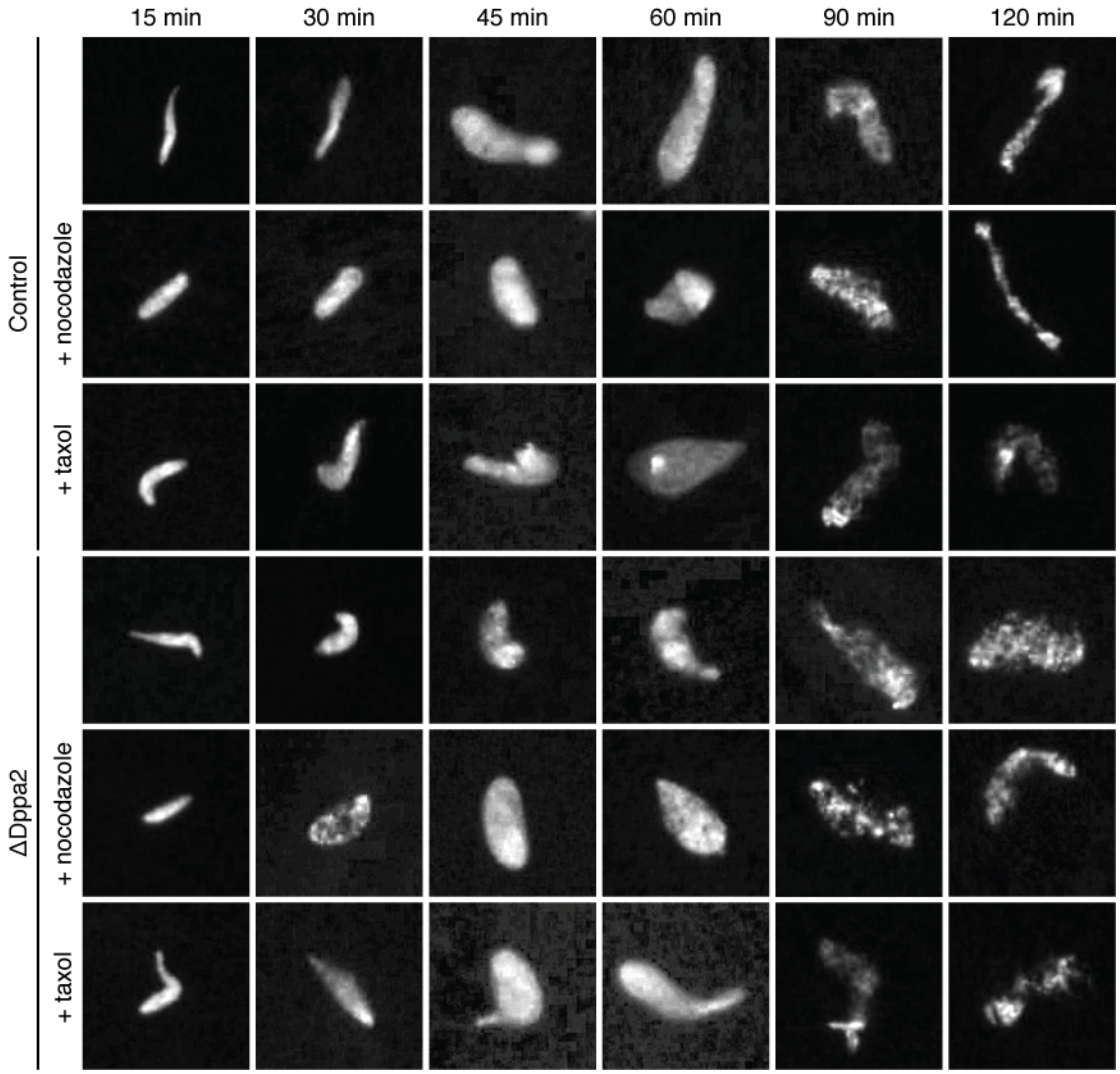

Figure 3-7. Nuclear assembly in interphase extracts

Metaphase extracts were released into interphase by addition of calcium and 1 h incubation at 20 °C. Sperm were then added together with nocodazole or taxol.

positively promotes nuclear formation. We hypothesize that if microtubules are not present to deliver membranes during the initial stages of nuclear assembly, the nucleus may fail to round up properly and then becomes irreversibly committed to abnormal morphology.

3.4. SUMOylation of Dppa2 is dispensable for suppressing microtubules

Dppa2 contains a potential DNA-binding domain in its SAP motif (Figure 1-4), but we found that a point mutation in the SAP domain, previously reported to abolish DNA binding (Woo, 2010), did not affect loading onto DNA beads (Figure 3-8, A and B). We also found that mutating lysine 230 in the C terminus of Dppa2 did not affect DNA-binding, but largely abolished its DNA-dependent SUMOylation, confirming earlier demonstrations that lysine 230 is the SUMO acceptor site (Woo, 2010). However, SUMOylation-deficient Dppa2 was able to inhibit microtubule assembly (Figure 3-8, C and D). Similarly, depletion of the SUMO E3 ligase PIASy (Woo, 2010) abolished SUMOylation of Dppa2 (Figure 3-8E), but did not affect its suppression of spindle assembly (Figure 3-8F).

3.5. The C terminus of Dppa2 is required to inhibit microtubule assembly

Next we turned to larger truncation mutants. The boundaries of the SAP and DCR domains of Dppa2 were consistent with a predicted disorder plot, and we designed deletion mutants around these motifs (Figure 3-9). Deletion of the SAP domain ($Dppa2^{\Delta SAP}$) successfully abolished DNA-binding, without affecting the capacity of Dppa2 for inhibiting microtubule assembly. On the other hand, Dppa2 lacking the last 86 amino acids of its C terminus ($Dppa2^{\Delta C}$) could bind DNA but no longer suppress

Figure 3-8. SUMOylation of Dppa2 is not required to inhibit microtubule assembly

(A) GST-FLAG-tagged Dppa2 proteins were purified from *E. coli* and analyzed by Coomassie staining.

(B) DNA-coated beads (Postow et al., 2008) were incubated in egg extracts supplemented with 0.4 μM GST-FLAG-tagged Dppa2 proteins for 45 min at 20 °C, then detected by western blotting with anti-FLAG antibody (Sigma F1804; 1 μg/ml). Arrowheads indicate unmodified Dppa2 in the cytosol and a SUMOylated species migrating at higher molecular weight.

(C) Spindles assembled in extracts supplemented with recombinant GST-FLAG-Dppa2 (4 μM).

(D) DMSO-induced spindle assembly in extracts supplemented with GST-FLAG-Dppa2. Data in this figure and Figure 2-12A came from the same experiment.

(E) Metaphase extracts were immunodepleted using antibodies against the N terminus of PIASy (gift of Yoshiaki Azuma; 5 μg antibody per 100 μl beads per 100 μl extract), then supplemented with MBP-FLAG-tagged wild-type Dppa2. DNA beads were incubated in these extracts at 20 °C for 1 h, then analyzed by western blotting. The SUMOylated forms of both recombinant Dppa2 (detected by FLAG tag) and endogenous Dppa2 were abolished by PIASy depletion.

(F) Spindles were assembled in control and ΔPIASy extracts supplemented with wild-type or SUMOylation-deficient MBP-FLAG-Dppa2.

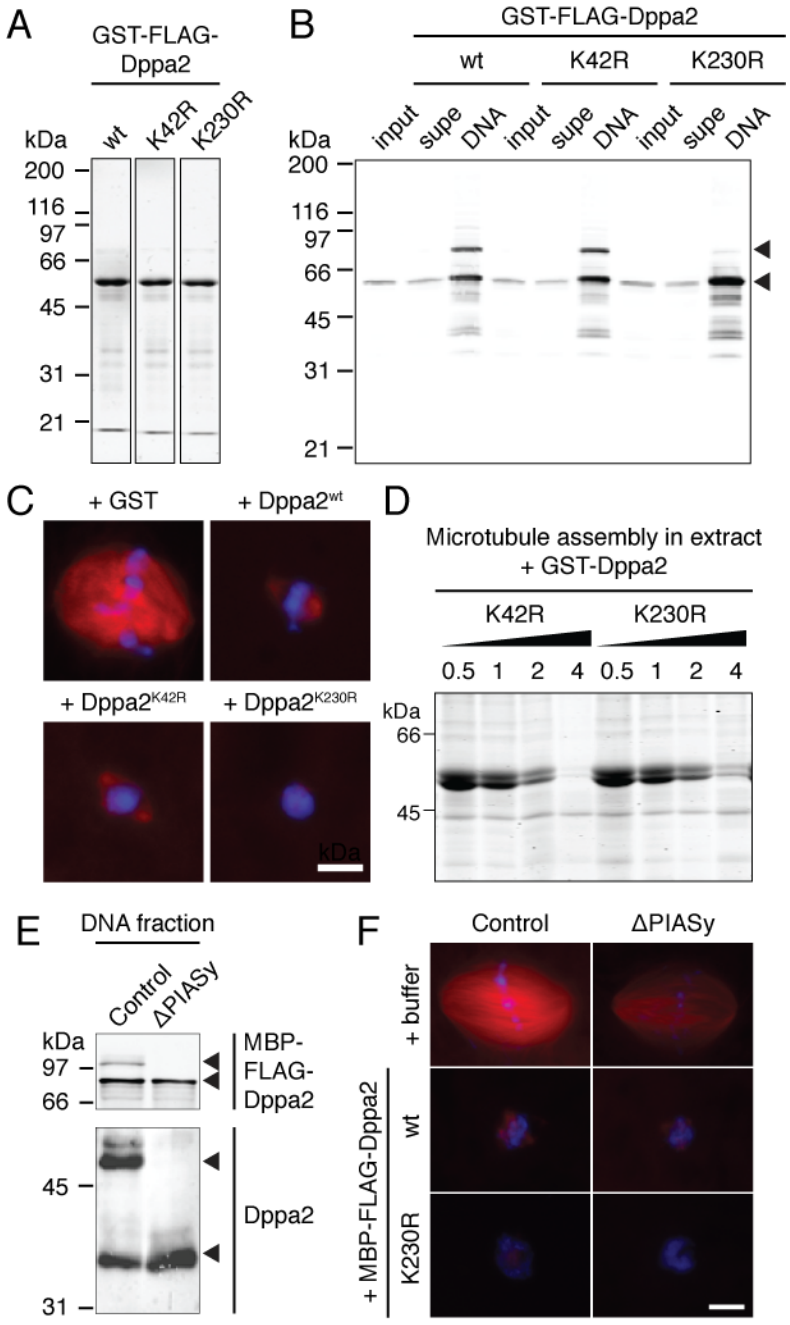
A
GST-FLAG-Dppa2
wt
K42R
K230R
kDa
200
116
97
66
45
31
21
B
GST-FLAG-Dppa2
wt
K42R
K230R
input
supe
DNA
C
+ GST
+ Dppa2wt
+ Dppa2K42R
+ Dppa2K230R
kDa
D
Microtubule assembly in extract
+ GST-Dppa2
K42R
K230R
0.5 1 2 4 0.5 1 2 4
E
DNA fraction
Control
ΔPIASy
MBP-FLAG-Dppa2
Dppa2
F
Control
ΔPIASy
+ buffer
+ MBP-FLAG-Dppa2
wt
K230R

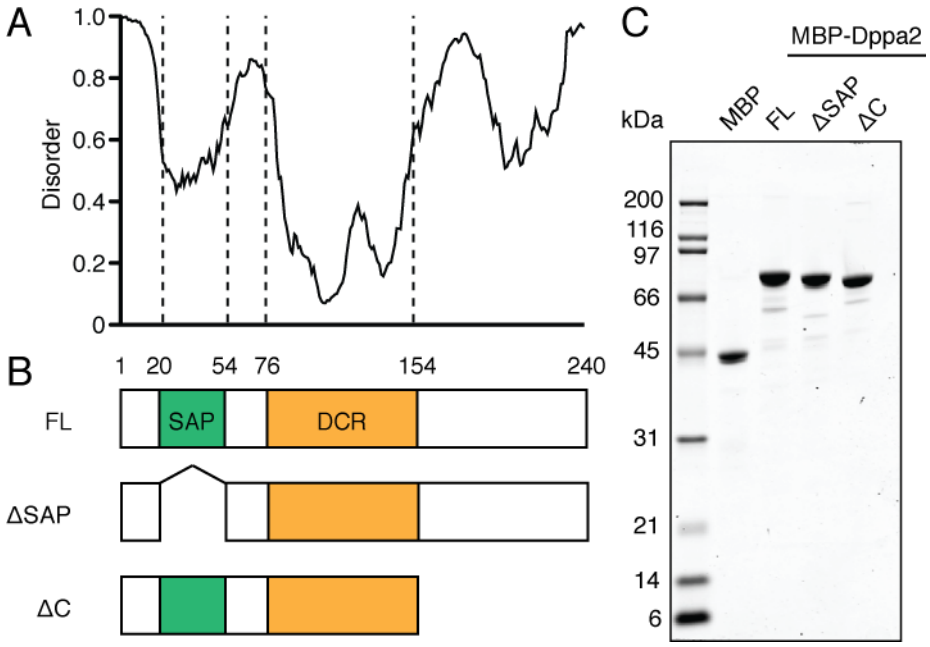

Figure 3-9. Dppa2 truncation mutants

(A) Protein disorder predicted by PONDR-FIT (Xue et al., 2010). The SAP and DCR domains are bounded by regions of high disorder.

(B) Dppa2 domain deletion mutants used in this Chapter.

(C) Purity of recombinant MBP-tagged Dppa2 proteins, analyzed by SDS-PAGE and Coomassie staining.

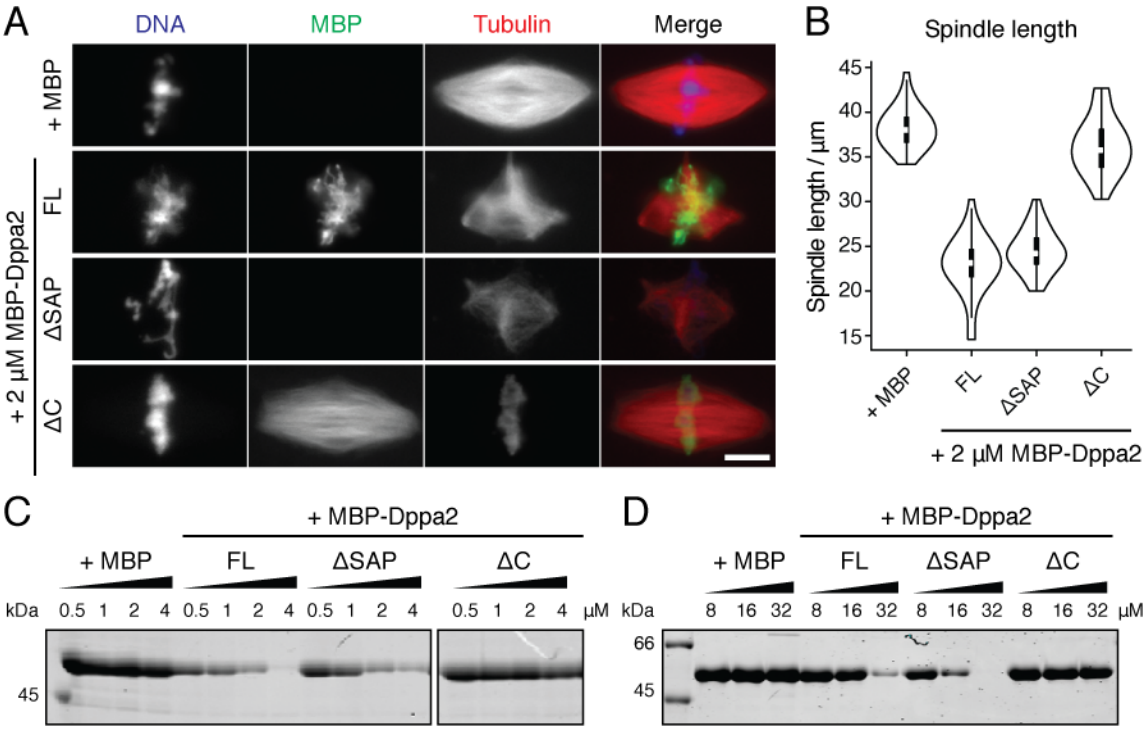

Figure 3-10. Dppa2 requires its C terminus but not DNA binding to inhibit microtubule assembly

(A) Spindle assembly in the presence of 2 µM recombinant MBP-tagged Dppa2 protein. Dppa2 localization was visualized by immunofluorescence with anti-MBP antibody (NEB E8032, 1 µg/ml). Scale bar, 10 µm.

(B) Quantification of spindle length from (A). Each column represents mean and standard error from 30 spindles.

(C) Chromatin-independent microtubule assembly in *Xenopus* egg extracts. Extracts were treated with DMSO (5%) and microtubule polymer recovered by pelleting.

(D) Polymerization of purified MAP-free bovine tubulin. Tubulin was treated with DMSO (5%) and microtubule polymer recovered by pelleting.

microtubule assembly, either in *Xenopus* egg extracts (Figure 3-10, A-C) or from purified tubulin (Figure 3-10D). As we expected (Figure 2-12), Dppa2 does not have to be bound to DNA to suppress microtubule polymerization, and our deletion mutants allow separation of these dual functions. The C-terminal domain is not well conserved in other species (Figure 1-4), suggesting that Dppa2 in these species may lack this microtubule-regulatory role. This would be consistent with the hypothesis that mammalian Dppa2 is a transcription factor and epigenetic regulator (Nakamura et al., 2011).

3.6. Dppa2 must be localized to chromatin for nuclear formation

The strict localization of Dppa2 to chromatin despite its function in regulating microtubule assembly suggested that it might be specifically responsible for suppressing microtubules in the vicinity of chromosomes. To test this hypothesis we asked whether the DNA-binding and microtubule-regulatory activities of Dppa2 were both required to support nuclear assembly. This was confirmed by depletion and add-back experiments, in which neither Dppa2$^{\Delta SAP}$ nor Dppa2$^{\Delta C}$ were able to rescue nuclear assembly in ΔDppa2 extracts (Figure 3-11). Taken together, our data illustrate a requirement for spatially and temporally restricted microtubule dynamics during nuclear formation, mediated by chromatin-bound Dppa2.

3.7. Nuclear assembly in ΔDppa2 extracts is not rescued by Xkid depletion or dynein inhibition

We reasoned that motor protein activity might contribute to the nuclear deformation defect in ΔDppa2 extracts, by tearing nascent nuclear membranes or applying forces directly to chromatin that have yet to assembly a protective lamina. Xkid is a chromokinesin that coats chromatin and promotes metaphase chromosome alignment by

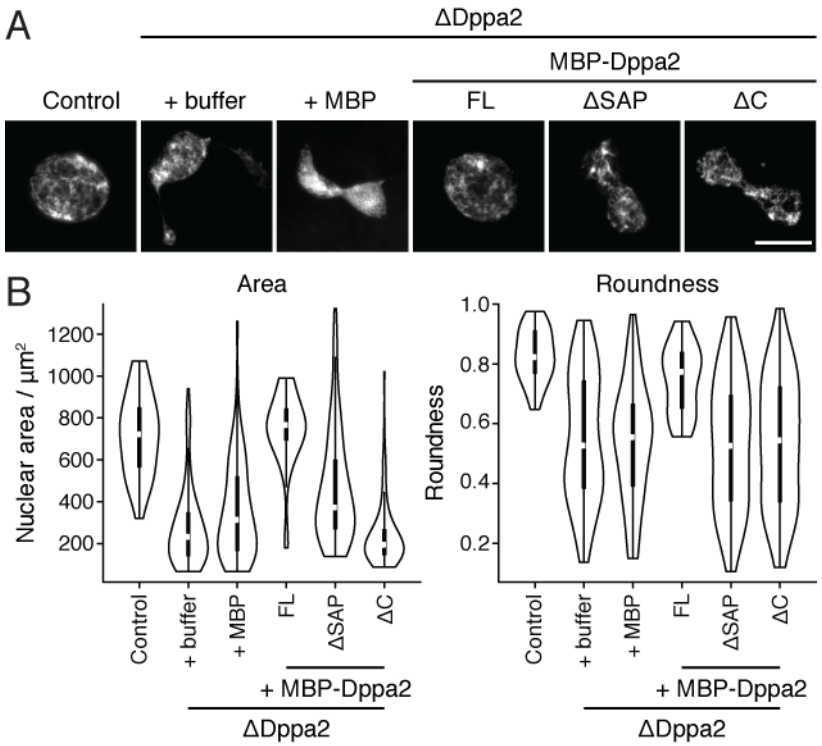

Figure 3-11. Nuclear assembly requires localized microtubule disassembly by chromatin-bound Dppa2

(A) Nuclear assembly in control and ΔDppa2 extracts, supplemented with recombinant MBP-tagged proteins (400 nM). Nuclei were imaged 60 min after calcium addition. Scale bar, 10 μm.

(B) Quantification of nuclear size and shape from (A), n > 30 for each condition.

Figure 3-12. Nuclear assembly in ΔDppa2 extracts is not rescued by Xkid depletion or dynein inhibition

(A) Efficiency of Xkid and Dppa2 depletion assessed by western blotting using anti-Dppa2 and anti-Xkid (1 μg/ml) antibodies.

(B) Nuclei assembled in extracts shown in (A) were fixed and imaged at 60 min after calcium addition. Each column represents mean of >60 nuclei, error bars indicate 95% confidence intervals.

(C) Recombinant p50/dynamitin purified from *E. coli* and analyzed by Coomassie staining.

(D) Nuclear assembly in extracts treated with recombinant p50/dynamitin (20 μM). Scale bar, 10 μm.

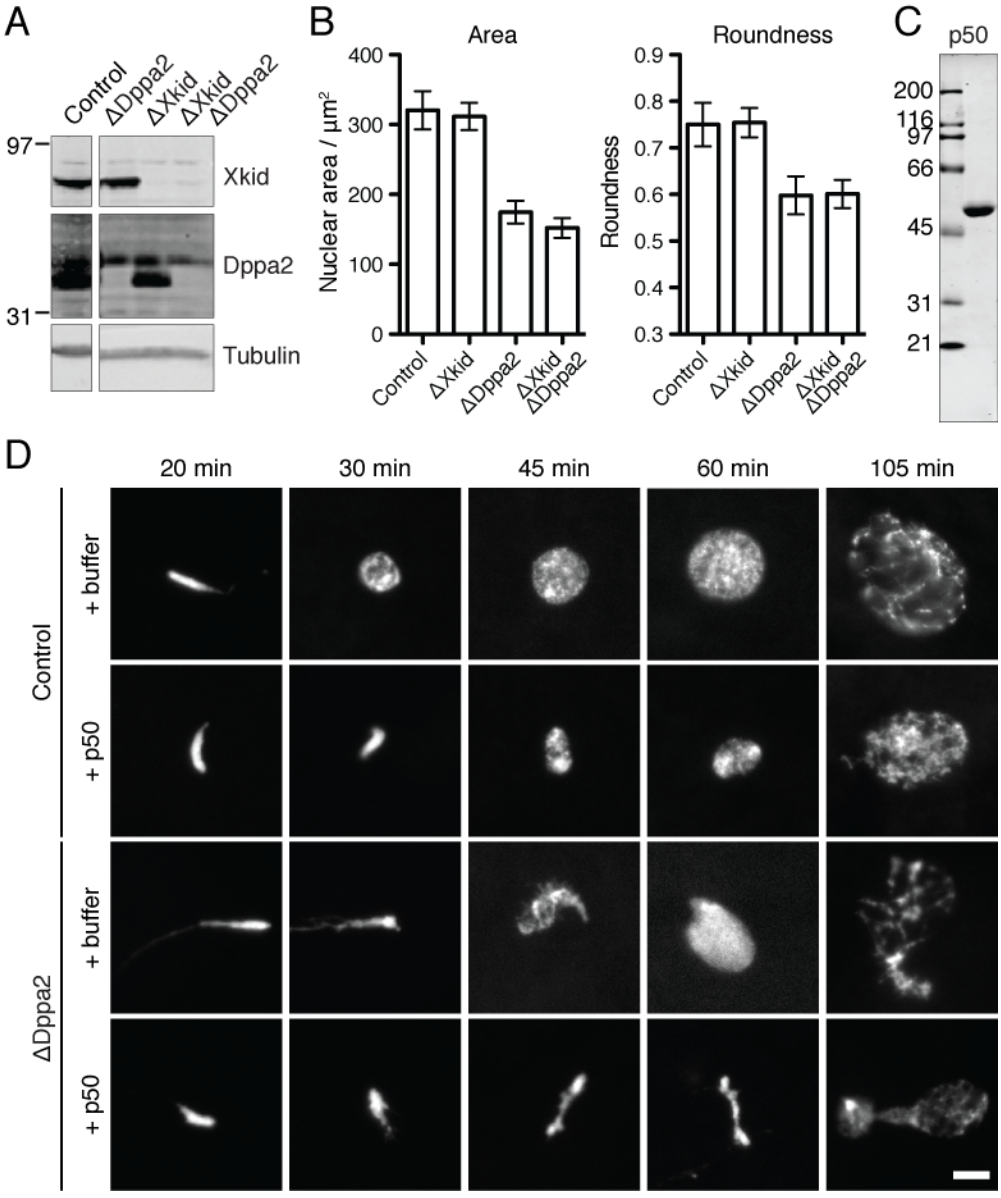
A
Control
ΔDppa2
ΔXkid
ΔXkid ΔDppa2
97
31
Xkid
Dppa2
Tubulin
B
Area
Nuclear area / μm²
400
300
200
100
0
Control
ΔXkid
ΔDppa2
ΔXkid ΔDppa2
Roundness
Roundness
0.9
0.8
0.7
0.6
0.5
0.4
0.3
C
p50
200
116
97
66
45
31
21
D
20 min
30 min
45 min
60 min
105 min
Control
+ buffer
+ p50
ΔDppa2
+ buffer
+ p50

pushing chromosome arms toward the metaphase plate (Funabiki and Murray, 2000; Antonio et al., 2000). Depletion of Xkid did not interfere with normal nuclear assembly in control extracts nor rescue nuclear defects in ΔDppa2 extracts (Figure 3-12, A and B). This was not wholly unexpected since the bulk of Xkid protein is degraded in anaphase (Funabiki and Murray, 2000; Antonio et al., 2000), and therefore unlikely to contribute significantly to nuclear deformation in interphase.

Dynein was a more compelling candidate since it is responsible for the bulk of microtubule-dependent membrane trafficking in *Xenopus* egg extracts, and dynein-dependent tearing is strong enough to tear the nuclear envelope during mitotic entry (Beaudouin et al., 2002; Salina et al., 2002; Wang et al., 2013). During M phase, high mitotic phosphorylation releases dynein from membranes, but these attachments would be expected to re-form during nuclear assembly (Niclas et al., 1996). However, inhibition of dynein by adding recombinant p50/dynamitin (Wittmann and Hyman, 1999) failed to rescue and indeed exacerbated nuclear assembly defects in ΔDppa2 extracts (Figure 3-12C). The same treatment also led to reduced nuclear size in control extracts. We infer from these results that dynein-dependent membrane trafficking contributes positively to nuclear assembly by delivering membranes. If any dynein-dependent nuclear damage took place, it was apparently compensated by this effect.

Chapter 4. Regulation of microtubule dynamics by Dppa2

4.1. Dppa2 does not bind detectably to microtubules or free tubulin

Although we had not thus far detected any Dppa2 localization to spindle or aster microtubules, we attempted three further experiments to rule out this possibility. First, we pelleted microtubules from *Xenopus* egg extracts to purify microtubule-binding proteins, and recovered only background levels of Dppa2 compared to bona fide MAPs (Figure 4-1A). Second, we immunoprecipitated Dppa2 from egg extracts to detect any interaction with soluble tubulin, and found neither α-tubulin nor γ-tubulin (Figure 1-2B). Third, we asked whether Dppa2 could interact with purified tubulin, in which case we should be able to detect a Dppa2-tubulin complex with a higher apparent molecular weight than either protein alone (Belmont and Mitchison, 1996). However, when mixed together neither Dppa2 nor tubulin showed any molecular weight shift (Figure 4-1, C and D).

4.2. In vitro microtubule dynamics assay

Dppa2 suppresses microtubule assembly both in *Xenopus* egg extracts and from purified tubulin (Figures 2-9 and 2-10), although we noted that a higher concentration of Dppa2 was required to inhibit DMSO-induced polymerization of purified tubulin than in egg extracts (compare Figure 2-12A with Figure 2-12B). We can reconcile this because the in vitro experiment does not recapitulate physiological microtubule dynamics; in the absence of microtubule regulators, microtubules are more stable (Kinoshita et al., 2001), and adding DMSO tilts the reaction away from equilibrium in favor of polymerization. As a result, catastrophes are negligible and we typically recover greater than 90% of the available tubulin in these conditions. In order to measure the effect of Dppa2 in more physiological conditions, we omitted DMSO from future experiments.

Figure 4-1. No evidence of Dppa2 interaction with microtubules or tubulin

(A) Extracts containing MBP or MBP-Dppa2 (2 μM) fusion proteins were treated with taxol (5 μM) and incubated at 20 °C for 1 h. Polymerized microtubules were recovered by pelleting through a glycerol cushion, and microtubule-bound proteins analyzed by western blotting with anti-MBP (NEB E8032; 0.1 μg/ml), anti-α-tubulin (Sigma T9026; 1/20,000), anti-Xorbit (gift of Rebecca Heald; 1/6,000), anti-MCAK (gift of Ryoma Ohi; 2 μg/ml), anti-γ-tubulin (Sigma T3320; 1/10,000) and anti-H3 (Abcam ab1791; 1/1,000) antibodies.

(B) MBP or MBP-Dppa2 (4 μM) was added to extracts and incubated at 20 °C for 1 h, then immunoprecipitated with anti-MBP antibody. Dppa2-binding proteins were probed by western blotting.

(C) MBP-Dppa2 and purified bovine tubulin (10 μM each) were mixed together or incubated alone at 37 °C for 10 min. Protein species were separated by native molecular weight by gel filtration on a Superose 6 10/300 GL column.

(D) Fractions collected from gel filtration in (C) were stained with Coomassie.

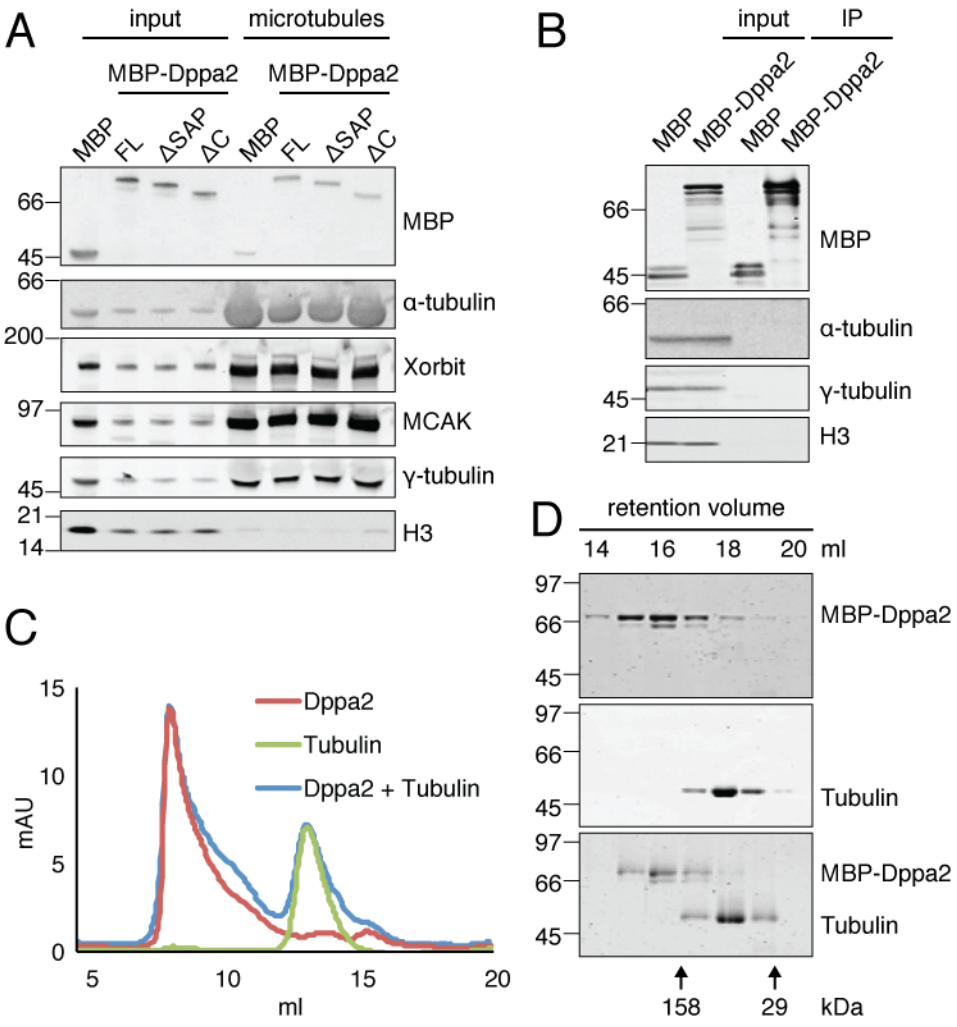
A
input
microtubules
MBP-Dppa2
MBP-Dppa2
MBP
FL
ΔSAP
ΔC
MBP
FL
ΔSAP
ΔC
66
45
66
200
97
45
21
14
MBP
α-tubulin
Xorbit
MCAK
γ-tubulin
H3
B
input
IP
MBP
MBP-Dppa2
MBP
MBP-Dppa2
66
45
66
45
21
MBP
α-tubulin
γ-tubulin
H3
C
15
10
5
0
mAU
5
10
15
20
ml
Dppa2
Tubulin
Dppa2 + Tubulin
D
retention volume
14
16
18
20
ml
97
66
45
97
66
45
97
66
45
MBP-Dppa2
Tubulin
MBP-Dppa2
Tubulin
158
29
kDa

In the absence of DMSO there is however a nucleation barrier to polymerization. This can be overcome by forming short microtubule 'seeds' in the presence of the non-hydrolyzable GTP analog GMPCPP. Seeds are immobilized inside home-made flow cells, and excess GMPCPP washed out and replaced with GTP-tubulin to grow extensions that exhibit dynamic instability (Figure 4-2). Seeds and extensions can be distinguished using tubulin labeled with different fluorophores, or alternatively a single fluorophore at different brightness. To reduce background fluorescence from unincorporated tubulin, the flow cell is visualized with total internal reflection fluorescence (TIRF) illumination.

4.3. Dppa2 is a microtubule catastrophe factor

In contrast to earlier results, where 32 μM Dppa2 was required to suppress DMSO-induced microtubule polymerization (Figure 2-12B), as little as 1 μM Dppa2 strongly inhibited microtubule growth from GMPCPP-stabilized seeds (Figure 4-3A). As expected, the C terminus of Dppa2 was required for this effect. Suppression of microtubule growth by Dppa2 was dose-dependent, and at higher concentrations of Dppa2 we could no longer detect any extensions on the majority of seeds within the 10 min timescale of the experiment (Figure 4-3B).

Given the unambiguous suppression of dynamic microtubule growth by Dppa2, we wished to determine whether Dppa2 regulated growth velocity or catastrophe frequency. We did not closely examine two further dynamics parameters, namely rescue frequency and shrinkage velocity. Rescue frequency is often excluded in many studies because rescue events are extremely rare in vitro; since rescue frequency is already close to zero (Walker et al., 1988), a further reduction in rescue frequency was unlikely to

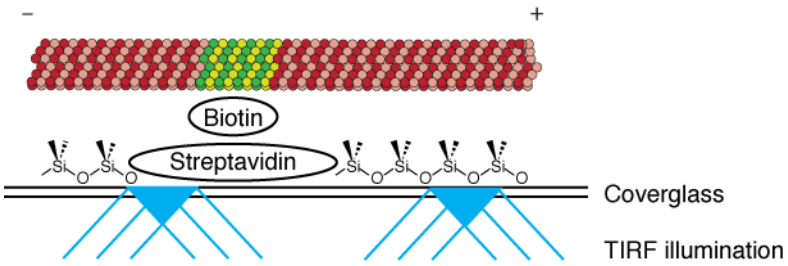

Figure 4-2. TIRF microscopy-based microtubule dynamics assay

GMPCPP-stabilized microtubule seeds labeled with biotin and Alexa Fluor 488 (green) are immobilized onto silane-passivated coverslips by biotin-streptavidin linkage. Dynamic microtubule extensions are grown off the seeds from rhodamine-labeled tubulin monomers (red).

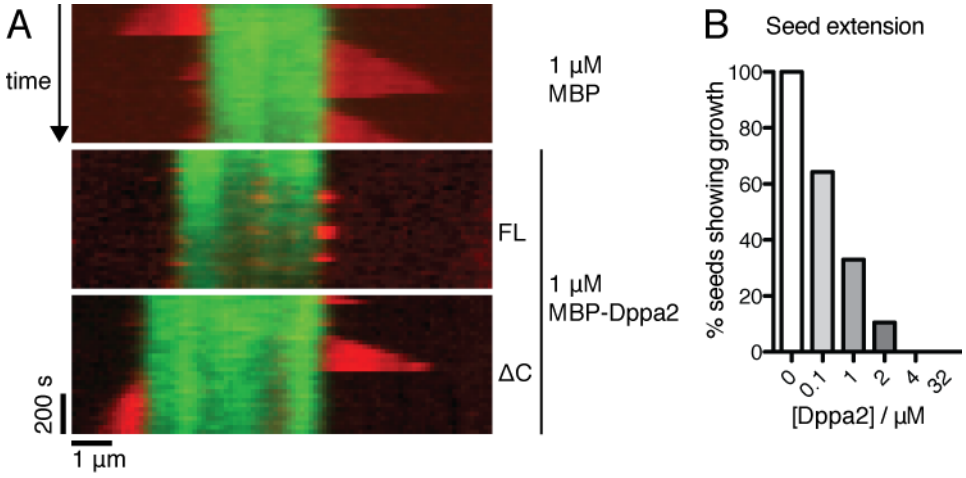

Figure 4-3. Dppa2 inhibits dynamic microtubule growth

(A) GMPCPP-stabilized seeds (green) were incubated in the presence of MBP-tagged Dppa2 (1 µM) and GTP-tubulin (12 µM; red) at 37 °C and imaged at 20 s intervals for 10 min. Time-lapse images are shown as kymographs.

(B) Proportion of seeds from which any microtubule growth was detected over a 10 min period in the presence of Dppa2. >30 seeds were counted in each condition.

explain the depolymerizing effect of Dppa2. We excluded shrinkage velocity because microtubule extensions were extremely short in the presence of Dppa2, and so tended to depolymerize completely during the interval between two successive frames of time-lapse imaging (Figure 4-3A), making it difficult to estimate the shrinkage velocity accurately.

In the absence of Dppa2, we observed microtubule growth from both ends of GMPCPP seeds, and the plus end was easily distinguished from the minus end because it was more dynamic and grew to greater lengths (Figure 4-4A). However, in the presence of Dppa2, we typically only found microtubule growth on one side of the seed, which we assumed to be the plus end. We therefore focused our attentions solely on plus end dynamics. For similar reasons, we measured microtubule dynamics in the presence of a relatively low Dppa2 concentration (100 nM), since microtubule extensions are too short-lived at higher concentrations to measure even growth rates or catastrophe frequencies.

This analysis revealed that 100 nM Dppa2 did not alter microtubule growth rates but increased catastrophe frequency by 50% (Figure 4-4B; Table 4-1). The magnitude of this effect is comparable to that of Op18/stathmin, which increases catastrophe frequency 5-10 fold at a concentration of 3.4 μM (Belmont and Mitchison, 1996). However, Dppa2 was less potent than the kinesin-8 Kip3 or MCAK, which achieve similar increases in catastrophe at concentrations in the range of 10 nM (Gardner et al., 2011).

4.4. Dppa2 depolymerase activity requires GTP hydrolysis

We performed a complementary experiment by asking whether Dppa2 continues to inhibit microtubule growth in the presence of GMPCPP. Addition of GMPCPP does not alter microtubule growth rate but eliminates catastrophe (Hyman et al., 1992), and so

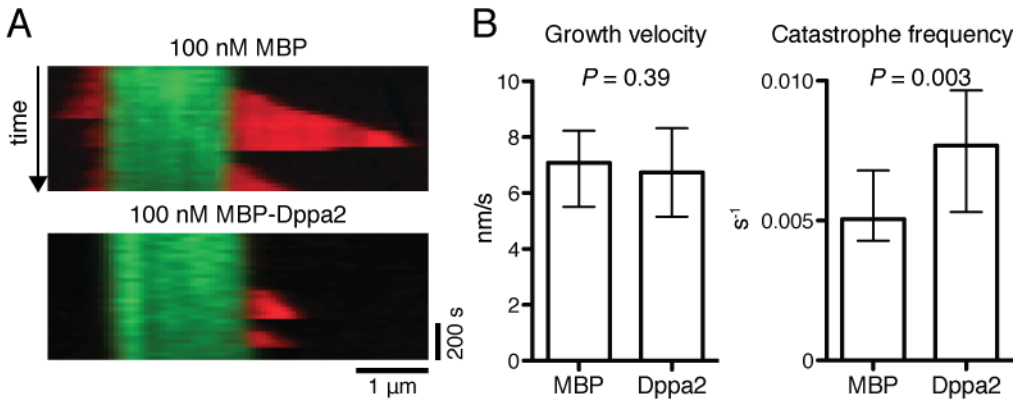

Figure 4-4. Dppa2 promotes microtubule catastrophe

(A) GMPCPP-stabilized seeds (green) were incubated in the presence of MBP-tagged Dppa2 (100 nM) and GTP-tubulin (12 µM; red) at 37 °C.

(B) Mean growth velocities and catastrophe frequencies (MBP: n = 24; Dppa2: n = 18). Error bars represent 95% confidence intervals obtained by bootstrapping.

Table 4-1. Microtubule dynamics parameters

	Growth rate (nm/s)	Catastrophe frequency (s^{-1})
MBP	7.08	0.0051
Dppa2	6.74	0.0077

should suppress the catastrophe-promoting activity of Dppa2. Catastrophe is thought to depend on GTP hydrolysis and loss of the GTP cap (Figure 1-3). Consistently, while Dppa2 could completely eliminate dynamic microtubule growth in the presence of GTP (Figure 4-3), it had a much smaller effect in the presence of GMPCPP (Figure 4-5). GMPCPP also restored microtubule growth at the minus end in the presence of Dppa2.

One explanation for these data is that Dppa2 could block nucleotide exchange in tubulin, preventing GTP loading and recycling of tubulin monomers. However, tubulin was still able to load radiolabeled GTP in the presence of Dppa2 (Figure 4-6). Moreover, Dppa2 did not itself bind stoichiometric quantities of GTP, making it less likely that Dppa2 could harbor any intrinsic GTPase activity that depletes the pool of GTP available for tubulin polymerization. We do not expect Dppa2 to contain GTPase activity, since we have not found any sequence homology with known GTPases. Dppa2 may instead act as a GTPase-activating protein (GAP) for the GTPase activity of tubulin. It is known for example that nocodazole increases the GTPase activity of tubulin in solution (Larsson et al., 1999), but we do not favor this model for Dppa2 since it would deplete the pool of GTP-tubulin and should therefore reduce microtubule growth rates. Instead, Dppa2 may accelerate GTP hydrolysis in the microtubule lattice, increasing the likelihood of losing the GTP cap and hence the frequency of catastrophe.

4.5. Mammalian Dppa2 and Dppa4 do not inhibit microtubule assembly

No overt microtubule-related phenotypes have been reported in mammalian cells for either depletion or overexpression of the orthologs of Dppa2 (Ivanova et al., 2006; Madan et al., 2009; Du et al., 2010; Nakamura et al., 2011; Tung et al., 2013). Moreover, the C-terminal domain of *Xenopus* Dppa2 that confers microtubule suppression is not

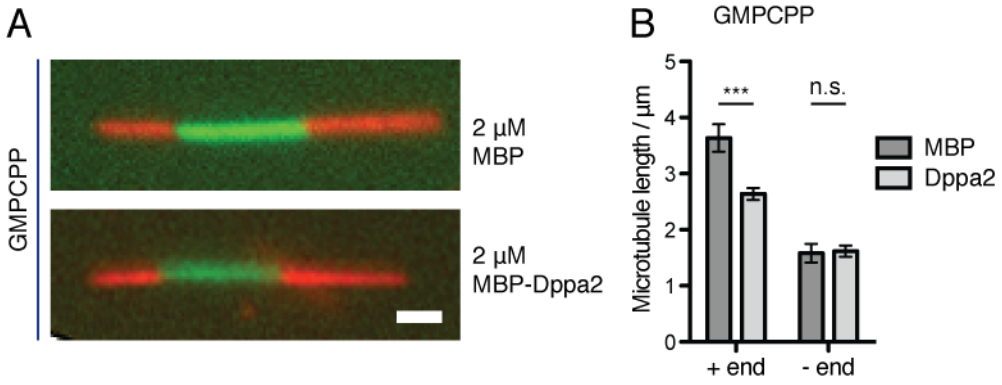

Figure 4-5. Dppa2 does not depolymerize microtubules in the presence of GMPCPP

(A) GMPCPP-stabilized seeds (green) were immobilized onto coverslips, washed and incubated with MBP-tagged Dppa2 (2 µM), fresh GMPCPP (1 mM) and tubulin (2 µM; red) for 1 h at 37 °C. Scale bar, 1 µm.

(B) Quantification of microtubule lengths from (A). Each column indicates mean of >36 microtubules, error bars indicate 95% confidence intervals. (+) end, $P < 0.0001$; (-) end, $P = 0.70$.

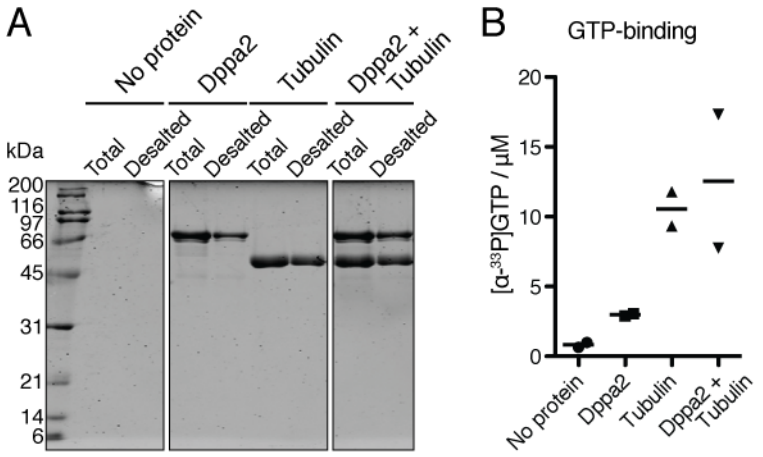

Figure 4-6. Dppa2 does not bind GTP or interfere with tubulin GTP exchange

MBP-Dppa2 and tubulin (15 µM each) were loaded with [α-^{33}P]GTP (1 mM, 1.3 Bq/µl) and incubated on ice for 1 h. Proteins were separated from unincorporated GTP using Micro Bio-Spin P-6 desalting columns (Bio-rad 732-6221).

(A) Recovery of proteins after desalting shown by Coomassie staining.

(B) Concentration of GTP bound to proteins measured by scintillation counting. Data shown are counts from two independent experiments.

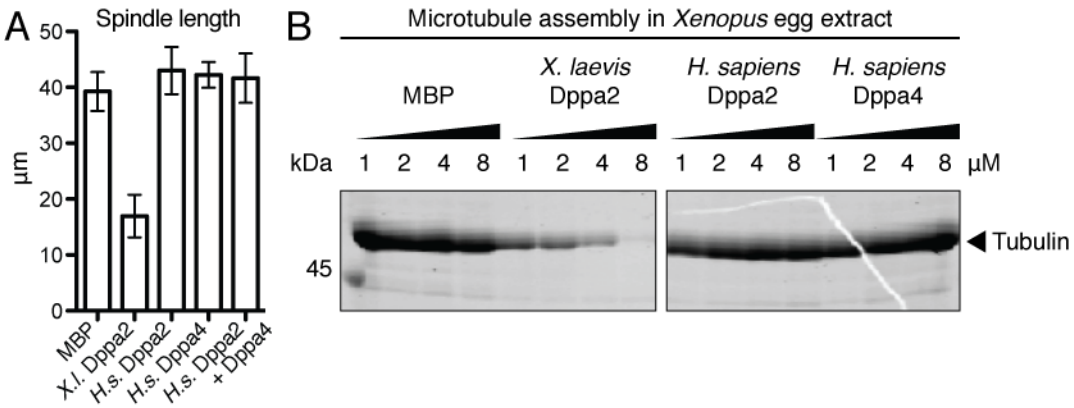

Figure 4-7. Human Dppa2 and Dppa4 do not inhibit microtubule assembly

(A) Length of spindles assembled in *Xenopus* egg extracts supplemented with MBP-tagged proteins (4 µM). Error bars indicate 95% confidence intervals of the mean. Data in this figure and Figure 3-10B came from the same experiment, n>30 for each condition.

(B) DMSO-induced microtubule assembly in *Xenopus* egg extracts supplemented with recombinant MBP-tagged proteins. Data in this figure and Figure 3-10C came from the same experiment.

well conserved in mammals (Figure 1-4). We purified human Dppa2 and Dppa4 proteins from *E. coli*, and tested their ability to inhibit microtubule assembly both alone and added together, since they have been reported to form a complex (Rual et al., 2005; Tung et al., 2013). As expected, neither protein suppressed spindle assembly or DMSO-induced microtubule polymerization (Figure 4-7).

Chapter 5. Discussion

5.1. Nuclear assembly is shaped by microtubule dynamics

The work described in this thesis and published elsewhere (Xue et al., 2013; Xue and Funabiki, 2014) demonstrates a requirement for spatial and temporal control of microtubule dynamics during nuclear assembly. In *Xenopus* egg extracts, this control is locally mediated around chromatin by chromatin-bound regulators such as the CPC, to the list of which we now add the novel microtubule catastrophe factor Dppa2. Nuclear assembly takes place in a regime of finely balanced microtubule dynamics, and upsetting this balance in either direction can compromise nuclear shape and size. Our results pertain specifically to the processes of fertilization and pronuclear formation, but establish principles that generalize to mitotic cell division.

We showed that Dppa2 was required for nuclear assembly and suppressed local microtubule polymerization. In the absence of Dppa2, sperm chromosomes were associated with greater microtubule density and subsequently formed smaller nuclei with abnormal morphology (Figure 2-3 and Figure 2-9). These nuclei incorporated less lamin and fewer NPCs (Figure 2-4), and showed delayed and disorganized DNA replication (Figure 2-5). However, normal nuclear size, shape and replication could be restored by treatment with a titrated amount of nocodazole (Figure 3-5), suggesting that these nuclear defects were the result of excessive microtubule polymerization.

We propose three non-mutually exclusive mechanisms through which microtubules could interfere with nuclear assembly (Figure 5-1). First, microtubules may physically obstruct recruitment of membranes and closure of the nuclear envelope. Second, microtubule-dependent shear forces and motor protein activity may tear the

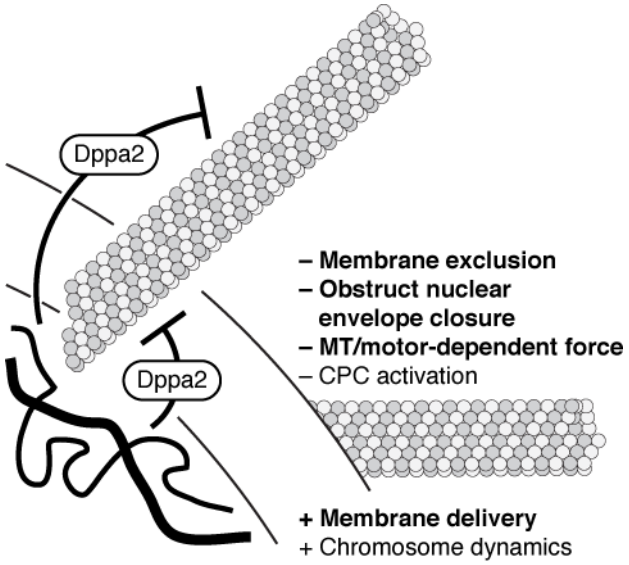

Figure 5-1. Microtubules play both positive and negative roles in nuclear formation
Nuclear assembly requires tightly balanced microtubule dynamics and is sensitive to both positive (+) and negative (–) influences. While excess microtubules inhibit nuclear formation by obstructing nuclear envelope closure and/or damaging nascent nuclei through motor proteins and shear forces, abolishing microtubules impedes delivery of membranes and nuclear expansion. Key factors involved in nuclear deformation in ΔDppa2 extracts are highlighted in bold.

nuclear envelope and/or deform nascent nuclei. Third, the CPC is activated by microtubules and could delay nuclear formation by inhibiting chromosome decondensation.

Physical obstruction delays membrane recruitment

Studies in human cells showed that the initial binding of nuclear envelope proteins to anaphase chromosomes tends to exclude regions of high microtubule density (Chaudhary and Courvalin, 1993). Similarly, ER membranes are excluded by mitotic spindle fibers, and ER recruitment to chromosomes is delayed by taxol treatment (Lu et al., 2011). This is likely to be a combination of both passive exclusion and proteins such as REEP3/4 and SUN1/2 that actively clear membranes away from the spindle (Smyth et al., 2012; Schlaitz et al., 2013; Turgay et al., 2014). During the final steps of nuclear envelope closure, microtubule remnants can be seen occupying gaps in the membrane (Haraguchi et al., 2008).

Nuclear size is driven primarily by import rates, and can continue indefinitely in *Xenopus* egg extracts, which behave as cells of infinite volume since they have no plasma membrane (Gant et al., 1999; Levy and Heald, 2010). Failure to seal the nuclear envelope and establish a nuclear permeability barrier would preclude accumulation of lamins and other cargos, resulting in decreased nuclear size. Insufficient import of DNA replication factors also explains delays in replication. Nuclei assembled in ΔDppa2 extracts showed clearly reduced lamin recruitment, consistent with such an import delay. Moreover, the staining was patchy, suggesting that not all regions of the nuclear envelope sealed at the same time. At later time points this resulted in uneven nuclear expansion, contributing to the nuclear shape defect (Figure 2-4A).

We were largely unsuccessful in our efforts to visualize this process through dual-color live imaging of microtubules and nuclei (Figure 2-1). Microtubules in *Xenopus* egg extracts were too dense to resolve, and are not suited to deconvolution-based superresolution imaging strategies such as structured illumination microscopy. Although lipophilic membrane dyes bleached rapidly (see Appendix A), they remain promising for use under lower intensity illumination, and we also had some success visualizing the nuclear envelope assembly with fluorescently-labeled antibodies against NPCs (Figure 2-1B). Nonetheless, electron microscopy may be the better approach, sacrificing time resolution to visualize single microtubules in the context of the nascent pronucleus. This would help establish the timing of nuclear envelope closure in ΔDppa2 extracts and confirm whether patchy lamin and NPC recruitment are caused by microtubule obstruction.

Microtubule-dependent forces deform nuclei

Microtubules can exert significant force on chromosomes. Kinetochore fibers are strong enough to break dicentric chromosomes that bridge the cleavage plane (Gisselsson et al., 2000), and as soon as the nuclear envelope begins to form it creates a growing platform for binding to microtubules. Microtubules are highly dynamic during M phase, and exert forces strong enough to tear the mature nuclear envelope (Beaudouin et al., 2002; Salina et al., 2002; Turgay et al., 2014). Although interactions between microtubules and membranes are reduced in M phase by mitotic phosphorylation of dynein and STIM1 (Niclas et al., 1996; Smyth et al., 2012), they are re-established as Cdk1 activity declines, at a time when chromosomes are still associated with many microtubules.

Mitotic chromosomes are highly condensed and resistant to shear forces. However, in the early stages of nuclear assembly chromosomes begin to decondense and become more easily deformed, before they have acquired a sufficiently strong lamina to buffer against physical stress. We know that chromosomes undergo extensive motion during pronuclear assembly, initially pushed outward by the dense aster and later pulled back in by dynein activity (Figure 2-1), and so are likely to experience significant viscous friction. Lamina weakness is exacerbated in ΔDppa2 extracts, where nuclei will therefore be particularly susceptible to physical damage. We frequently saw a stretched morphology in these nuclei, with a thin, distended appearance on the side closest to the centrosome (e.g. Figure 2-4A). We note also that while taxol treatment lead to nuclear shape defects, these nuclei rarely had the stretched appearance of nuclei assembled in ΔDppa2 extracts (Figure 3-3). We suggest that this may because taxol-induced microtubules are dense but stable, and may not subject nuclei to the same dynamic forces that are experienced in ΔDppa2 extracts. Collectively, these results argue for a contribution from microtubule forces to nuclear deformation.

We attempted to address the impact of motor proteins by depleting the chromokinesin Xkid and by inhibiting dynein with recombinant p50/dynamitin (Figure 3-12). Xkid had no impact on nuclear size or shape, but dynein inhibition delayed nuclear expansion in both control and ΔDppa2 extracts. We interpret this result as a consequence of reduced membrane delivery in dynein-inhibited extracts (see below, 'Microtubules promote nuclear assembly by delivering membranes'). However, we suggest that if we can reduce dynein processivity without abolishing function completely, we may lessen the microtubule-dependent forces experienced by nascent nuclei without severely

impacting membrane delivery, similar to rescue of nuclear assembly using a low dose of nocodazole (Figure 3-5). This may require a lower titer of p50, which disrupts the dynactin complex that promotes dynein localization, or alternatively small molecular direct inhibitors of dynein (Firestone et al., 2012). In addition, other motors may be important, especially kinesins that would be pulling on membranes and chromatin in the opposite direction to dynein and hence compounding microtubule-dependent stresses.

Contribution of the CPC

The CPC inhibits chromosome decondensation in anaphase (Mora-Bermúdez et al., 2007; Neurohr et al., 2011), and retention of the CPC on chromosomes delays nuclear formation (Ramadan et al., 2007; Kelly et al., 2010; Afonso et al., 2014). The CPC also promotes microtubule polymerization around chromatin, and codepletion of the CPC rescued both the phenotypes of increased microtubule mass and abnormal nuclear shape in ΔDppa2 extracts (Figure 3-1), indicating that Dppa2 and the CPC antagonize one another. Initially we hypothesized that Dppa2 might directly suppress the CPC, thereby explaining the increased microtubule stability and delayed nuclear formation in ΔDppa2 extracts. We eliminated this possibility upon discovering that Dppa2 can still suppress microtubule formation in the absence of chromatin (Figure 2-12A), in the absence of the CPC (Figure 3-2D) and in vitro (Figure 2-12B).

Nonetheless, the CPC is activated by microtubules (Tseng et al., 2010; Tan and Kapoor, 2011; Campbell and Desai, 2013), and it is possible that increased microtubule density in ΔDppa2 extracts could stimulate CPC-dependent inhibition of chromatin decondensation, contributing to the nuclear defect. We examined CPC localization and CPC-dependent substrate phosphorylation following both depletion (Figure 2-6, B and C)

and overexpression of Dppa2 (Figure 3-2, A – C), but did not detect any change. We surmise therefore that microtubule-dependent stimulation of CPC activity was not a cause of nuclear assembly defects in ΔDppa2 extracts.

A difficulty remains because enhanced sperm aster assembly in ΔDppa2 extracts was fully rescued to control levels by CPC codepletion (Figure 3-1, B and C), yet only nuclear shape and not nuclear size were rescued (Figure 3-1, D and E). We only analyzed aster size at a single time point, and may have lacked the temporal or spatial resolution to determine whether CPC codepletion truly was a perfect counterbalance to Dppa2 depletion. These two pathways of microtubule regulation are independent (Figure 3-2D), and it is possible that at another time point that is more critical to nuclear assembly microtubule dynamics in ΔCPCΔDppa2 extracts were not exactly equal to control extracts. By the same token, we examined whole asters and may not have measured the most relevant population of microtubules, which is to say those in the immediate vicinity of chromosomes. Although both Dppa2 and the CPC are localized on chromatin, they may have different binding and diffusion kinetics that affect the distances over which they act.

Microtubules promote nuclear assembly by delivering membranes

We observed that high concentrations of nocodazole that abolished microtubule assembly resulted in slower nuclear expansion (Figure 3-3). We attribute this to the role of microtubules in delivering ER membranes to the nascent nucleus. Formation of the tubular ER network does not depend on microtubules and can take place in the presence of nocodazole (Dreier and Rapoport, 2000), but under these conditions the ER forms a spatially homogenous pattern that does not distinguish cellular landmarks. Microtubules

break the symmetry of this network by promoting motor-dependent directed motion of ER tubules. In particular, engagement of dynein transports both ER tubules (Wang et al., 2013) and the nascent nucleus (Figure 2-1) towards the center of the centrosome and consequently towards each other. This explains our observation that while perfectly spherical nuclei can form in the presence of high concentrations of nocodazole, nuclear expansion is significantly enhanced when microtubules are present (Figure 5-1).

5.2. Temporal and spatial balance of microtubule dynamics during nuclear formation

In the above section we discussed possible mechanisms by which microtubules could impinge on nuclear assembly, both positively and negatively. We concluded that loss of nuclear size and shape in ΔDppa2 extracts is likely caused by a combination of physical blockage of membrane recruitment, leading to delayed and uneven nuclear envelope closure, weakened lamina and susceptibility to microtubule-dependent shear force (Figure 5-1). However, we also found that nuclear assembly was uniquely sensitive to perturbations of microtubule dynamics during a limited time window, and moreover Dppa2 localization is essential to its function in supporting nuclear formation. Here we discuss these requirements for spatial and temporal control of microtubules, with specific reference to fertilization and pronuclear assembly.

Temporal control of microtubule dynamics

The period during which nuclear assembly is most sensitive to altered microtubule dynamics is essentially exactly at the transition from M phase to interphase (Figure 3-6). We attribute this phenomenon to the rapid assembly of microtubules around chromosomes during the sensitive window, when Cdk1 activity is still high, which

sensitizes nuclei to further microtubule perturbations. After the window closes, we suggest that two effects take place. The first is straightforward: once mitotic kinase activity is extinguished, microtubules stabilize and nuclei experience lesser forces and smaller perturbations from microtubules. In this state, nuclei are mostly left alone to expand through continuous import and membrane incorporation (Levy and Heald, 2010; Wang et al., 2013). The second effect is more complex, because nuclear morphology appears to become fixed early on in nuclear assembly, either during the M phase-to-interphase transition or very soon after. At 30 min after release from metaphase, inducing ectopic microtubules no longer perturbs nuclear shape, nor does nocodazole rescue nuclear shape in ΔDppa2, extracts even at high doses (Figure 3-6). Along the same lines, we suspect that the uneven swelling of nuclei in ΔDppa2 extracts reflects patchy recruitment of membranes and NPCs early on; the regions that successfully assembled membranes and NPCs will swell continuously, whereas regions that didn't will not.

This is due to the positive feedback effect of continuous nuclear import, so regions with higher NPC density at one time point will assemble more NPCs in future, ad infinitum. However, there is an additional nuance in the cell cycle-dependence of NPC assembly. NPCs are assembled starting from M phase exit but also continuously loaded in interphase, leading to a doubling of NPC number during G1. When Cdk1 activity is high, even if the nuclear membrane is not complete NPC assembly is driven by direct recruitment of the nucleoporin ELYS to nucleosomes (Maeshima et al., 2010; Inoue and Zhang, 2014; Zierhut et al., 2014). This recruits the essential Nup107/160 complex to promote assembly of the rest of the NPC (Harel et al., 2003a; Walther et al., 2003a). However, ELYS is no longer properly localized once Cdk1 activity falls. In interphase,

NPC assembly relies instead on Pom121 to recruit Nup107/160 (Doucet et al., 2010). Pom121 inserts into existing membranes via its curvature-sensing domain, and may be disfavored on the distended surface of nuclei assembled in ΔDppa2 extracts, amplifying the positive feedback effect of earlier exclusion.

Hence, if early nuclear envelope assembly is blocked by microtubules, it will not be easily fixed later on by depolymerizing microtubules. It may be possible to test this by forcing ELYS onto interphase chromatin, either with Cdk1-site phosphomimetic mutations or tethering to a DNA-binding domain (Zierhut et al., 2014). We predict that this should offset some of the nuclear morphology defects observed in ΔDppa2 extracts by reducing the importance of initial NPC assembly rates, promoting more homogeneous lamin import and increasing nuclear roundness.

We note that sperm incubated directly in interphase extracts only ever experience low Cdk1 activity, and assemble nuclei that are large in size but retain the original extended, crescent/corkscrew shape of hypercompacted sperm (Figure 3-7). Dynamic M phase asters may normally help by delivering membranes, an effect that is eliminated in interphase extracts. Alternatively, we speculate that ELYS-dependent seeding of NPCs on chromatin might be relatively homogeneous, since it is mediated by interaction with ubiquitous nucleosomes (unless of course dense microtubules are in the way), whereas Pom121 will selectively enrich on curved membranes, leading to a potentially more heterogeneous distribution. This second possibility predicts that activating the ELYS-dependent pathway of NPC assembly would also improve nuclear morphology in interphase extracts.

Nuclear assembly in interphase extracts is also insensitive to Dppa2 depletion, we suggest because the robust M phase microtubules that Dppa2 is normally required to control are not present. In addition, we know that dynamic microtubules enhance the aggregation of anaphase chromosomes into a single mass (Mora-Bermúdez et al., 2007); stabilizing microtubules with taxol disperses the chromosomes and leads to segregation defects. Chromsomes added directly to interphase extracts may also fail to aggregate as tightly, and subsequently swell into aspheric nuclei.

Spatial control of microtubule dynamics during fertilization

Dppa2 is bound to chromatin throughout the cell cycle, and this localization is essential for its role in nuclear assembly (Figure 3-11). Local control of microtubule dynamics is an important established paradigm for understanding metaphase spindle assembly, whereby enrichment and activation of RCC1 and the CPC restrict spindle microtubules to the vicinity of chromosomes and suppress ectopic spindle formation elsewhere in the cytoplasm. This is especially important in the context of the *Xenopus laevis* egg, which maintains a meiotic spindle of ~35 μm length in a cell of 1 mm diameter (Wühr et al., 2008). Dppa2 performs a similarly specific role by suppressing excessive microtubule growth around nascent nuclei, without perturbing global microtubule dynamics elsewhere in the cell. Even though the function of Dppa2 can be bypassed by a treatment as basic as nocodazole, this is not a viable biological solution since the loss of global aster microtubules would be catastrophic and prevent pronuclear capture and fusion.

The majority of experiments described in this thesis were performed in a manner mimicking fertilization and male pronuclear assembly. During this process, the sperm centrosome rapidly nucleates an aster that will eventually span the millimeter-scale

length of the fertilized embryo (Wühr et al., 2009). Astral microtubules are particularly dense during the first 15 minutes following release from metaphase (Figure 2-1), exactly the window in which nuclear assembly is most easily derailed. We note that microtubule suppression by Dppa2 is dispensable during the later stages of nuclear assembly (Figure 3-6A), even as the aster continues to increase in size. We can reconcile this because by this point the interphase aster is more stable and less dense, relying on nucleation remote from the centrosome to continue growing (Ishihara et al., 2014). This presents a lesser impediment to nuclei, which have also incorporated sufficient levels of lamin to buffer against physical stresses.

Nuclear formation following mitosis

We do not exclude a role for Dppa2 in the early mitotic divisions of the *Xenopus* embryo, where remnants of spindle microtubules could also interfere with nuclear assembly. We performed an experiment in which we assembled metaphase spindles in egg extracts, and then inhibited Dppa2 by adding function-blocking antibodies against Dppa2, together with calcium to trigger anaphase (Figure 2-7C). To our surprise this elicited a stronger nuclear assembly defect than we had observed with pronuclear assembly experiments in immunodepleted extracts. However, we are wary of overinterpreting this result since Dppa2 is a DNA-binding protein, and so high-affinity antibodies against Dppa2 could coat chromosomes and inhibit chromosome condensation, even though antibodies against the chromokinesin Xkid did not have this effect (Figure 2-7C).

Human tissue culture studies have shown that taxol treatment can interfere with chromosome dynamics and delay nuclear envelope closure (Mora-Bermúdez et al., 2007; Lu et al., 2011), but none have reported significant nuclear morphology defects. Although

the *Xenopus* meiotic spindle is small compared to the size of the egg, it is still large relative to spindles in many other cells and moreover dense with non-kinetochore microtubules; for comparison, spindles in HeLa cells measure ~15 μm in length (Cai et al., 2009). We consider that if spindle remnants can interfere with nuclear assembly, they are more likely to do so in those cells that have larger spindles or more dense spindle fibers. In addition, one advantage of the sperm pronuclear assembly assay that we favor is the dramatic shape conversion from an initial crescent shape into a decondensed sphere (Figure 2-2). Assembly of interphase nuclei from anaphase chromosomes does not involve such a large shape change, making phenotypes harder to measure. Nonetheless, subtle defects in nuclear assembly may accumulate over time, potentially impacting nuclear organization or functions such as mechanotransduction.

Function of Dppa2 in embryonic development

The first cell cycle of the fertilized *Xenopus* embryo, which is the closest in vivo regime to egg extracts, is relatively slow, lasting around 30 min from prophase onset to cytokinesis and 100 min in total (Wühr et al., 2010). However, subsequent divisions up to the MBT are extremely rapid, compressing a complete round of DNA replication and nuclear division into 30 min. These rapid mitoses are poorly approximated by egg extract experiments as performed according to Figure 2-7C. Dppa2 is expressed in *Xenopus* embryos well beyond the MBT (Siegel et al., 2009; Woo, 2010), and morpholino-mediated knockdown of Dppa2 disrupts embryogenesis at a fairly late stage (Siegel et al., 2009). Since morpholinos only inhibit de novo protein synthesis and would not take effect until the maternal pool of Dppa2 is depleted by several cleavage cycles, this suggests that Dppa2 is required beyond pronuclear formation in the very first cell cycle.

It is tempting to speculate whether Dppa2 contributes to the rapid cell divisions that take place in pre-MBT embryos. In particular, *Xenopus* embryos utilize karyomeres to accelerate nuclear assembly, where segregating chromosomes assemble functional nuclear envelopes before anaphase is complete (Richards, 1917; Lemaitre et al., 1998). Dppa2 coats chromosomes along their length, and could facilitate karyomere formation by destabilizing spindle microtubules that contact chromosomes.

Egg extracts cannot recapitulate karyomere formation, and the exact requirements for Dppa2 in fertilization and mitosis can only be determined by in vivo experiments. Dppa2 function could be blocked in embryos by microinjection of anti-Dppa2 antibodies at different developmental stages, followed by immunostaining of microtubules and nuclear envelopes (Becker and Gard, 2006). Live imaging is also possible by co-injecting mRNA encoding fluorescent protein-tagged tubulin and nuclear envelope proteins, though limited to superficial cell layers due to the opacity of *Xenopus* embryos (Woolner et al., 2009). Another workaround is to make extracts of synchronized embryos at different stages. Embryo extracts containing G2/prophase nuclei can be progressed to metaphase by adding CSF-arrested egg extract, and then released into interphase with calcium to monitor karyomere formation (Lemaitre et al., 1998).

5.3. Implications for disease

We have shown that altered microtubule dynamics can cause defects in nuclear assembly, and hypothesize that mutation of microtubule regulators or motor proteins could have similar effects during pathogenesis. Nuclei in ΔDppa2 extracts fail DNA replication, but even less severe perturbations to nuclear assembly could be deleterious. Proper pronuclear size and aster function are essential during fertilization, since small pronuclei

risk failing to complete pronuclear fusion (Meyerzon et al., 2009). A study of patients undergoing in vitro fertilization found multinucleated cells in the embryos of 44% of patients, contributing significantly to rates of pregnancy failure (Balakier and Cadesky, 1997). Multinucleation and the similar phenomenon of micronuclei formation originate from mitotic segregation errors giving rise to lagging chromosomes, where we speculate misregulated microtubule dynamics may contribute to subsequent pathology.

Lagging chromosomes are at risk because they dwell near the spindle midzone, which contains dense microtubules that could physically obstruct nuclear envelope assembly, and is also a region of high CPC activity (Fuller et al., 2008). Lagging chromosomes show a delay in nuclear envelope formation relative to other chromosomes in the same cell that have completed segregation (Afonso et al., 2014), leading eventually to micronuclei formation. This delay has been attributed solely to high CPC activity at the midzone, since it is rescued by Aurora B inhibition (Figure 5-2). However, Aurora B inhibition not only reduces CPC activity but also destabilizes midzone microtubules, and so there could exist a second component of the nuclear assembly delay that depends on microtubules (for example physical exclusion of membrane recruitment) but is CPC-independent. To distinguish between these two components, Aurora B inhibition could be combined with acute taxol treatment to ask whether ectopic microtubules can impede nuclear assembly, independently of the CPC, in cells that suffer chromosome segregation errors.

Lagging chromosomes that fail nuclear envelope assembly are a source of micronuclei, which are characterized by weakened or incomplete nuclear envelopes, replication defects, and proneness to rupture later in the cell cycle (Hatch et al., 2013).

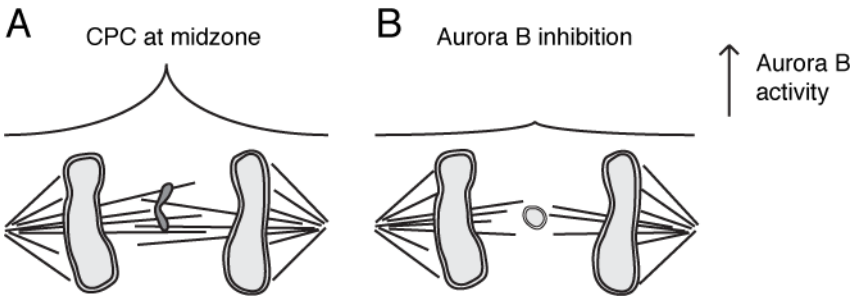

Figure 5-2. Lagging chromosomes undergo delayed nuclear assembly

(A) In untreated cells, lagging chromosomes show delayed chromosome decondensation and nuclear assembly due to the nearby presence of dense midzone microtubules and high CPC activity.

(B) In the presence of Aurora B inhibitors, CPC activity is low but midzone microtubules will also be destabilized, allowing lagging chromosomes to proceed to nuclear formation at the same time as segregated chromosomes.

Rupture during S phase is particularly damaging and could lead to massive DNA damage to the micronuclear chromosome (Crasta et al., 2012), termed ‘chromothripsis, thought to be a source of genomic instability in many cancers (Stephens et al., 2011).

Finally we consider an additional possible consequence of micronuclear rupture. Mammalian cells contain an innate immunity pathway that senses foreign DNA in the cytoplasm, triggering a type I interferon response to defend against viral infection (Cai et al., 2014). DNA sensing is mediated by the second messenger cyclic GMP-AMP (cGAMP) and its synthetase cGAS, which activate the ER transmembrane protein STING and subsequently NF-κB signaling. Host DNA normally escapes detection because it is sequestered inside the nucleus. However, in certain congenital disorders DNA accumulates in the cytoplasm, triggering the STING response and leading to autoimmune disease (Stetson et al., 2008; Gall et al., 2012). We hypothesize that DNA inside ruptured micronuclei could trigger a similar response. To test this, ruptured micronuclei can be reliably generated in cancer cells (Hatch et al., 2013), and then monitored for activation of STING. This may represent an unappreciated pathway to autoimmune disease, as well as contributing to the pro-inflammatory environment of cancer (Grivennikov et al., 2010).

5.4. Conservation of Dppa2

The mammalian orthologs of *Xenopus* Dppa2 share sequence similarity in their SAP and DCR domains (Figure 1-4; Siegel et al., 2009), but are truncated at the C terminus and do not suppress microtubule polymerization (Figure 4-7). Human Dppa2 and Dppa4 are found in the same orientation in the genome, spaced 20 kb apart on chromosome 3q13. They share many putative upstream binding sites for pluripotency-related transcription factors such as POU and SOX domain proteins (Maldonado-Saldivia et al., 2007),

suggesting that their expression may be co-regulated. There is also evidence of a splice variant of Dppa4 that lacks the SAP domain, though expressed at lower levels than the full-length isoform (Maldonado-Saldivia et al., 2007). Dppa4 lacking the SAP domain has been generated experimentally and was found to bind histones via the DCR motif (Masaki et al., 2010), although this variant associates with chromatin less stably than full length Dppa4 containing both the SAP and DCR domains.

We have not identified any Dppa2 orthologs in invertebrate animals, fish or amphibians other than *Xenopus*. However, the genomes of two reptiles, the Burmese python *Python bivittatus* and the lizard *Anolis carolinensis*, contain predicted proteins that share 35% sequence identity with *Xenopus* Dppa2, including the C terminus (Figure 5-3). With only two sequences from each of amphibians and reptiles, we cannot be certain that the scheme shown in Figure 5-3 is correct. However, if it were, the alignment would suggest that *Xenopus* Dppa2 containing the extended C terminus is the ancestral state, and that the C-terminal domain was later lost in the amniote lineage after mammals diverged from reptiles.

We do not know whether the C terminal domains of these putative reptile orthologs can suppress microtubule assembly. If they can, we should be able to infer some of the key residues required for this activity among the 35% that are conserved between *Xenopus* and reptile Dppa2, which could then guide homology searches for related proteins. However, mammals were clearly not under selective pressure to maintain the C terminus and have since adapted to its absence. In an earlier section we discussed hypotheses for how suppression of microtubules by *Xenopus* Dppa2 may

A

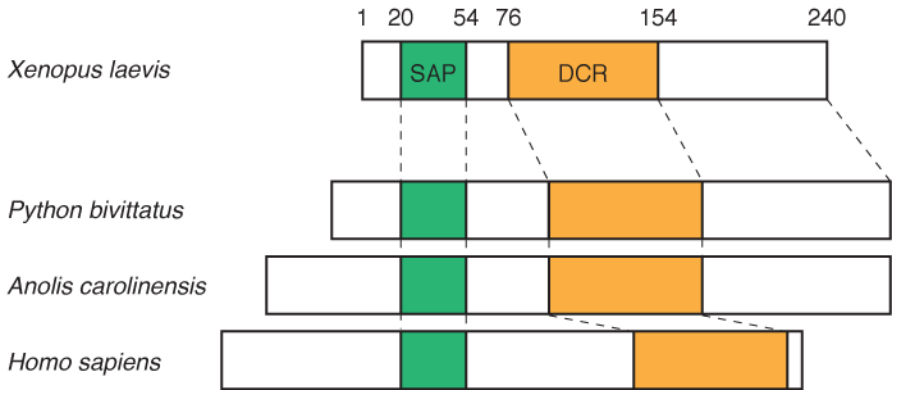

B

```
X. laevis           150 ECRLQQR------SVFQD-NY-----PPMGQMRKS-VSTTRTRKKSGR-------F
X. tropicalis       149 ECRLQQR------SAFQDKNY-----PPSGQMRKSTISASRSRKKSGR-------F
P. bivittatus       193 KCTLCQQIQGKGSTAYLSQNFFKNLSPLVKSTSSSSLLAAGGSKEKRRTVEIKKLY
A. carolinensis     234 KHPMNQQIQGKGKRVSLPKTALKNVIPRQDYTAQPSLDATNTSRDKRRTIEIRKLY
                            *                   *                   *

X. laevis           190 QPQEDPEYARRVDELLDQLATGQVDSQKILKPSRPAVLHSPLPKPESSPIAINQ
X. tropicalis       191 QPQEDPEYARRVDELLGQLATGQVDSQKVLKPSRPAVMHSPLAKPESSPIAIDQ
P. bivittatus       248 QPQEDQAYAQRVDGILSQMARGELGMDRALRPLQPLVVHSPAPYGR--------
A. carolinensis     288 QPQEDEAYAQRVDGLLSLMARGELGMDLALRPVQPLVVHSPAPFEK--------
                        *****  ** ***  *   * *       * *  * * ***
```

Figure 5-3. Putative orthologs of *Xenopus* Dppa2 in reptiles

(A) Alignment of *X. laevis* Dppa2 drawn to scale against orthologs in *P. bivittatus* (XP_007425058.1) and *A. carolinensis* (XP_008120055.1). *H. sapiens* Dppa2 is also included for comparison purposes.

(B) Alignment of C-terminal domains of Dppa2 in amphibians and reptiles. Asterisks indicate identical residues.

facilitate rapid cell division in the pre-MBT embryo, and it is possible that this function became unnecessary in lineages when cell cycles became longer.

Function of mammalian Dppa2 paralogs

Nonetheless, mammalian Dppa2 and Dppa4 have essential functions, since knocking out either gene in mice results in lethality before or soon after birth (Madan et al., 2009; Nakamura et al., 2011). Transcriptome analysis of Dppa2-null mouse embryos found 106 genes whose expression was altered at least two-fold, and increases in DNA methylation and histone H3 lysine 9 dimethylation at a number of gene promoters (Nakamura et al., 2011). In this study, the most affected genes were Nkx2-5, a homeobox transcription factor required for cardiac and muscle development (Bodmer, 1993; Lints et al., 1993) and the synaptonemal complex protein Syce1 (Costa et al., 2005). The mechanism by which Dppa2 could regulate these apparently unrelated genes is still unclear. A yeast two-hybrid screen using human Dppa2 as bait identified 18 potential interacting proteins, including the putative histone methyltransferase SETD5 (Rual et al., 2005; Grozeva et al., 2014; Kuechler et al., 2014), but to our knowledge has not been followed up.

Overexpression of Dppa2 in human cancers

While Dppa2 is normally silenced in adult somatic tissues, it becomes reactivated in certain cancers and is oncogenic when transduced into tissue culture cells (John et al., 2008; Tung et al., 2013). However, we are cautious of extrapolating our ideas of how Dppa2 functions during embryogenesis to its activities when overexpressed outside its native context. Overexpression of human Dppa2 and Dppa4 in untransformed 3T3 cells results in 2- to 4-fold upregulation of a number of cell-cycle-related genes, including

cyclin B1, cyclin G1, E2F1 and Mdm2-binding protein (Tung et al., 2013). This effect requires both the SAP and DCR domains, and may be related to the proposed epigenetic functions of mouse Dppa2 (Nakamura et al., 2011).

Since Dppa2 overexpression occurs most frequently in lung carcinoma, future overexpression experiments should be performed in cultured pulmonary epithelial cells (Forbes, 2002). We would be interested to know whether Dppa2 drives expression of the same target genes in lung epithelia as it does in 3T3 fibroblasts, but also any changes in epigenetic status, heterochromatin distribution or nuclear morphology, which are hallmarks of cancer (Jevtić et al., 2014).

We have already discussed possible roles for Dppa2-dependent control of microtubule dynamics in fertilization or rapid mitosis prior to the MBT. However, *Xenopus* Dppa2 appears also to share at least some of the microtubule-independent activities of its mammalian orthologs. Morpholino-mediated knockdown of Dppa2 causes developmental defects in *Xenopus* embryos, but is partially rescued by co-expression of mouse Dppa2 (Siegel et al., 2009). Better understanding of mammalian Dppa2 and Dppa4 function will therefore also yield insights into *Xenopus* embryogenesis.

5.5. *Xenopus* Dppa2 is a novel microtubule catastrophe factor

Xenopus Dppa2 is a chromatin-bound microtubule-destabilizing protein, placing it in opposition to the microtubule-stabilizing pathways of RanGTP and the CPC. We do not yet understand the mechanism by which Dppa2 promotes microtubule catastrophe, and discuss here preliminary ideas of how Dppa2 might interact with microtubules, while highlighting priority experiments to shed light on its mechanism.

The Dppa2 C terminus may be a protein-protein interaction hub

The C terminus of Dppa2 required for suppressing microtubules does not share sequence homology with any known microtubule regulators, and sequence-based structure modeling programs were unable to predict any folds with high confidence. It has a relatively high degree of disorder, though comparable to the SAP domain for which solution structures have been determined (Figure 3-9A; Suzuki, 2009). The C terminus has an isoelectric point of ~10 and is fairly hydrophilic with a high likelihood of solvent exposure. These are common features of epitopes that mediate protein-protein interactions. Moreover, the region is enriched in proline residues, 5 out of 6 of which are conserved in the reptile homologs (Figure 5-3B). Proline residues are conformationally rigid, and polyproline sequences tend to adopt a helical structure that presents a hydrophobic surface within a mostly hydrophilic domain (Kay et al., 2000). This favors hydrophobic interactions and thus also promotes protein-protein docking. The implications of these features for stimulating microtubule catastrophe are unclear, although it suggests a possible binding surface for microtubules. Our preliminary proteomics efforts to find binding partners to Dppa2 were unsuccessful and failed to pull down any specific proteins (data not shown). However, we consider that Dppa2 may only bind specific structures for which we had not enriched (see below, 'Interaction between Dppa2 and microtubules'). In addition, binding partners of Dppa2 may be transient, in which case pulldown experiments are worth repeating using low concentrations of crosslinking reagent to stabilize weak interactions (Subbotin and Chait, 2014).

Another common feature of these exposed and relatively disordered regions is that they are frequently post-translationally modified. In addition to PIASy-dependent

SUMOylation of lysine 230, Eileen Woo identified multiple phosphorylation sites in Dppa2 at serines 226 and 234 that match the Cdk consensus (Woo, 2010). Mutation of these sites, or an additional Aurora B consensus site at serine 183, did not affect SUMOylation of Dppa2. These modifications may serve to enhance protein-protein interactions, and highlight a further challenge for proteomic screens seeking interacting partners, since phosphorylation is easily lost during capture and washing steps. Possible solutions include using glutamate and aspartate substitutions or chemical installation of stable phosphoresidue analogs. SUMOylation-dependent interactions are more difficult since Dppa2 is only SUMOylated upon binding to DNA (Woo, 2010), but work from other groups has successfully identified SUMO-dependent protein-protein interactions by using linear fusions of the SUMO protein tagged onto the C terminus of proteins of interest (Huang et al., 2003), or alternatively tethering Dppa2 to the SUMO E2 conjugating enzyme Ubc9 (Niedenthal, 2009). However, we note that recombinant Dppa2 which is unmodified was active in suppressing microtubule assembly in vitro, as was the SUMO-deficient K230R mutant (Figure 3-8), indicating that neither modification is essential for this activity, though they may modulate it in vivo or play some additional unidentified function.

Interaction between Dppa2 and microtubules

Despite the ability of Dppa2 to suppress microtubule assembly in *Xenopus* egg extracts and in vitro, we found no evidence of any interaction between Dppa2 and microtubules or soluble tubulin (Figure 4-1). The observation that Dppa2 promotes microtubule catastrophe without reducing microtubule growth velocity suggests that it acts on microtubule polymers rather than soluble tubulin, and possibly at or near the GTP

cap. Catastrophe is thought to result from conformational changes in the tubulin protofilament following GTP hydrolysis, and it is possible that Dppa2 only binds short-lived intermediates or transition states in this process. One approach would be two-color imaging of Dppa2 together with the tips of dynamic microtubules. Although our preliminary attempts to visualize Dppa2 fused to a single GFP on microtubules were unsuccessful (data not shown), it may be necessary to increase fluorescence signal by fusing multiple tandem copies of GFP, or alternatively using photostable dyes such as the Alexa Fluor family.

An alternative would be to look for Dppa2 binding to microtubule ends by electron microscopy. This may be difficult since microtubule ends are highly heterogeneous, which hampers the class averaging process used to obtain high precision localization information. However, tubulin oligomers can be stabilized in a ring conformation that closely mimics the curvature of microtubule ends with the drug dolastatin. Dolastatin rings were used as a homogeneous platform for binding of MCAK in electron microscopy studies (Moores and Milligan, 2008), and may be useful to enrich for Dppa2 if it has similar binding modes.

Dppa2 as a putative tubulin GAP

Dppa2 cannot destabilize GMPCPP-stabilized microtubule seeds, which distinguishes its mechanism of action from those of microtubule-severing enzymes (Hartman et al., 1998) and KinI depolymerases (Desai et al., 1999). We hypothesize that Dppa2 may stimulate the GTPase activity of the microtubule polymer, accelerating loss of the GTP cap and promoting catastrophe. To test this model, GTP hydrolysis can be monitored by polymerizing microtubules in the presence of Dppa2 and radiolabeled GTP. If Dppa2 has

a sufficiently large effect on the GTPase activity of tubulin, this should result in increased conversion of GTP to GDP despite inhibition of tubulin polymerization. However, even in the absence of Dppa2, microtubules undergoing dynamic instability will continually consume GTP as microtubules grow, and so if Dppa2 has only a modest GAP activity it may be difficult to distinguish from this background.

We also note that while Dppa2 was far more effective at suppressing growth of microtubules in the presence of GTP than GMPCPP, it still produced a statistically significant decrease in the length of microtubules assembled in the presence of GMPCPP (Figure 4-5). GMPCPP hydrolysis is normally very slow with a half-life of many hours (Caplow et al., 1994), and if the mechanism of Dppa2 action is truly as a GAP, it may have sufficiently accelerated the hydrolysis of GMPCPP to produce this effect.

5.6. Concluding remarks

In our analysis of microtubule dynamics in vitro, we measured microtubule growth and catastrophe but neglected shrinkage and rescue. Shrinkage velocities can be captured by imaging with better time resolution, but rescue frequencies rarely occur in vitro. An alternative approach would be to compare rescue frequencies in control and ΔDppa2 *Xenopus* egg extracts, using axonemes or centrosomes to nucleate microtubules; GMPCPP seeds cannot be used in extracts as they are quickly destroyed by high severing activity.

The work contained in this thesis describes a new function for *Xenopus* Dppa2 in regulating microtubule catastrophe in the vicinity of chromosomes. Though this activity is not shared by the mammalian orthologs of Dppa2, it illustrates an evolutionary innovation that allows regulation of local microtubule dynamics, without perturbing

reactions that may be occurring in different locations or over alternative length scales. The activity of Dppa2 was critical to maintaining balanced microtubule dynamics during nuclear formation, since nuclear assembly relies on microtubule-dependent delivery of membranes but can also be distorted by excess microtubules. If this process is compromised, accumulated nuclear defects may accelerate the progression of cancer, autoimmunity and aging.

The catastrophe-promoting activity of Dppa2 resides in its C terminus. Here our knowledge is hampered by the lack of obvious orthologs to the C-terminal domain, although this may improve as more non-mammalian vertebrate genomes are sequenced. GAPs for tubulin have been previously described (Roychowdhury et al., 1999), but Dppa2 adds an extra dimension of strict localization requirement. A key question for the future will be to reconcile the microtubule-regulatory activity of *Xenopus* (and possibly reptile) Dppa2 with the proposed epigenetic functions of their mammalian orthologs, which need not necessarily be mutually exclusive.

Chapter 6. Materials and methods

Xenopus laevis *egg extracts*

Female *X. laevis* between 2.3 and 2.5 years of age were purchased from Nasco (LM00535M). Frogs were primed by injection of 50-75 units pregnant mare serum gonadotropin (EMD Millipore 367222) into the dorsal lymph sac using a 27-gauge hypodermic needle. After at least 48 h but within 3 weeks, ovulation was induced with 150-500 units human chorionic gonadotropin (Sigma CG10). Frogs were rested for 3 months between ovulation cycles. Procedures were approved by The Rockefeller University Institutional Animal Care and Use Committee.

Eggs were collected in Marc's Modified Ringer's solution at 16 °C over 16 h in the dark. CSF-arrested metaphase egg extracts were prepared according to Murray (1991).

Nuclear and aster assembly

A typical reaction comprised 20 µl CSF extract, demembranated sperm (500/µl) and $CaCl_2$ (0.4 mM) incubated at 20 °C. Extract supplements included with DAPI (0.5 µg/ml), Hoechst 33342 (0.5 µg/ml), YOYO-1 (Invitrogen N7565; 0.1 µM); $DiOC_6$ (1 µg/ml), $DiOC_{18}$ (1 µg/ml), CM-DiI (Invitrogen V-22888; 1 µM), 1 µM GST-GFP-NLS (gift of Cristina Ghenoiu), bovine tubulin labeled with X-rhodamine succinimidyl ester (Invitrogen C-1309; 0.2 µM), or antibodies labeled with Alexa Fluor 568 succinimidyl ester (Invitrogen A20184; 1-10 µg/ml).

Nuclei and asters were fixed by squashing 1 µl extract with 3 µl fix (PBS, 50% (v/v) glycerol, 10% (w/v) formaldehyde, 1 µg/ml Hoechst 33342) under an 18 × 18 mm

coverslip. Live imaging was performed by squashing 4 µl extract under a coverslip and sealing with warm Valap (equal parts mixture of petroleum jelly, lanolin and paraffin).

Nocodazole (Sigma M1404) was used at 0.4 to 16 µM, taxol (Sigma T7402) at 10 µM and colcemid (Fisher A430033M001) at 13 µM. GST-Op18^{AAA} (gift of Jessica Rosenberg) (Budde et al., 2001) was used at 4 µM.

Spindle assembly

Spindles were assembled by cycling through interphase to metaphase. Sperm (1000/µl) and $CaCl_2$ (0.4 mM) were added to metaphase extracts and incubated at 20 °C. S phase is completed after 1 h 20 min, and extracts were driven back into metaphase by addition of 3 volumes of CSF extract. Spindles were visualized after 60 min.

Recombinant proteins

Purified Dppa2 protein had poor solubility and was prone to aggregation. We favored expressing Dppa2 as a fusion protein with N-terminal MBP and C-terminal polyhistidine tags. Rosetta 2 cells (EMD Millipore 71403) were grown at 37 °C to OD_{600} of 1.0 in 1 l rich medium (1% tryptone, 0.5% yeast extract, 0.5% NaCl, 0.1% NH_4Cl, 0.6% Na_2HPO_4, 0.3% KH_2PO_4, 1 mM $MgCl_2$, 0.4% glycerol, 0.5% glucose). Expression was induced with 0.1 mM IPTG and incubation at 18 °C for 16 h. Cells were harvested by centrifugation and stored at -20 °C.

Cell pellets were resuspended in 50 ml amylose column buffer (20 mM HEPES [pH 8.0], 0.2 M KCl, 10 mM 2-mercaptoethanol), supplemented with 0.2 mg/ml lysozyme and 20 µg/ml DNase I. Cells were lysed first by dounce homogenizer and then sonication. Lysates were clarified at 45,000 rpm (*k*-factor 133) in a type 45 Ti rotor (Beckman 337922 rotor, 355618 bottles), 4 °C, 45 min. Proteins were captured by

incubation with 2 ml amylose resin (NEB E8021), 4 °C, 1 h with rotation. Resin was washed with 100 ml amylose column buffer, then eluted with 20 ml column buffer supplemented with 10 mM maltose.

Polyhistidine-tagged proteins were captured from maltose eluates by incubation with 1 ml Ni-NTA (Qiagen 30230), 4 °C, 30 min with rotation. Resin was washed with 50 ml Ni^{2+} column buffer (20 mM HEPES [pH 8.0], 0.3 M KCl, 30 mM imidazole, 10 mM 2-mercaptoethanol), then eluted with polyhistidine elution buffer (20 mM HEPES [pH 8.0], 50 mM KCl, 250 mM imidazole, 10 mM 2-mercaptoethanol). Eluates were applied directly to cation exchange columns at pH > 7, or anion exchange at any pH. For all other ion exchange protocols, imidazole was first removed by dialysis. Purified proteins were stored at -80 °C in 20 mM HEPES [pH 8], 150 mM KCl, 1 mM DTT.

Anti-Dppa2 antibodies

Affinity and solubility tags were cleaved off Dppa2 prior to immunization of rabbits. For antibody purification, GST-Dppa2 was expressed in *E. coli*. Cells from 2 l culture were lysed in PBS and captured by incubation with glutathione sepharose resin (GE Healthcare 17-0756-05), 4 °C, 1 h with rotation. Resin was washed with 100 ml PBS, then crosslinked by incubation with 30 mM dimethyl pimelimidate (Fisher PI-21667), 45 min at room temperature with rotation in the dark. Crosslinking was quenched with 2 incubations in 0.1 M ethanolamine [pH 8.2], 10 min each. Resin was then washed extensively with glutathione elution buffer (20 mM Tris [pH 8], 150 mM NaCl, 10 mM reduced glutathione).

Polyclonal antibodies from sera were captured on crosslinked GST-Dppa2, washed with 100 ml antibody wash buffer (20 mM phosphate [pH 7.4], 0.5 M NaCl,

0.1% Tween-20) and eluted with 0.2 M glycine [pH 2.3]. One-milliliter fractions were collected into tubes containing 35 µl of 2 M Tris base and mixed immediately. Antibodies were dialyzed into PBS + 50% glycerol for storage at -20 °C.

Immunodepletion

CPC depletion requires crosslinking of antibodies to beads (Kelly et al., 2007); Dppa2 depletion does not.

To deplete Dppa2 from 100 µl extract, 100 µl magnetic protein A beads (Invitrogen 10008D) were washed with 5 × 200 µl antibody wash buffer (100 mM HEPES [pH 8.0], 150 mM KCl), then resuspended in 100 µl wash buffer supplemented with 10 µg anti-Dppa2 antibodies or rabbit IgG for mock depletion control. Beads were incubated with rotation at room temperature for 1 h, then washed 3 times and moved to a fresh tube. Beads were washed 2 more times in sperm dilution buffer (5 mM HEPES [pH 8], 100 mM KCl, 1 mM $MgCl_2$, 50 mM sucrose), and divided into 2 portions. Extracts were supplemented with 100 µg/ml cycloheximide and applied to one portion of beads and incubated on ice for 1 h. Beads were recovered and applied to the second portion. After the second round of depletion, extracts were applied to magnets twice to remove beads.

To deplete the CPC from 100 µl extract, 200 µl beads were coupled to 17 µg anti-INCENP antibodies. Antibodies were crosslinked by resuspending beads in 0.5 ml dimethyl pimelimidate (30 mM in antibody wash buffer) and incubating for 45 min at room temperature in the dark. Crosslinking reactions were quenched with 2 × 10 min washes in Tris-buffered saline. Beads were then washed, and divided into two portions for two rounds of depletion.

Immunoprecipitation

Beads were prepared identically to those used for immunodepletion but crosslinking was essential. For each reaction, 5 µg antibodies were coupled to 50 µl beads, and incubated with 100 µl extract at 4 °C for 1 h. Beads were washed with 5 × 200 µl IP wash buffer (20 mM HEPES [pH 8.0], 250 mM KCl, 0.1% Triton X-100) and eluted with 20 µl SDS sample buffer or mass spec elution buffer (0.5 N NH_4OH, 0.5 mM EDTA).

DMSO-induced microtubule assembly in egg extracts

Five per-cent DMSO was added to 20 µl metaphase egg extracts, and incubated at 20 °C for 30 min. Extract was diluted in 0.4 ml BRB80 (80 mM PIPES [pH 6.9], 1 mM $MgCl_2$, 1 mM EGTA) + 30 % glycerol + 1 % Triton X-100, and layered over 0.8 ml BRB80 + 40% glycerol in microcentrifuge tubes. Microtubules were pelleted by centrifugation at 16,000 g for 15 min at room temperature. The supernatant was removed and the cushion interface washed with 2 × 0.4 ml BRB80. The cushion was then removed and the pellet resuspended in 40 µl SDS sample buffer.

DMSO-induced assembly of purified tubulin

For in vitro microtubule assembly, reactions containing 20 µM bovine tubulin in 10 µl volume of BRB80 + 1 mM DTT + 1 mM GTP were assembled on ice. Five per-cent DMSO was then added and the mixture warmed to 37 °C for 30 min. The mixture was layered over 0.5 ml warm BRB80 + 40 % glycerol and pelleted at 90,000 rpm (14.5 *k*-factor) in a TLA120.1 rotor (Beckman) for 5 min at 37 °C. The supernatant was removed and the cushion interface washed with 2 × 0.2 ml BRB80. The cushion was removed and the pellet resuspended in 30 µl SDS sample buffer.

Western blots

Immunoblots were blocked with 4 % nonfat dry milk in PBS for 1 h at room temperature. Primary antibodies were diluted in PBS + 2% BSA + 0.1% Tween 20. IRDye 800CW and 680RD secondary antibodies were used at 50 ng/ml.

Immunofluorescence microscopy

Ten microliter extract samples were fixed in 2 % formaldehyde for 5 min, then spun down onto glass coverslips. Primary antibodies were diluted in PBS + 2% BSA + 0.1% Triton X-100. Alexa Fluor 488 and Cy3-conjugated secondary antibodies (Jackson ImmunoResearch) were used at 1.5 µg/ml, DNA was stained with 1 µg/ml Hoechst 33342.

Quantification of microscope images

Nuclei and spindles were segmented from images by global thresholding in ImageJ (NIH). Nuclear cross-sectional area and roundness were measured using the 'Analyze Particles' command. Spindle length was defined as the Feret diameter (longest distance between any two points on the perimeter).

Radioactive replication assay

Nuclei were assembled in extracts supplemented with 1 kBq/µl [α-^{33}P]dCTP (PerkinElmer). At each time point, 15 µl extract samples were taken and added to 200 µl stop buffer (20 mM Tris [pH 8], 20 mM EDTA, 0.5 % SDS) containing 50 µg/ml RNase A and incubated at 37 °C for 15 min. A further 200 µl stop buffer containing 1 mg/ml proteinase K was then added, and the reaction incubated at 37 °C for 1 h. Samples were extracted twice with 400 µl phenol-chloroform and once with 400 µl chloroform. DNA was precipitated by addition of 40 µl 3 M sodium acetate and 1 ml ethanol and incubation

at 4 °C for 15 min, then pelleted by centrifugation at 16,000 g for 30 min at 4 °C. DNA pellets were resuspended in 15 µl TE buffer (10 mM Tris [pH 8], 1 mM EDTA) containing 50 µg/ml RNase A. Ten microliters of each sample was loaded on an agarose gel, then dried and exposed to a PhosphorImager screen (Fujifilm).

Fluorescent replication assay

Nuclei were assembled in extracts supplemented with 1 µM FITC-dUTP (GE Healthcare), and spun down for immunofluorescence. Replication was inhibited by addition of 8 µM recombinant non-degradable geminin (gift of Christian Zierhut (McGarry and Kirschner, 1998) or 40 µM aphidicolin (Fisher BP615).

Histone H1 kinase assay

One microliter samples of metaphase and interphase *Xenopus* egg extracts were snap-frozen in liquid nitrogen and stored at -80 °C. Samples were thawed with 9 µl kinase buffer (15 mM $MgCl_2$, 20 mM EGTA, 80 mM β-glycerophosphate, 0.1 % Igepal CA-630, 1 mM DTT, 50 µM ATP, 10 µg/ml leupeptin, 10 µg/ml pepstatin, 10 µg/ml chymostatin, 125 µg/ml histone H1, 60 µCi/ml [γ-^{32}P]ATP). Reaction was incubated at 30 °C for 10 min and stopped by addition of 30 µl SDS sample buffer. 10 µl was analyzed on a 15 % polyacrylamide gel, dried and exposed to a PhosphorImager screen.

Stock 5 × reaction buffer (75 mM $MgCl_2$, 100 mM EGTA, 400 mM β-glycerophosphate, 0.5 % Igepal CA-630) may be stored at 4 °C for 1 month, other components should be added fresh.

Sperm remodeling

Capped mRNA encoding GFP-H2B (gift of Christopher Jenness) was synthesized using the mMessage mMachine kit (Invitrogen AM1340). CSF-arrested extracts were

supplemented with 150 µg/ml mRNA and cycled through interphase to metaphase for translation. Demembranated sperm were incubated in these extracts for 30 min and visualized by immunofluorescence using anti-GFP antibodies. Biotinylated chromosomes were purified according to Funabiki and Murray (2000).

GMPCPP-stabilized microtubule seeds

Alexa Fluor 488-labeled, biotinylated (Cytoskeleton T333P) and recycled tubulins were mixed to 20 µM total tubulin concentration in 1× BRB80 + 1 mM DTT + 1 mM GMPCPP (Jena Bioscience, NU-405). Final label ratios were 0.25× fluorescent and 0.1× biotinylated. The seed mix was incubated on ice for 10 min, then clarified by ultracentrifugation (Beckman TLA120.1 rotor, 90,000 rpm, 2 °C, 5 min). The supernatant was stored as 3 µl aliquots at -80 °C. To assemble seeds, one aliquot was warmed to 37 °C for 15 min.

Passivated coverglass

18 × 18 mm coverslips were passivated as previously described (Lamichhane et al., 2010). Coverslips were cleaned by sonication in successive 5 min cycles of 2% Micro-90 detergent (VWR 89210-138), deionized water, 0.1 M KOH and water. Coverslips were rinsed in ethanol, then dried by wicking with Kimwipes and compressed air.

Clean coverslips were immersed in a solution of 2% 3-aminopropyltriethoxysilane (VWR TCA0439), 5% acetic acid, 93% methanol for 5 min, then laid onto Kimwipes. Fresh 20% (w/v) solutions of PEG (Laysan Bio MPEG-SC-5000) and biotin PEG (Laysan Biotin-PEG-SC-5000) are made up in 0.1 M $NaHCO_3$, and combined in 75:1 ratio of PEG:biotin PEG. Two coverslips at a time were dried fully with compressed air, then sandwiched together around 6 µl of PEG mixture. Sandwiches

were incubated for 3 h in a humid chamber, then rinsed in water and stored under vacuum.

Microtubule dynamics assay

A flow cell was constructed using a clean slide, double-sided tape and a biotin-coated coverslip. The cell was incubated with 0.5 mg/ml streptavidin (Fisher 21122) for 5 min, then flushed with BRB80 + 1 mM DTT + 0.5 mg/ml casein. GMPCPP seeds were diluted 1/1000 in BRB80 and perfused into the flow cell. After 5 min, unbound seeds were washed out and replaced with polymerization mixture (1× BRB80, 12 μM tubulin, 25% Alexa 594-labeled, 1 mM GTP, 1 mM ATP, 0.5 mg/ml casein, 5% glycerol), supplemented with 10× oxygen scavenging mix (45 mg/ml glucose, 2 mg/ml glucose oxidase [Sigma G-2133], 0.35 mg/ml catalase [Sigma C-40], 0.5% 2-mercaptoethanol). The flow cell was sealed with Valap and placed on a microscope stage heated to 37 °C for 10 min to reach steady state before imaging. Lifetimes and lengths of microtubule extensions at catastrophe were measured from time-lapse microscopy traces. Growth velocity was defined as the sum of microtubule lengths divided by the sum of lifetimes, catastrophe frequency as the number of catastrophes divided by the sum of lifetimes.

Statistical analysis

Sample means were compared by two-tailed unpaired *t*-tests assuming unequal variances. For microtubule dynamics parameters, experimental data were resampled 1,000 times to obtain bootstrap confidence intervals for growth velocity and catastrophe frequency.

Table 6-1. Primary antibodies used for western blot and immunofluorescence

Immunogen	Source	Identifier	Host species	Stock (mg/ml)	WB dilution	IF dilution
Aurora B	Cocalico	RU1050	Rabbit	3.4	5 μg/ml	
Dasra A	Cocalico	RU982	Rabbit	7		6 μg/ml
Dppa2 peptide	Covance	RF1828	Rabbit			
Dppa2 peptide	Covance	RF1829	Rabbit			
Dppa2 peptide	Covance	RF1830	Rabbit			
Dppa2	Covance	RF1831	Rabbit			
Dppa2	Covance	RF1832	Rabbit	6.7	5 μg/ml	0.2 μg/ml
Dppa2	Covance	RF1833	Rabbit		5 μg/ml	
GFP	Roche	11814460001	Mouse	0.4	0.4 μg/ml	2 μg/ml
H3	Abcam	ab1791	Rabbit		1/1,000	
H3S10ph	H. Kimura	7G1G7	Mouse		0.5 μg/ml	1 μg/ml
H3T3ph	Millipore	07-424	Rabbit		1/10,000	
H4K20me2	H. Kimura	2E2	Mouse	4.6		1 μg/ml
INCENP	Covance	RF1718	Rabbit		5 μg/ml	1 μg/ml
Lamin B3	D. Shumaker		Rabbit			1/200
mAb414	Covance	MMS-120P	Mouse	1		0.2 μg/ml
MBP	NEB	E8032	Mouse		0.1 μg/ml	1 μg/ml
MCAK	R. Ohi		Rabbit		1 μg/ml	0.2 μg/ml
RCC1	R. Heald		Rabbit		1 μg/ml	
α-tubulin	Sigma	T9026	Mouse		1/20,000	1/1,000
γ-tubulin	Sigma	T3320	Rabbit		1/10,000	
Xkid	Cocalico		Rabbit		3 μg/ml	
Xorbit	R. Heald		Rabbit		1/6,000	

Table 6-2. Antibodies generated in this study

Target	Accession/clone	Immunogen	Supplier	ID	Concentration (mg/ml)	Date
Lamin B3[1]	NP_001081545	MBP-His-LB3(373-583)	Proteintech	S4118-1	0.3	10/6/13
Lamin B3[1]	NP_001081545	MBP-His-LB3(373-583)	Proteintech	S4118-2	0.18	10/28/13
LBR[2]	NP_001079301	MBP-His-LBR(1-211)	Proteintech	S4119-1	0.9	
LBR[2]	NP_001079301	MBP-His-LBR(1-211)	Proteintech	S4119-2	1.2	10/6/13
MBP[1]		MBP from pMAL vectors	Cocalico	RU1991	1.8	1/6/15
SP4[3]	NP_001081230	MBP-SP4 (denatured)	Cocalico	RU1990	–	1/6/15
SUN1[2]		CLYRFRAHGTPAQ	Covance	RF2080	6.0	8/9/12
SUN1[2]		CLYRFRAHGTPAQ	Covance	RF2081	0.9	8/9/12
SUN1[2]	IMAGE 6326555	MBP-His-SUN1(1-104)	Proteintech	S3956-1	0.3	10/28/13
SUN1[2]	IMAGE 6326555	MBP-His-SUN1(1-104)	Proteintech	S3956-2	0.15	
SUN2[2]	IMAGE 4173442	MBP-His-SUN2(1-152)	Proteintech	S4120-1	3.3	10/6/13
SUN2[2]	IMAGE 4173442	MBP-His-SUN2(1-152)	Proteintech	S4120-2	0.65	10/28/13

[1] Described in Appendix E.
[2] Not clear if these antibodies recognized the correct species in extract.
[3] SP4 (sperm-specific basic nuclear protein 4) was solubilized in 6 M guanidine HCl for immunization; we did not attempt to affinity-purify antibodies from serum.

Table 6-3. Plasmids used and generated in this study

Box	ID	Name	Description	Vector	mg/ml	Marker	Notes
1	1	pBS	Bluescript				For DNA beads
	2	H3-GST	H3(1-45)-GST				
	3	pJR14	H3(1-45) AA-GST				H3S10AS28A
	4	pJX10	H3(1-45)-F_c-His_{10}				
	5	pJX11	H3(1-45) AA-F_c-His_{10}				H3S10AS28A
	6	pJX12	H3(1-45)-ZZ-His_{10}				
	7	pJX13	H3(1-45) AA-F_c-His_{10}				H3S10AS28A
	8	Sororin			0.63		IMAGE 5511973
	9	Emi1			0.28		IMAGE 6323527
	10	Ligase IV		pCMV-SPORT6	0.55		IMAGE 6957895
	11	XLF/cernunnos		pCMV-SPORT6	0.52		IMAGE 6864803
	12	Spc24		pExpress-1	0.48		IMAGE 7765637
	13	Smarcd1			0.57		IMAGE 6642998
	14	Bromodomain containing 1					IMAGE 5515438
	15	Bromodomain containing 4					IMAGE 6638394
	16	SETD1B					IMAGE 6863688
	17	Sirtuin 3.2					IMAGE 6868458
	18	Cyclin D-type binding-protein 1		pCMV-SPORT6			IMAGE 7011193
	19	pBT25	GFP-INCENP	pCS2	2.3		
	20	pBT60			0.3		
	21	pJX21	GFP-INCENP(L33R)	pCS2	0.38		
	22	pJX22	GFP-INCENP(F21RL33R)	pCS2	2.8		

Box	ID	Name	Description	Vector	mg/ml	Marker	Notes
1	23	pJX23	GFP-INCENP(1-60)	pCS2	2.56		
	24	pJX24	GFP-INCENP(1-60; F21RL33R)	pCS2	2.76		
	25	pJX27	GFP-INCENP(1-242)	pCS2	2.37		
	26	pJX28	GFP-INCENP(1-242; F21RL33R)	pCS2	1.33		
	27	pJX29	GFP-INCENP(1-400)	pCS2	3.29		
	28	pJX30	GFP-INCENP(1-400; F21RL33R)	pCS2	3.14		
	29	pJX31	GFP-INCENP(1-491)	pCS2	2.93		
	30	pJX32	GFP-INCENP(1-491; F21RL33R)	pCS2	2.15		
	31	pJX33	GFP-INCENP(1-110)	pCS2	1.75		
	32	pJX34	GFP-INCENP(1-110; F21RL33R)	pCS2	1.36		
	33	GFP-SBP			0.3		For TnT
	34	INCENP 492-878			0.5		For TnT
	35	MCAK-4A	pFastBac HTa		0.23		Ryoma Ohi
	36	pCS2+					
	37	pCZ59	GFP N-terminal tag		0.1		pET52b
	38	pCZ62					
	39	pCZ65	AFS1-Fc-His10				pET52b
	40	pCZ67	AFS1-ZZ-His10				pET52b
	41	pJ201-42108	3FLAG-Dppa2(1-77)			Kan	Alex Kelly/DNA2.0
	42	pJ201-42107	3FLAG-H2B			Kan	Alex Kelly/DNA2.0
	43	pJR13	Op18-AAA				Jessica Rosenberg
	44	pCAGGS NGE	GFP under CMV promoter		0.94		Maria Jasin

Box	ID	Name	Description	Vector	mg/ml	Marker	Notes
1	45	pCP-TagRFP-T	His6-FLAG-TagRFP		0.05		Roger Tsien
	46	pEMW6pfd	GST-FLAG-Dppa2		0.69		pGEX6p-1
	47	pEMW6pfd-K42R	GST-FLAG-Dppa2(K42R)				
	48	pEMW6pfd-K230R	GST-FLAG-Dppa2(K230R)				
	49	pEMW6pfd-Ubc9	GST-FLAG-Dppa2-Ubc9		0.43		
	50	pEMW6p-gfp-d	GST-GFP-Dppa2				
	51	pJX41	Dppa2(1-77)-MCAK(4A)		0.14	Kan	
	52	pJX42	H2B-MCAK(4A)		0.19	Kan	
	53	pJX43	GST-Dppa2-SUMO2				
	54	pJX44	GST-SUMO2-Dppa2				
	55	pJX45	GST-FLAG-Dppa2(K42R)-Ubc9				
	56	pJX46	GST-Ubc9-Dppa2				
	57	pJX47	GST-Ubc9-Dppa2(K42R)				
	58	pJX48	Dppa2(1-77)-MCAK(4A)			Kan	Remove EcoRI site from pJX41
	59	pJX49	H2B-MCAK(4A)			Kan	Remove EcoRI site from pJX42
	60	pJX50	Dppa2(1-77)-MCAK(4A)		1.1		pCS2
	61	pJX51	H2B-MCAK(4A)		1		pCS2
	62	pJX52	Dppa2(1-77;K42R)-MCAK(4A)		1.25		
	63	pJX53	H2B-MCAK(4A)		1.23		Add initiation Met to pJX51
	64	pJX54	GST-SAP-Op18(AAA)				

Box	ID	Name	Description	Vector	mg/ml	Marker	Notes
1	65	pJX55	GST-SAP(K42R)-Op18(AAA)				
	66	pJX57	GST-FLAG-Dppa2				Delete EcoRI site 2 from pEMW6pfd
	67	pJX58	GST-FLAG-Dppa2				Delete EcoRI site 1 from pEMW6pfd
	68	pJX59	GST-Op18(AAA)				Delete NheI site from pJR11
	69	pJX60	H2B-TagRFP				pCS2
	70	pJX61	GST-SUMO2a-Dppa2				
	71	pJX62	GFP-Dppa2		0.7		pCS2
	72	pJX63	GFP tag		1.03		pcDNA3
	73	pJX64	FRT LAP tag		0.47		pcDNA5
	74	pJX65	FRT Dppa2		6		
	75	pJX66	FRT Dppa4		0.09		
	76	pJX67	FRT Dppa2		0.17		
	77	pcDNA3 tau	Tau-eGFP		0.19		CMV promoter
	78	pAC1	GST-Dppa2		0.18		Mutated EcoRI site to BglII in pEMW6pfd
	79	pAC3	GST-hDppa4				
	80	pAC4	GFP-hDppa2		1.1		pCS2
	81	pAC5	GFP-hDppa4		2.5		pCS2
2	1	pAC7	GFP-hDppa2	pcDNA5 FRT	1.1		
	2	pAC8	GFP-hDppa4	pcDNA5 FRT	0.9		
	3	pAC9	GFP-Dppa2	pcDNA5 FRT	0.22		
	4	pDW1		pAFS210	0.3		
	5	pAFS210	GFP				Aaron Straight

Box	ID	Name	Description	Vector	mg/ml	Marker	Notes
2	6	pKW2162	His_6-Rango-2	pRSET			Petr Kalab
	7	pKW2303	Rango-2 tissue culture expression; no marker				Petr Kalab
	8	pKW2388	His_6 Ran-binding sensor	pRSET			Petr Kalab
	9	BAF ZZ	BAF and ZZ tag	pIDTSmart	0.05		synthetic gene
	10	ALADIN			0.31		EST library 2015
	11	Lap2β			1		EST library 2051
	12	Laminin R1			0.69		EST library 265
	13	Nup98			0.05		EST library 284
	14	LBR					EST library 2595
	15	pJX72	LBR-GFP in pCS2		2.5		LBR cDNA from IMAGE 8331622
	16	SUN1	N terminus (1-463)	pBluescript SK-	0.19		IMAGE 6326555
	17	pJX75	MBP-His6-Dppa2				
	18	pJX76	MBP-His6-Dppa2 K42R				
	19	pJX77	MBP-His6-Dppa2 K230R				
	20	pJX78			0.16		
	21	pJX79	GST-SUN1				
	22	SUN2		pCMV-SPORT6			IMAGE 4173442
	23	pJX80	MBP-SUN2 (1-152)				
	24	pJX81			0.32		
	25	pJX82	GFP-BAF-His_6		0.05		
	26	pJX83	MBP-His_6-hDppa2				
	27	pJX84	MBP-His_6-hDppa4				
	28	pJX85	GFP-LRMP-His_8				
	29	pJX86	GFP-Dppa2-K42R		0.64		

Box	ID	Name	Description	Vector	mg/ml	Marker	Notes
2	30	pJX87	GFP-Dppa2-K230R		1.2		
	31	p50 dynamitin	Human p50 under T7				
	32	pJX88	His_6-BAF-TagRFP		0.11		
	33	pJX93	MBP-His_6-eGFP		0.18		
	34	pJX94	MBP-His_6-TagRFP		0.1		
	35	pJX97	MBP-His_6-Dppa2(ΔSAP)				Turbo K12
	36	pJX98	MBP-His_6-Dppa2(ΔDCR)				Turbo K12
	37	pJX99	MBP-His_6-Dppa2(ΔC)		0.05		Turbo K12
	38	pJX101	MBP-His_6-Dppa2		0.08		Turbo K12
	39	Lamin B3			0.7		IMAGE 5156585
	40	pJX104	MBP-His_6-Lamin B3		0.1		
	41	pJX105	GST-Lamin B3		0.7		
	42	pJX106	MBP-Lamin B3 CTD		0.1		
	43	pJX107	GST-Lamin B3 CTD		0.1		
	44	pJX108	MBP-His_6-LBR		0.05		
	45	pJX109	GST-LBR		0.12		
	46	pJX110	MBP-LBR NTD		0.12		
	47	pJX111	GST-LBR NTD		0.29		
	48	pJX113	GST-SUN2		0.1		
	49	pJX114	MBP-Dppa2 (77-242)		0.04		
	50	pJX115	MBP-Dppa2 (157-242)		0.03		
	51	pJX116	MBP-Dppa2 (196-242)		0.05		
	52	pJX117	MBP-Dppa2				
	53	EMAP4					IMAGE 5085289
	54	pJX119	SAP-GFP-His				
	55	pJX120	MBP-Dppa2 (114-242)				

Box	ID	Name	Description	Vector	mg/ml	Marker	Notes
2	56	pJX121	MBP-Dppa2 (144-242)				
	57	pJX127	His-TEV-Dppa2(144-240)			Kan	
	58	pJX128	pJX128 MBP-XDppa2-His				No FLAG
	59	pJX129	GFP-XDppa2 (144-242)				
	60	pJX131	MBP-GST-His				
	61	pJX132	MBP				
	62	pJX133	GFP-His				
	63	pJX134	GST-GFP				
	64	mKO2-Cdt1	FUCCI PiggyBac				
	65	mAG-Geminin	FUCCI PiggyBac				
	66	PiggyBac	Transposase				
	67	pJX136	MBP-TEV-Dppa2(144-242)-TEV-His				
	68	pJX137	MBP-Dppa2-His				
	69	pJX139	MBP-Dppa2-His				Rigid linker
	70	pJX140	MBP-Dppa2(144-242)-His				Rigid linker
	71	pJX141	MBP-SP4				Protamine
	72	pCola Duet	Bicistronic				
	73	pET Duet	Bicistronic				
	74	CRISPR lenti					
	75	PX330	SpCas9 and sgRNA				

Table 6-4. Labeled antibodies

Immunogen	Conjugate	Concentration (mg/ml)	Ratio label/ protein	Date
Lamin B3	Alexa Fluor 568 SE	0.14	0.83	6/14/12
mAb414	Alexa Fluor 568 SE	0.3	4.4	6/14/12

Table 6-5. Modified tubulins

Conjugate	Concentration (μM)	Ratio label/protein	Date
Alexa Fluor 488 SE	190	0.6	6/14/12
Alexa Fluor 594 SE	94	1.9	8/17/11
Alexa Fluor 647 SE	151	0.36	2/7/12
Recycled	100		2/5/15

As at 2/5/15, have 140 mg phosphocellulose-purified tubulin suitable for labeling. Also have commercial stocks of biotinylated tubulin (Cytoskeleton T333P) and rhodamine-tubulin (Cytoskeleton TL334M).

Appendix A. Visualizing membranes with lipophilic dye

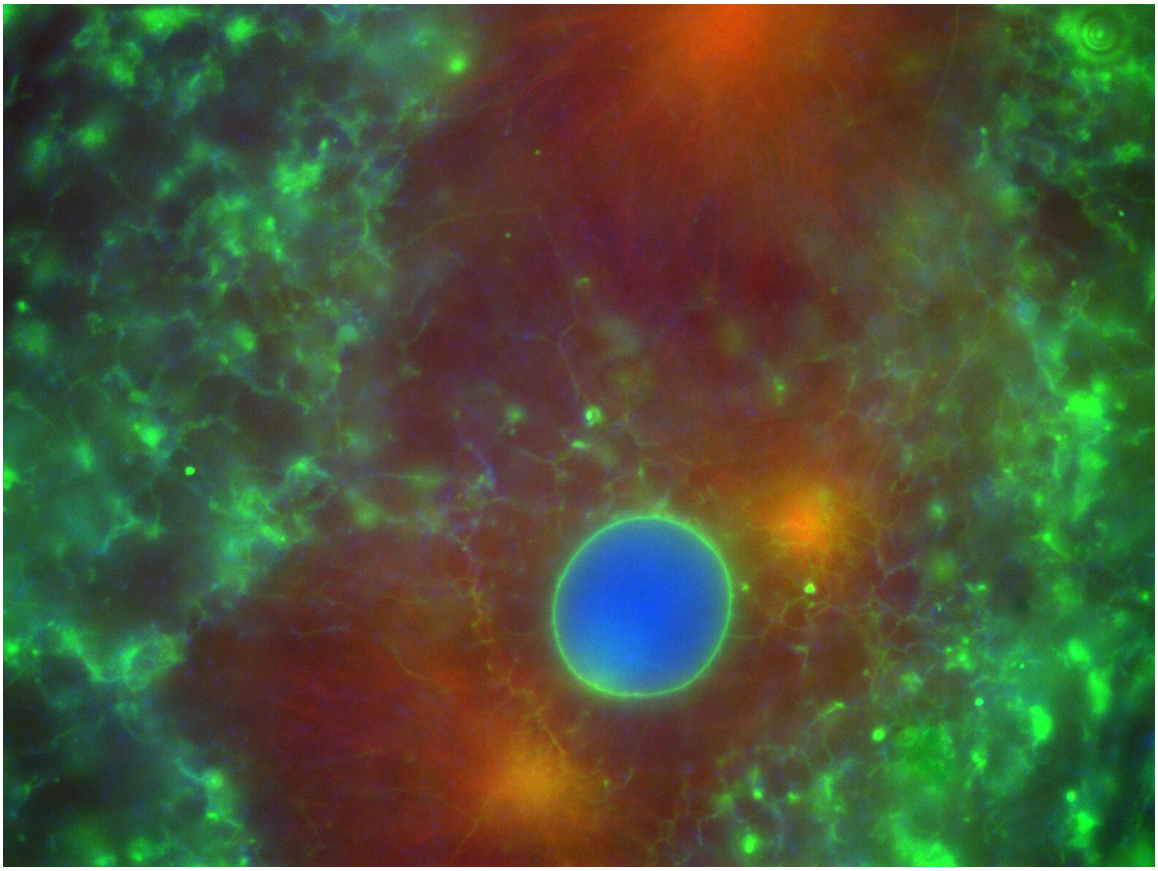

Figure A-1. Visualizing ER membranes

The long-chain lipophilic dye $DiOC_{18}$ (Sigma D4292; 1 μg/ml; green) must be preincubated with extracts for 30 min to incorporate into membranes. Extracts were then supplemented with DAPI (0.5 μg/ml; blue) and rhodamine-labeled tubulin (0.5 μM; red). After addition of sperm and calcium, extract was kept in the dark at room temperature for 50 min before imaging to reduce photobleaching of the membrane dye.

Appendix B. Towards the minimal microtubule-regulatory domain of Dppa2

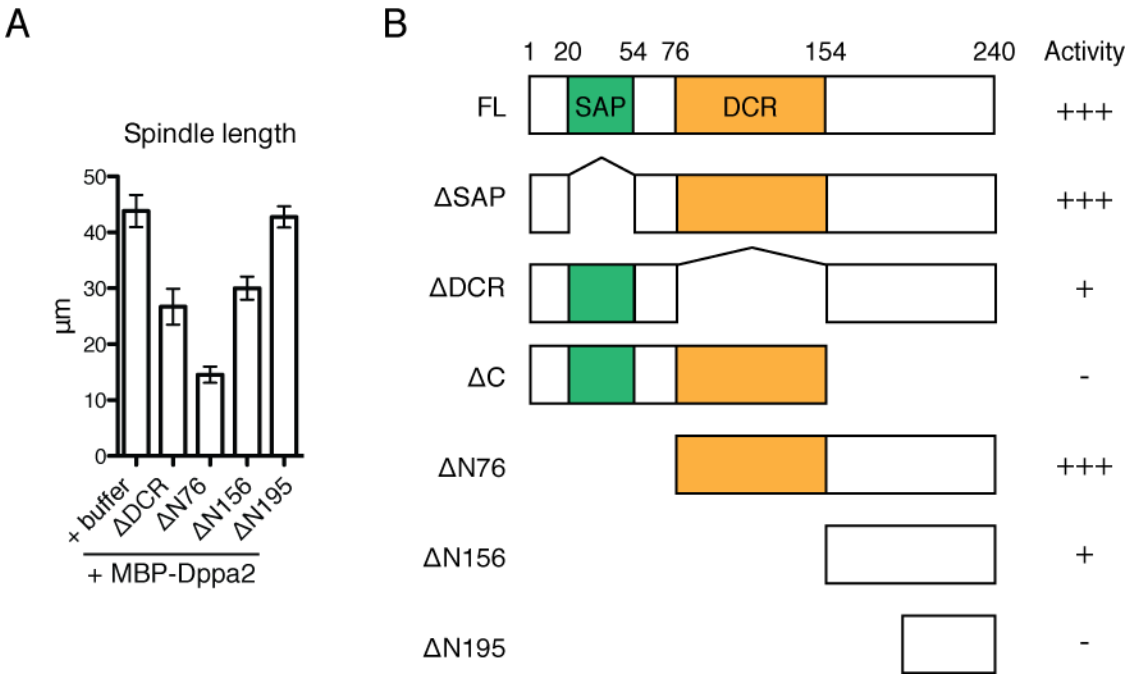

Figure B-1. The C-terminal 164 amino acids of *Xenopus* Dppa2 are sufficient to suppress microtubule assembly

(A) Length of spindles assembled in *Xenopus* egg extracts supplemented with MBP-tagged proteins (4 µM). Each column represents mean of >30 spindles, error bars indicate 95% confidence intervals.

(B) Summary of microtubule depolymerization experiments in this thesis.

Appendix C. DNA-binding determinants of *Xenopus* Dppa2

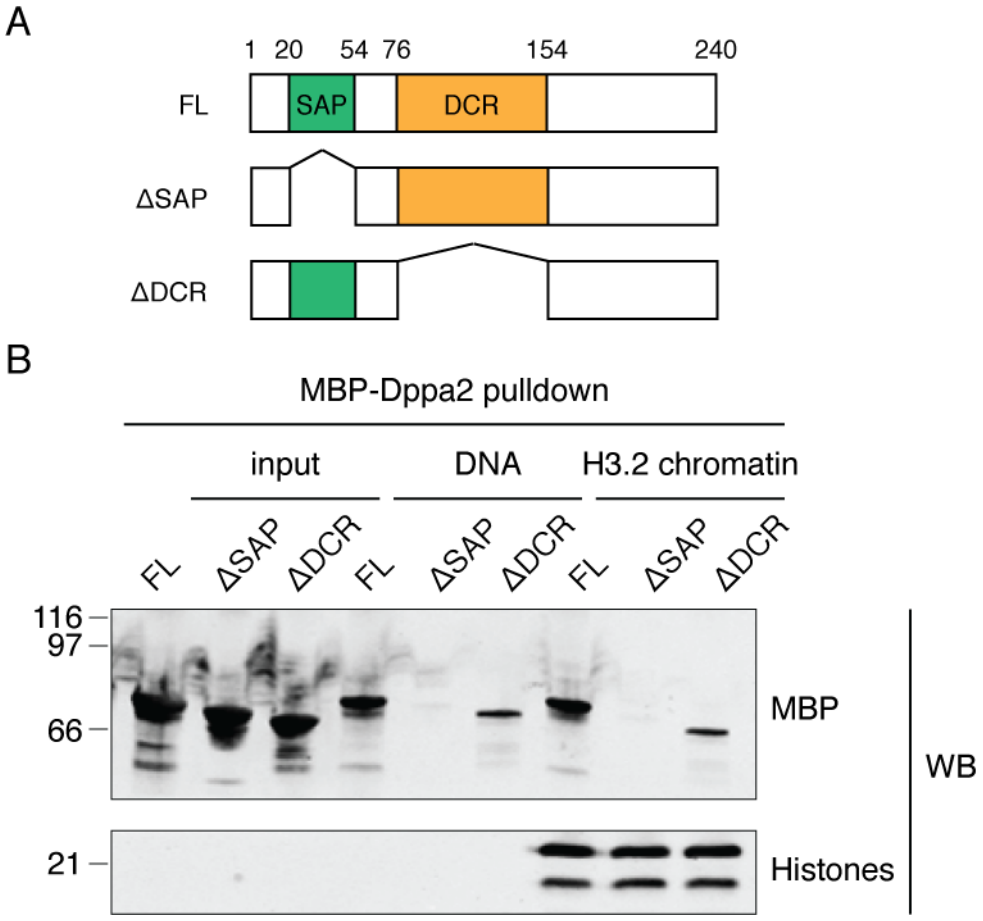

Figure C-1. In vitro interaction between *Xenopus* Dppa2 and chromatin

(A) Schematic of MBP-tagged Dppa2 deletion mutants used in this Figure.

(B) Recombinant Dppa2 proteins were incubated with magnetic beads coupled to naked plasmid DNA or nucleosome arrays assembled on 19 repeats of the 601 positioning sequence (Zierhut et al., 2014), and analyzed by western blotting.

The SAP and DCR domains of mouse Dppa4 were reported to bind DNA and histones respectively (Masaki et al., 2010). We found that the DCR domain of *Xenopus* Dppa2 was insufficient for binding to nucleosome beads and the SAP domain was essential. FRAP experiments showed that the SAP domain alone can bind sperm chromatin but has a very short residence time ($t_{1/2}$ = 1.12 s; Matthew Takata, unpublished), suggesting that the DCR may be required to stabilize binding to chromatin.

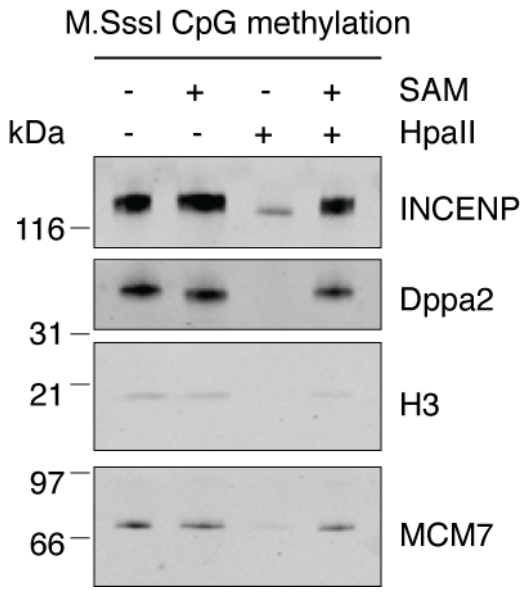

Figure C-2. Dppa2 has no preference for methylated DNA

3 μg biotinylated pBluescript plasmid DNA was immobilized on magnetic streptavidin-coated beads (Postow et al., 2008). Beads were treated with 12 U M.SssI CpG DNA methyltransferase (NEB M0226) and 160 μM S-adenosylmethionine (SAM) at 37 °C in 150 μl volume for 4 h. SAM was replenished after each hour. Enzyme was removed by washing beads with 20 mM HEPES [pH 8] + 2 M NaCl. Extent of methylation reaction was checked by protection from digestion by the methylation-sensitive restriction enzyme HpaII. Beads were incubated in CSF-arrested *Xenopus* egg extracts for 45 min, and co-purifying proteins analyzed by western blotting.

Appendix D. Effect of CpG methylation on DNA-binding proteins

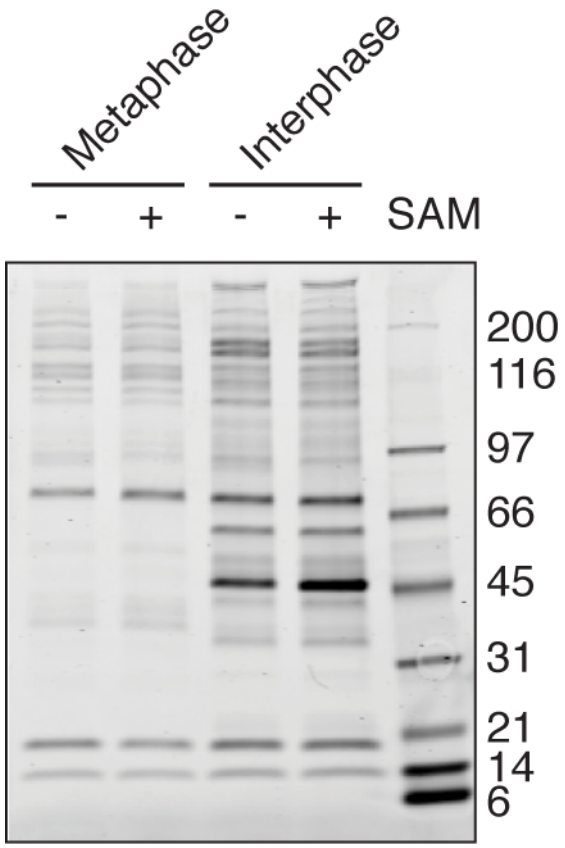

Figure D-1. Effect of CpG methylation on DNA-binding proteins in *Xenopus* egg extracts

Plasmid DNA-coated beads were methylated with M.SssI DNA methyltransferase. SAM was omitted for an unmethylated control. DNA beads were incubated in metaphase or interphase *Xenopus* egg extracts, and co-purifying proteins analyzed by Coomassie staining.

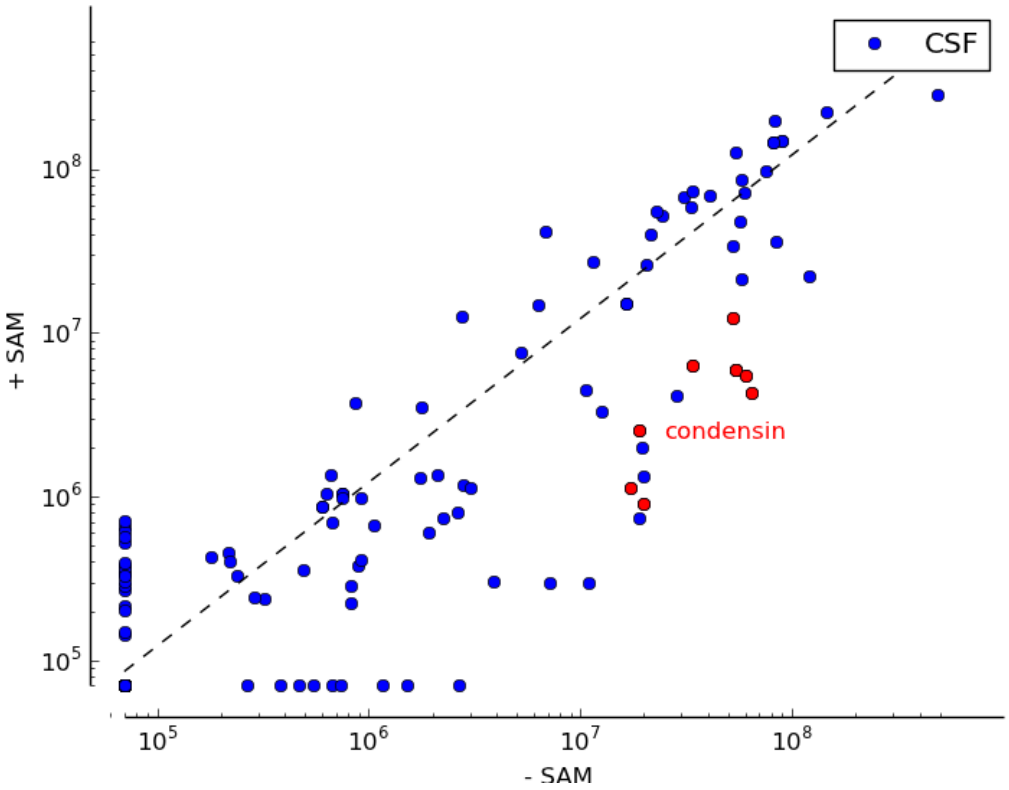

Figure D-2. Effect of CpG methylation in metaphase

Abundance of proteins copurifying with methylated DNA in CSF-arrested metaphase extracts measured by mass spectrometry.

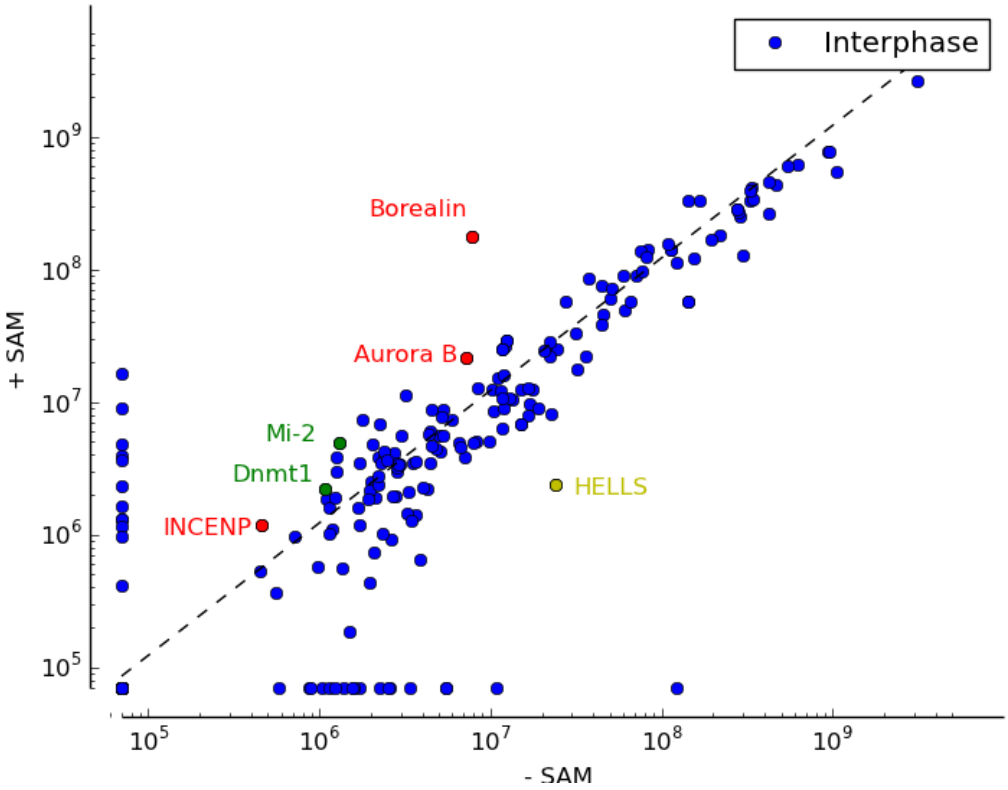

Figure D-3. Effect of CpG methylation in interphase

Abundance of proteins copurifying with methylated DNA in interphase extracts measured by mass spectrometry.

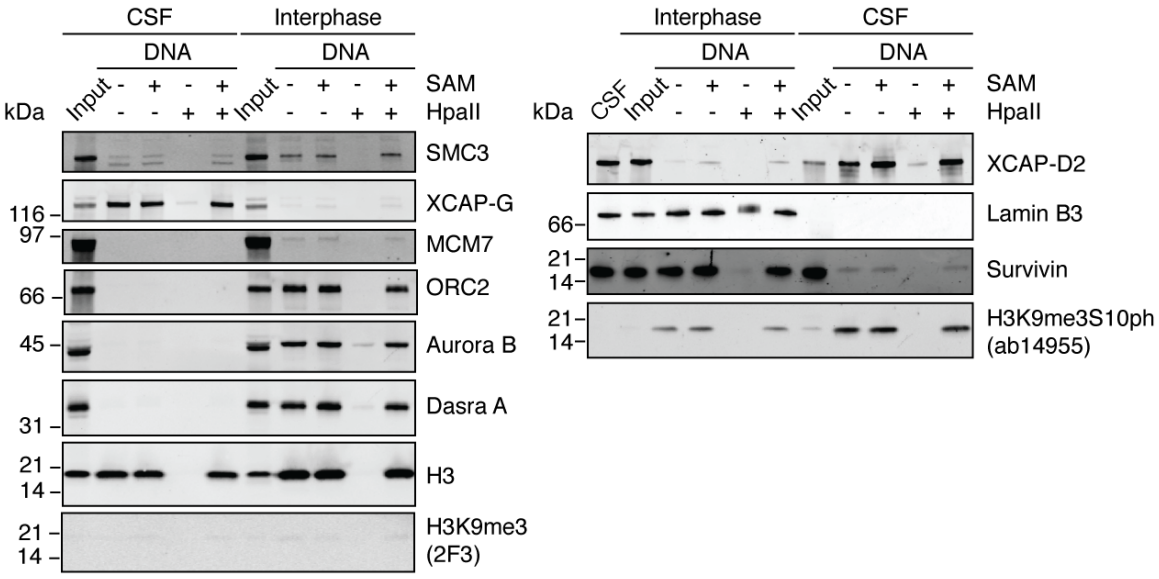

Figure D-4. Most DNA-binding proteins are not affected by DNA methylation

Analysis of proteins co-purifying with methylated DNA beads by western blotting. The CPC is ~30% enriched on methylated DNA.

Appendix E. Anti-lamin B3 and anti-MBP antibodies

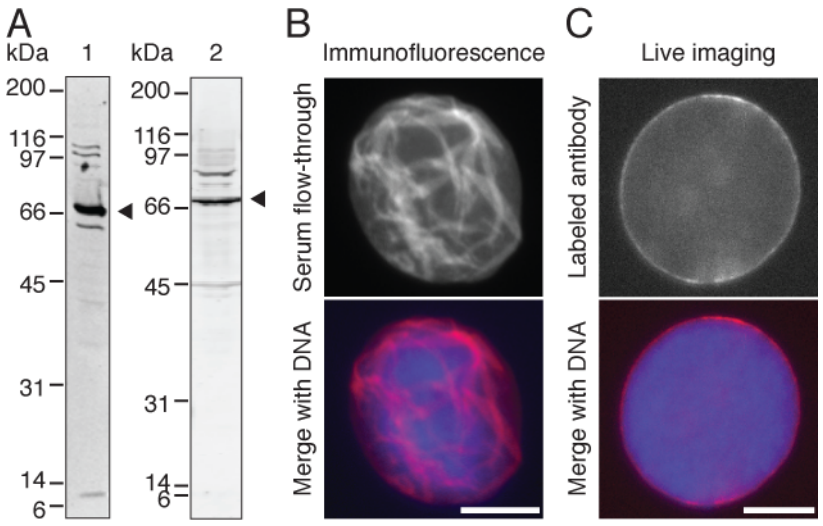

Figure E-1. Anti-lamin B3 antibodies

(A) The C terminus of *X. laevis* lamin B3 ($LB3_C$; residues 373-583) was purified as an MBP fusion from *E. coli* and used to immunize two rabbits (Proteintech; project S4118). Polyclonal antibodies were purified from test bleed sera using GST-$LB3_C$ immobilized on glutathione sepharose by dimethyl pimelimidate (30 mM) crosslinking. Antibodies were stored in PBS + 50% glycerol (rabbit 1: 0.3 mg/ml; rabbit 2: 0.18 mg/ml), and tested by western blotting (1 µg/ml in PBS + 2% BSA + 0.1% Triton X-100) against 0.5 µl egg extract. Arrowheads indicate lamin B3 (67 kDa).

(B) Nuclei were spun onto coverslips and stained using serum flow-through saved from antibody purification (rabbit 1; 1/100 in PBS + 2% BSA + 0.1% Triton X-100).

(C) Affinity-purified antibodies were labeled with Alexa Fluor 568 succinimidyl ester (Invitrogen A20184) and stored in PBS + 2 mM NaN_3 (0.14 mg/ml, 0.83× label stoichiometry). Nuclei were assembled in egg extract supplemented with labeled antibodies (1/100) and Hoechst 33342 (0.5 µg/ml).

Scale bars, 10 µm.

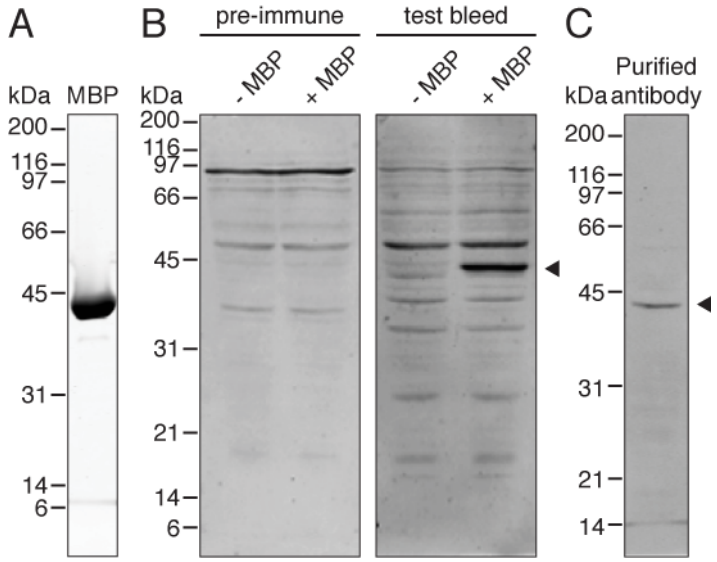

Figure E-2. Anti-MBP antibodies

(A) MBP was expressed in *E. coli*, purified using amylose resin and used to immunize one rabbit (Cocalico; project RU1991).

(B) Pre-immune and test bleed sera were diluted 1/100 in PBS + 4% non-fat milk and tested against 0.5 µl egg extract supplemented with buffer or 1 µM MBP. Arrowhead indicates MBP (43 kDa).

(C) Polyclonal antibodies were purified from test bleed sera using MBP immobilized on Affigel 15, and stored in PBS + 50% glycerol (1.8 mg/ml). Antibodies were tested by western blotting (1 µg/ml in PBS + 2% BSA + 0.1% Triton X-100) against 0.3 µl egg extract supplemented with 1 µM MBP. Arrowhead indicates MBP (43 kDa).

Appendix F. Full sequence alignment of putative Dppa2 orthologs

Accessions: *P. bivittatus* (XP_007425058.1), *A. carolinensis* (XP_008120055.1), *P. antarctica* (GAK64391.1), *U. maydis* (XP_011389067.1)

```
Xenopus laevis Dppa2             ------------------------------------------------------------MP
Xenopus tropicalis Dppa2         ------------------------------------------------------------MP
Python bivittatus (predicted)    ------------------------------------------------------------MP
Anolis carolinensis (predicted)  ----------MNQQIQGKGKRVSLPKTALKNVIPRQDYTAQPSLDATNTSRDKRRDFGMP
Pseudozyma antarctica (predicted)------------------------------------------------------------
Ustilago maydis (predicted)      ------------------------------------------------------------
Homo sapiens Dppa2               MSDANLDSSKKNFLEGEVDDEESVILTLVPVKDDANMEQMEPSVSSTSDVKLEKPKKYNP
Mus musculus Dppa2               MSYFGLETFNENQSEENLDEE-SVILTLVPFKEEEEPNTDYATQSNVSSSTLDHTP---P

                                                                                --SAP motif--
Xenopus laevis             --------------KRRAKTP--AP-EPDLTPN--------------SLQLLKRAQLQQH
Xenopus tropicalis         --------------KRQGKNP--APPQPDLTPS--------------SLQLLKRAQLQQH
Python bivittatus          --------------RQGRKTTKSTSTLPLRTPAKDSSCQPLSATFSVDYNTLKRAQLQLQ
Anolis carolinensis        --------------RQSRKIAKSASTPP--------QCAPVNRATSVDYSVLKRAQLQQL
Pseudozyma antarctica      -------------------------------------MATNMLLSPEALHCLKRKQLTNL
Ustilago maydis            ----------------------------------------MLLSPHALHCLKRKQLTNL
Homo sapiens               GHLLQTNEQFTAPQKARCKIP-ALPLPTILPPINK----------------VCRDTLRDW
Mus musculus               ARSLVRH----AGIKHPTRTIPSTCPPPSLPPIRD----------------VSRNTLREW
                                                                                *  *

                           -------SAP motif-------
Xenopus laevis             CKRLGLRGTGKNAELVQRLQEYF-------------------------------------
Xenopus tropicalis         CKRLGLRGTGKNAELVQRLLEYF-------------------------------------
Python bivittatus          CKKLGLRATGKNTELVERLKAHH-------------------------------------
Anolis carolinensis        CKKLGIRATGKNSELLERVKAFH-------------------------------------
Pseudozyma antarctica      CRRFGIKAVGKNADLIQRLQEYAASNIPSDSPTKGNVAVLRHIKRPRQSDAS----SDSD
Ustilago maydis            CRRFGIKVVGKNADLIQRLQEYAASNIPIDSPTKGNVPILRHVKRRRQSDSS----QESV
Homo sapiens               CQQLGLSTNGKKIEVYLRLHRHAYPEQRQDMPEMSQETRLQRCSRKRKAVTKRARLQRSY
Mus musculus               CRYHNLSTDGKKVEVYLRLRRHSYSKQECYIPNTSREARMKQGPKKSKIVFRG--IGPPS
                           *        **      *
```

Appendix F. Full sequence alignment of putative Dppa2 orthologs

```
Xenopus laevis                ------------------------------QQAA---ANEQEE----------DPTTPSL
Xenopus tropicalis            ------------------------------QQAA---ANQ--E----------DPQTPSP
Python bivittatus             ------------------------------GESSLKMACNKEE-TNKSEESSHNFGTPVM
Anolis carolinensis           ------------------------------KEPLCEIVNTKEENTKKDEEKDQKAQAPLP
Pseudozyma antarctica         SDNQYDEQKPTTVYPPLTPRTRQKRVSDI-VQAIEEVKAQPDE-MDSDDELD-DPEVKSP
Ustilago maydis               NDELLSAEAASLPNPPLTPRTRQKRISDL-VQAIEQVKGQDDG-MNTDE--D-DDEGVFT
Homo sapiens                  EMNERAEETNTVEVITSAPGAMLASWARIAARAVQPKALNSCS-------------IPVS
Mus musculus                  GCQRKKEESGVLEILTSPKESTFAAWARIAMRAAQSMSKNRCP-----------------

                                                 ----------------DCR motif-----------------
Xenopus laevis                D---------ENEK---ESEEVTVGRGW----------CVVHGQEM--TVSSWKPLFLRC
Xenopus tropicalis            E---------KDES---VSGELTGGRGW----------CVVHGQEL--TVSRWKPLFLRC
Python bivittatus             APPLDLAKDIKTET---SEEKTDMVRGW----------CVVHGMVLYRPASSWVPLLLRG
Anolis carolinensis           APPVALNKEIKFEV---FEKKTEVVHGW----------CVVHGMILYRPESSWFPLLLRG
Pseudozyma antarctica         SCKNTIAFPVKQQQ-----APLS-PQ---STQPLRIIKALPSSTRLASPLSTATILELSR
Ustilago maydis               SQKSTIAFPCSSPRPVSTIAPVSGPQQCESTQPLRIIKALPNADRITSPLSTATILELSR
Homo sapiens                  V-----------EA---FLMQASGVR-W----------CVVHGRLLSADTKGWVRLQFHA
Mus musculus                  -------LPSNVEA---FLPQATGSR-W----------CVVHGRQLPADKKGWVRLQFLA
                                                                                        *
                                                 ----------------------DCR motif----------------------
Xenopus laevis                GRVCVTC-EGSCVPLHLTPSSFPTPCGLQDNLICDECFERNQER--ECRLQQR------S
Xenopus tropicalis            GRVCMTF-EGSCIPLHLTPSSTPTPCGLQDNLICEECFERNQER--ECRLQQR------S
Python bivittatus             GLVCVQD-GENLVPFHLPPLNISVPEGLLDNYVCKDCVLRNQEKPKKCTLCQQIQGKGST
Anolis carolinensis           GMVYVQD-GENHVPFHLPVTNISVPEGLSDNYICRECVLRNQEKLKKHPMNQQIQGKGKR
Pseudozyma antarctica         PPAAHEASNSATASMYPDISTLPLPEGISS-----DCLASSSTLP--SITSRQFSAAAAS
Ustilago maydis               TPAAKDGNSS----LYPDLSSLPLPQGVSS-----DCLTSSSTLP--SITSRQFSAAAAS
Homo sapiens                  GQAWVPTTHRRMISLFLLPACIFPSPGIEDNMLCPDCAKRNKKMMKRLMTVEK-------
Mus musculus                  GQTWVPDTPQRMNFLFLLPACIIPEPGVEDNLLCPECVHSNKKILRNFKIRSR-------
                                                 *         *
```

Appendix F. Full sequence alignment of putative Dppa2 orthologs

```
Xenopus laevis              VFQD-NY-----PPMGQMRKS-VSTTRTRKKSGR-------FQPQEDPEYARRVDELLDQ
Xenopus tropicalis          AFQDKNY-----PPSGQMRKSTISASRSRKKSGR-------FQPQEDPEYARRVDELLGQ
Python bivittatus           AYLSQNFFKNLSPLVKSTSSSSLLAAGGSKEKRRTVEIKKLYQPQEDQAYAQRVDGILSQ
Anolis carolinensis         VSLPKTALKNVIPRQDYTAQPSLDATNTSRDKRRTIEIRKLYQPQEDEAYAQRVDGLLSL
Pseudozyma antarctica       VLAEMNA---RLTAAGRSTTSASLATMSSMGNGA-------WQTLASSTSTQGMSQ--SR
Ustilago maydis             VLAEMNA---RLTAAGRSATSGSLATMSSIGNGT-------WQNLVASASSQGMSK--SH
Homo sapiens                ------------------------------------------------------------
Mus musculus                --AKKNALPPNMPP------------------------------------------------

Xenopus laevis              LATGQVDSQKILKPSRPAVLHSPLPKPESSPIAINQ-----------------------
Xenopus tropicalis          LATGQVDSQKVLKPSRPAVMHSPLAKPESSPIAIDQ-----------------------
Python bivittatus           MARGELGMDRALRPLQPLVVHSPAPYGR-------------------------------
Anolis carolinensis         MARGELGMDLALRPVQPLVVHSPAPFEK-------------------------------
Pseudozyma antarctica       SGRYEIQHERQFKKMDSIVNHYAARRVG------TADKSDASASTSSRSETSSS--VVAA
Ustilago maydis             SGRYEIHHERQFQKMDSIVNHYAARRVGAGLAAVSADKVESASKSSADSDSASSSFTLAA
Homo sapiens                ------------------------------------------------------------
Mus musculus                ------------------------------------------------------------

Xenopus laevis              ------------------------------------------------------------
Xenopus tropicalis          ------------------------------------------------------------
Python bivittatus           ------------------------------------------------------------
Anolis carolinensis         ------------------------------------------------------------
Pseudozyma antarctica       TKSLAV------------ARKPQRVDASTSTRSLAAMVHSTSTRKVASQRRPLPVPPAL
Ustilago maydis             TANTGASVADACMTANTSSSRRP-RVDASTSTRSLAAVARSSSTHKLPVQRRPLPTPPVS
Homo sapiens                ------------------------------------------------------------
Mus musculus                ------------------------------------------------------------
```

Appendix F. Full sequence alignment of putative Dppa2 orthologs

```
Xenopus laevis              ------------------------------------------------------------
Xenopus tropicalis          ------------------------------------------------------------
Python bivittatus           ------------------------------------------------------------
Anolis carolinensis         ------------------------------------------------------------
Pseudozyma antarctica       KACSKPPAAATTRVANLPSSRQAS-----------GSEAPRTKRLRLAVTEDQGALQNT
Ustilago maydis             STRSSRMLSTSSTRAQIVKLRQASTNTTTTSTSRSNANDPPRAKRLRLAVSEDQDALQNT
Homo sapiens                ------------------------------------------------------------
Mus musculus                ------------------------------------------------------------

Xenopus laevis              ------------------------------------------------------------
Xenopus tropicalis          ------------------------------------------------------------
Python bivittatus           ------------------------------------------------------------
Anolis carolinensis         ------------------------------------------------------------
Pseudozyma antarctica       VLEIPPEKKTVMIRVTRPEREGMPYQVSVAPSTSEAKKLGEASGPVRAASVLRKSVIKAT
Ustilago maydis             VLEIPPEKKTVVIRVTRPDRDGMPYKFSVASSCTTD---GE-SAPTRAASSLRKTVIKAT
Homo sapiens                ------------------------------------------------------------
Mus musculus                ------------------------------------------------------------

Xenopus laevis              ------------------------------------------------------------
Xenopus tropicalis          ------------------------------------------------------------
Python bivittatus           ------------------------------------------------------------
Anolis carolinensis         ------------------------------------------------------------
Pseudozyma antarctica       KSTFTG-GSAKKTTASAQAQKREAAFTKQQQHAAAMSRSMSSRANLAPAVSRSEGLPAST
Ustilago maydis             KGTFVGSSSAKKLATGVQSQRREMTFVKQQQQQAAMSRSISSRANLASA--EQSGMTNST
Homo sapiens                ------------------------------------------------------------
Mus musculus                ------------------------------------------------------------
```

Appendix F. Full sequence alignment of putative Dppa2 orthologs

```
Xenopus laevis              ------------------------------------------------------------
Xenopus tropicalis          ------------------------------------------------------------
Python bivittatus           ------------------------------------------------------------
Anolis carolinensis         ------------------------------------------------------------
Pseudozyma antarctica       SVRNKFTGALTAPPTATRTPVAAALTGSGASVVPSEASKGSV-TRLGGSIRSSVSQGLGR
Ustilago maydis             STRNKFTG-VTTMNCDTHKPLTAVSTLSGVAEGSKHSSTNSLSSRFGGSIRSSVSQGLGR
Homo sapiens                ------------------------------------------------------------
Mus musculus                ------------------------------------------------------------

Xenopus laevis              ------------------------------------------------------------
Xenopus tropicalis          ------------------------------------------------------------
Python bivittatus           ------------------------------------------------------------
Anolis carolinensis         ------------------------------------------------------------
Pseudozyma antarctica       ADAARQARLKEIKARTKAALAGFGSSRT----------VDAAAPESP----RKGATFSPS
Ustilago maydis             AEVARQARLKEIKARTKAALAGFGSQRNVSGDTLNNTDVDAGASQHKIVPCSQASSFSPS
Homo sapiens                ------------------------------------------------------------
Mus musculus                ------------------------------------------------------------

Xenopus laevis              ------------------------------------------------------------
Xenopus tropicalis          ------------------------------------------------------------
Python bivittatus           ------------------------------------------------------------
Anolis carolinensis         ------------------------------------------------------------
Pseudozyma antarctica       VTRPTIASLNRA-----VTTTGGSASLPMLSAIT---APLCGLNA--NVVEGLQRAATMH
Ustilago maydis             VMRPTIASLNRSSAASPSTGSNASASLPMLSAISRAAAPSTGLKAVHGAVVGLQRAATVH
Homo sapiens                ------------------------------------------------------------
Mus musculus                ------------------------------------------------------------
```

Appendix F. Full sequence alignment of putative Dppa2 orthologs

```
Xenopus laevis              ------------------------------------------------------------
Xenopus tropicalis          ------------------------------------------------------------
Python bivittatus           ------------------------------------------------------------
Anolis carolinensis         ------------------------------------------------------------
Pseudozyma antarctica       AGVG-ALMPSLTPRSSSLRHLRRVMRKQQKQAEVDHERVAAAENISPGKVVPSVI-----
Ustilago maydis             AGVSKVLTPCLTPRSSSLRHLRRVMRKQQKEADLVQVRVVAAENIAPGDVVPSVVIASNT
Homo sapiens                ------------------------------------------------------------
Mus musculus                ------------------------------------------------------------

Xenopus laevis              ------------------------------------------------------------
Xenopus tropicalis          ------------------------------------------------------------
Python bivittatus           ------------------------------------------------------------
Anolis carolinensis         ------------------------------------------------------------
Pseudozyma antarctica       ------KPTT--SELQYAPSIRTVAKVQPSPDKYTTLPLK-GRTAARPAGARSALVTSHA
Ustilago maydis             QALVSNKPDTVQDEQVAKPSIRTVA-VRSSPTK--LLPLNTTQTVPRPAGPRAPLVATRT
Homo sapiens                ------------------------------------------------------------
Mus musculus                ------------------------------------------------------------

Xenopus laevis              --------
Xenopus tropicalis          --------
Python bivittatus           --------
Anolis carolinensis         --------
Pseudozyma antarctica       TTSALNRI
Ustilago maydis             TISATNRR
Homo sapiens                --------
Mus musculus                --------
```

References

Abrams EW, Zhang H, Marlow FL, Kapp L, Lu S and Mullins MC (2012). Dynamic assembly of Brambleberry mediates nuclear envelope fusion during early development. *Cell* **150**, 521-532.

Afonso O, Matos I, Pereira AJ, Aguiar P, Lampson MA and Maiato H (2014). Feedback control of chromosome separation by a midzone Aurora B gradient. *Science* **345**, 332-336.

Alushin GM, Lander GC, Kellogg EH, Zhang R, Baker D and Nogales E (2014). High-resolution microtubule structures reveal the structural transitions in αβ-tubulin upon GTP hydrolysis. *Cell* **157**, 1117-1129.

Anderson DJ and Hetzer MW (2007). Nuclear envelope formation by chromatin-mediated reorganization of the endoplasmic reticulum. *Nat. Cell Biol.* **9**, 1160-1166.

Antonio C, Ferby I, Wilhelm H, Jones M, Karsenti E, Nebreda AR and Vernos I (2000). Xkid, a chromokinesin required for chromosome alignment on the metaphase plate. *Cell* **102**, 425-435.

Aravind L and Koonin EV (2000). SAP - a putative DNA-binding motif involved in chromosomal organization. *Trends Biochem. Sci.* **25**, 112-114.

Asencio C, Davidson IF, Santarella-Mellwig R, Ly-Hartig TBN, Mall M, Wallenfang MR, Mattaj IW and Gorjánácz M (2012). Coordination of kinase and phosphatase activities by Lem4 enables nuclear envelope reassembly during mitosis. *Cell* **150**, 122-135.

Balakier H and Cadesky K (1997). The frequency and developmental capability of human embryos containing multinucleated blastomeres. *Human Reprod.* **12**, 800-804.

Basto R, Lau J, Vinogradova T, Gardiol A, Woods CG, Khodjakov A and Raff JW (2006). Flies without centrioles. *Cell* **125**, 1375-1386.

Beaudouin J, Gerlich DW, Daigle N, Eils R and Ellenberg J (2002). Nuclear envelope breakdown proceeds by microtubule-induced tearing of the lamina. *Cell* **108**, 83-96.

Becker BE and Gard DL (2006). Visualization of the cytoskeleton in Xenopus oocytes and eggs by confocal immunofluorescence microscopy. *Meth. Mol. Biol.* **322**, 69-86.

Belmont LD, Hyman AA, Sawin KE and Mitchison TJ (1990). Real-time visualization of cell cycle-dependent changes in microtubule dynamics in cytoplasmic extracts. *Cell* **62**, 579-589.

Belmont LD and Mitchison TJ (1996). Identification of a protein that interacts with tubulin dimers and increases the catastrophe rate of microtubules. *Cell* **84**, 623-631.

Bodmer R (1993). The gene tinman is required for specification of the heart and visceral muscles in Drosophila. *Development* **118**, 719-729.

Bohnsack MT, Stüven T, Kuhn C, Cordes VC and Görlich D (2006). A selective block of nuclear actin export stabilizes the giant nuclei of *Xenopus* oocytes. *Nat. Cell Biol.* **8**, 257-263.

Borisy GG, Marcum JM, Olmsted JB, Murphy DB and Johnson KA (1975). Purification of tubulin and associated high molecular weight proteins from porcine brain and characterization of microtubule assembly in vitro. *Ann. N.Y. Acad. Sci.* **253**, 107-132.

Bortvin A, Eggan K, Skaletsky H, Akutsu H, Berry DL, Yanagimachi R, Page DC and Jaenisch R (2003). Incomplete reactivation of Oct4-related genes in mouse embryos cloned from somatic nuclei. *Development* **130**, 1673-1680.

Botuyan MV, Lee J, Ward IM, Kim J-E, Thompson JR, Chen J and Mer G (2006). Structural basis for the methylation state-specific recognition of histone H4-K20 by 53BP1 and Crb2 in DNA repair. *Cell* **127**, 1361-1373.

Brandt A, Papagiannouli F, Wagner N, Wilsch-Bräuninger M, Braun M, Furlong EEM, Loserth S, Wenzl C, Pilot F, Vogt N, Lecuit T, Krohne G and Grosshans J (2006). Developmental control of nuclear size and shape by Kugelkern and Kurzkern. *Curr. Biol.* **16**, 543-552.

Brouhard GJ, Stear JH, Noetzel TL, Al-Bassam J, Kinoshita K, Harrison SC, Howard J and Hyman AA (2008). XMAP215 is a processive microtubule polymerase. *Cell* **132**, 79-88.

Budde PP, Kumagai A, Dunphy WG and Heald R (2001). Regulation of Op18 during spindle assembly in Xenopus egg extracts. *J. Cell Biol.* **153**, 149-158.

Budde PP, Desai A and Heald R (2006). Analysis of microtubule polymerization in vitro and during the cell cycle in Xenopus egg extracts. *Methods* **38**, 29-34.

Buganim Y, Faddah DA, Cheng AW, Itskovich E, Markoulaki S, Ganz K, Klemm SL, van Oudenaarden A and Jaenisch R (2012). Single-cell expression analyses during cellular reprogramming reveal an early stochastic and a late hierarchic phase. *Cell* **150**, 1209-1222.

Burke B and Stewart CL (2014). Functional architecture of the cell's nucleus in development, aging, and disease. *Curr. Top. Dev. Biol.* **109**, 1-52.

Cai S, Weaver LN, Ems-McClung SC and Walczak CE (2009). Kinesin-14 family proteins HSET/XCTK2 control spindle length by cross-linking and sliding microtubules. *Mol. Biol. Cell* **20**, 1348-1359.

Cai X, Chiu Y-H and Chen ZJ (2014). The cGAS-cGAMP-STING pathway of cytosolic DNA sensing and signaling. *Mol. Cell* **54**, 289-296.

Campbell CS and Desai A (2013). Tension sensing by Aurora B kinase is independent of survivin-based centromere localization. *Nature* **497**, 118-121.

Caplow M, Ruhlen RL and Shanks J (1994). The free energy for hydrolysis of a microtubule-bound nucleotide triphosphate is near zero: all of the free energy for hydrolysis is stored in the microtubule lattice. *J. Cell Biol.* **127**, 779-788.

Chaudhary N and Courvalin JC (1993). Stepwise reassembly of the nuclear envelope at the end of mitosis. *J. Cell Biol.* **122**, 295-306.

Chikashige Y, Tsutsumi C, Yamane M, Okamasa K, Haraguchi T and Hiraoka Y (2006). Meiotic proteins bqt1 and bqt2 tether telomeres to form the bouquet arrangement of chromosomes. *Cell* **125**, 59-69.

Clowney EJ, Legros MA, Mosley CP, Clowney FG, Markenscoff-Papadimitriou EC, Myllys M, Barnea G, Larabell CA and Lomvardas S (2012). Nuclear aggregation of olfactory receptor genes governs their monogenic expression. *Cell* **151**, 724-737.

Collart C, Christov CP, Smith JC and Krude T (2011). The midblastula transition defines the onset of Y RNA-dependent DNA replication in Xenopus laevis. *Mol. Cell. Biol.* **31**, 3857-3870.

Costa Y, Speed R, Ollinger R, Alsheimer M, Semple CA, Gautier P, Maratou K, Novak I, Höög C, Benavente R and Cooke HJ (2005). Two novel proteins recruited by synaptonemal complex protein 1 (SYCP1) are at the centre of meiosis. *J. Cell Sci.* **118**, 2755-2762.

Courtois A, Schuh M, Ellenberg J and Hiiragi T (2012). The transition from meiotic to mitotic spindle assembly is gradual during early mammalian development. *J. Cell Biol.* **198**, 357-370.

Crasta K, Ganem NJ, Dagher R, Lantermann AB, Ivanova EV, Pan Y, Nezi L, Protopopov A, Chowdhury D and Pellman D (2012). DNA breaks and chromosome pulverization from errors in mitosis. *Nature* **482**, 53-58.

Davidson PM and Lammerding J (2013). Broken nuclei - lamins, nuclear mechanics, and disease. *Trends Cell Biol.* **24**, 247-256.

Desai A, Verma S, Mitchison TJ and Walczak CE (1999). Kin I kinesins are microtubule-destabilizing enzymes. *Cell* **96**, 69-78.

Di Talia S, She R, Blythe SA, Lu X, Zhang QF and Wieschaus EF (2013). Posttranslational control of Cdc25 degradation terminates Drosophila's early cell-cycle program. *Curr. Biol.* **23**, 127-132.

Dimitrov A, Quesnoit M, Moutel S, Cantaloube I, Poüs C and Perez F (2008). Detection of GTP-tubulin conformation in vivo reveals a role for GTP remnants in microtubule rescues. *Science* **322**, 1353-1356.

Doucet CM, Talamas JA and Hetzer MW (2010). Cell cycle-dependent differences in nuclear pore complex assembly in metazoa. *Cell* **141**, 1030-1041.

Dreier L and Rapoport TA (2000). In vitro formation of the endoplasmic reticulum occurs independently of microtubules by a controlled fusion reaction. *J. Cell Biol.* **148**, 883-898.

Du J, Chen T, Zou X, Xiong B and Lu G (2010). Dppa2 knockdown-induced differentiation and repressed proliferation of mouse embryonic stem cells. *J. Biochem.* **147**, 265-271.

Eberhart A, Feodorova Y, Song C, Wanner G, Kiseleva E, Furukawa T, Kimura H, Schotta G, Leonhardt H, Joffe B and Solovei I (2013). Epigenetics of eu- and heterochromatin in inverted and conventional nuclei from mouse retina. *Chromosome Res.* **21**, 535-554.

Edgar BA and Datar SA (1996). Zygotic degradation of two maternal Cdc25 mRNAs terminates Drosophila's early cell cycle program. *Genes Dev.* **10**, 1966-1977.

Evans KJ, Gomes ER, Reisenweber SM, Gundersen GG and Lauring BP (2005). Linking axonal degeneration to microtubule remodeling by Spastin-mediated microtubule severing. *J. Cell Biol.* **168**, 599-606.

Ewald A, Zünkler C, Lourim D and Dabauvalle M-C (2001). Microtubule-dependent assembly of the nuclear envelope in *Xenopus laevis* egg extract. *Eur. J. Cell Biol.* **80**, 678-691.

Feinberg AP, Ohlsson R and Henikoff S (2006). The epigenetic progenitor origin of human cancer. *Nat. Rev. Genet.* **7**, 21-33.

Fernandez AG and Piano F (2006). MEL-28 is downstream of the Ran cycle and is required for nuclear-envelope function and chromatin maintenance. *Curr. Biol.* **16**, 1757-1763.

Filion GJ, van Bemmel JG, Braunschweig U, Talhout W, Kind J, Ward LD, Brugman W, de Castro IJ, Kerkhoven RM, Bussemaker HJ and van Steensel B (2010). Systematic protein location mapping reveals five principal chromatin types in Drosophila cells. *Cell* **143**, 212-224.

Firestone AJ, Weinger JS, Maldonado M, Barlan K, Langston LD, O'Donnell M, Gelfand VI, Kapoor TM and Chen JK (2012). Small-molecule inhibitors of the AAA+ ATPase motor cytoplasmic dynein. *Nature* **484**, 125-129.

Forbes B (2002). Pulmonary epithelial cell culture. *Meth. Mol. Biol.* **188**, 65-75.

Forbes DJ, Kirschner MW and Newport JW (1983). Spontaneous formation of nucleus-like structures around bacteriophage DNA microinjected into *Xenopus* eggs. *Cell* **34**, 13-23.

Franz C, Walczak R, Yavuz S, Santarella R, Gentzel M, Askjaer P, Galy V, Hetzer M, Mattaj IW and Antonin W (2007). MEL-28/ELYS is required for the recruitment of nucleoporins to chromatin and postmitotic nuclear pore complex assembly. *EMBO Rep.* **8**, 165-172.

Fuller BG, Lampson MA, Foley EA, Rosasco-Nitcher SE, Le KV, Tobelmann P, Brautigan DL, Stukenberg PT and Kapoor TM (2008). Midzone activation of Aurora B in anaphase produces an intracellular phosphorylation gradient. *Nature* **453**, 1132-1136.

Funabiki H and Murray AW (2000). The *Xenopus* chromokinesin Xkid is essential for metaphase chromosome alignment and must be degraded to allow anaphase chromosome movement. *Cell* **102**, 411-424.

Gadea BB and Ruderman JV (2006). Aurora B is required for mitotic chromatin-induced phosphorylation of Op18/Stathmin. *Proc. Natl. Acad. Sci. U.S.A.* **103**, 4493-4498.

Gaetz J, Gueroui Z, Libchaber A and Kapoor TM (2006). Examining how the spatial organization of chromatin signals influences metaphase spindle assembly. *Nat. Cell Biol.* **8**, 924-932.

Gall A, Treuting P, Elkon KB, Loo YM, Gale M, Barber GN and Stetson DB (2012). Autoimmunity initiates in nonhematopoietic cells and progresses via lymphocytes in an interferon-dependent autoimmune disease. *Immunity* **36**, 120-131.

Gant TM, Harris CA and Wilson KL (1999). Roles of LAP2 proteins in nuclear assembly and DNA replication: truncated LAP2beta proteins alter lamina assembly, envelope formation, nuclear size, and DNA replication efficiency in *Xenopus laevis* extracts. *J. Cell Biol.* **144**, 1083-1096.

Gao Y, Vainberg IE, Chow RL and Cowan NJ (1993). Two cofactors and cytoplasmic chaperonin are required for the folding of alpha- and beta-tubulin. *Mol. Cell. Biol.* **13**, 2478-2485.

Gardner MK, Zanic M, Gell C, Bormuth V and Howard J (2011). Depolymerizing kinesins Kip3 and MCAK shape cellular microtubule architecture by differential control of catastrophe. *Cell* **147**, 1092-1103.

Garner EC, Campbell CS and Mullins RD (2004). Dynamic instability in a DNA-segregating prokaryotic actin homolog. *Science* **306**, 1021-1025.

Ghenoiu C, Wheelock MS and Funabiki H (2013). Autoinhibition and polo-dependent multisite phosphorylation restrict activity of the histone H3 kinase haspin to mitosis. *Mol. Cell* **52**, 734-745.

Gisselsson D, Pettersson L, Höglund M, Heidenblad M, Gorunova L, Wiegant J, Mertens F, Dal Cin P, Mitelman F and Mandahl N (2000). Chromosomal breakage-fusion-bridge events cause genetic intratumor heterogeneity. *Proc. Natl. Acad. Sci. U.S.A.* **97**, 5357-5362.

Giunta S, Belotserkovskaya R and Jackson SP (2010). DNA damage signaling in response to double-strand breaks during mitosis. *J. Cell Biol.* **190**, 197-207.

Grigoriev I, Gouveia SM, Van Der Vaart B, Demmers J, Smyth JT, Honnappa S, Splinter D, Steinmetz MO, Putney JW, Hoogenraad CC and Akhmanova A (2008). STIM1 is a MT-plus-end-tracking protein involved in remodeling of the ER. *Curr. Biol.* **18**, 177-182.

Grivennikov SI, Greten FR and Karin M (2010). Immunity, inflammation, and cancer. *Cell* **140**, 883-899.

Groen AC, Coughlin ML and Mitchison TJ (2011). Microtubule assembly in meiotic extract requires glycogen. *Mol. Biol. Cell* **22**, 3139-3151.

Grozeva D, Carss K, Spasic-Boskovic O, Parker MJ, Archer H, Firth HV, Park SM, Canham N, Holder SE, Wilson M, Hackett A, Field M, Floyd JA, Consortium UK, Hurles M and Raymond FL (2014). De novo loss-of-function mutations in SETD5, encoding a methyltransferase in a 3p25 microdeletion syndrome critical region, cause intellectual disability. *Am. J. Human Genet.* **94**, 618-624.

Gruss OJ, Carazo-Salas RE, Schatz CA, Guarguaglini G, Kast J, Wilm M, Le Bot N, Vernos I, Karsenti E and Mattaj IW (2001). Ran induces spindle assembly by reversing the inhibitory effect of importin alpha on TPX2 activity. *Cell* **104**, 83-93.

Gupta ML, Carvalho P, Roof DM and Pellman D (2006). Plus end-specific depolymerase activity of Kip3, a kinesin-8 protein, explains its role in positioning the yeast mitotic spindle. *Nat. Cell Biol.* **8**, 913-923.

Haraguchi T, Kojidani T, Koujin T, Shimi T, Osakada H, Mori C, Yamamoto A and Hiraoka Y (2008). Live cell imaging and electron microscopy reveal dynamic processes of BAF-directed nuclear envelope assembly. *J. Cell Sci.* **121**, 2540-2554.

Harel A, Orjalo AV, Vincent T, Lachish-Zalait A, Vasu S, Shah S, Zimmerman E, Elbaum M and Forbes DJ (2003a). Removal of a single pore subcomplex results in vertebrate nuclei devoid of nuclear pores. *Mol. Cell* **11**, 853-864.

Harel A, Chan RC, Lachish-Zalait A, Zimmerman E, Elbaum M and Forbes DJ (2003b). Importin beta negatively regulates nuclear membrane fusion and nuclear pore complex assembly. *Mol. Biol. Cell* **14**, 4387-4396.

Harr JC, Luperchio TR, Wong X, Cohen E, Wheelan SJ and Reddy KL (2015). Directed targeting of chromatin to the nuclear lamina is mediated by chromatin state and A-type lamins. *J. Cell Biol.* **208**, 33-52.

Hartl P, Olson E, Dang T and Forbes DJ (1994). Nuclear assembly with lambda DNA in fractionated *Xenopus* egg extracts: an unexpected role for glycogen in formation of a higher order chromatin intermediate. *J. Cell Biol.* **124**, 235-248.

Hartman JJ, Mahr J, McNally KLP, Okawa K, Iwamatsu A, Thomas S, Cheesman S, Heuser J, Vale RD and McNally FJ (1998). Katanin, a microtubule-severing protein, is a novel AAA ATPase that targets to the centrosome using a WD40-containing subunit. *Cell* **93**, 277-287.

Hatch EM, Fischer AH, Deerinck TJ and Hetzer MW (2013). Catastrophic nuclear envelope collapse in cancer cell micronuclei. *Cell* **154**, 47-60.

Heald R, Tournebize R, Blank T, Sandaltzopoulos R, Becker PB, Hyman AA and Karsenti E (1996). Self-organization of microtubules into bipolar spindles around artificial chromosomes in Xenopus egg extracts. *Nature* **382**, 420-425.

Hetzer MW, Bilbao-Cortes D, Walther TC, Gruss OJ and Mattaj IW (2000). GTP hydrolysis by Ran is required for nuclear envelope assembly. *Mol. Cell* **5**, 1013-1024.

Hiraoka Y and Dernburg AF (2009). The SUN rises on meiotic chromosome dynamics. *Dev. Cell* **17**, 598-605.

Horio T and Hotani H (1986). Visualization of the dynamic instability of individual microtubules by dark-field microscopy. *Nature* **321**, 605-607.

Horner HA and Macgregor HC (1983). C value and cell volume: their significance in the evolution and development of amphibians. *J. Cell Sci.* **63**, 135-146.

Huang TT, Wuerzberger-Davis SM, Wu ZH and Miyamoto S (2003). Sequential modification of NEMO/IKKgamma by SUMO-1 and ubiquitin mediates NF-kappaB activation by genotoxic stress. *Cell* **115**, 565-576.

Hyman AA, Salser S, Drechsel DN, Unwin N and Mitchison TJ (1992). Role of GTP hydrolysis in microtubule dynamics: information from a slowly hydrolyzable analogue, GMPCPP. *Mol. Biol. Cell* **3**, 1155-1167.

Inoue A and Zhang Y (2014). Nucleosome assembly is required for nuclear pore complex assembly in mouse zygotes. *Nat. Struct. Mol. Biol.* **21**, 609-616.

Ishihara K, Nguyen PA, Groen AC, Field CM and Mitchison TJ (2014). Microtubule nucleation remote from centrosomes may explain how asters span large cells. *Proc. Natl. Acad. Sci. U.S.A.*

Ivanova N, Dobrin R, Lu R, Kotenko I, Levorse J, Decoste C, Schafer X, Lun Y and Lemischka IR (2006). Dissecting self-renewal in stem cells with RNA interference. *Nature* **442**, 533-538.

Jenkins TG and Carrell DT (2012). Dynamic alterations in the paternal epigenetic landscape following fertilization. *Frontiers Genet.* **3**, 143.

Jevtić P, Edens LJ, Vuković LD and Levy DL (2014). Sizing and shaping the nucleus: mechanisms and significance. *Curr. Opin. Cell Biol.* **28C**, 16-27.

John T, Caballero OL, Svobodová SJ, Kong A, Chua R, Browning J, Fortunato S, Deb S, Hsu M, Gedye CA, Davis ID, Altorki N, Simpson AJ, Chen Y-T, Monk M and Cebon JS (2008). ECSA/DPPA2 is an embryo-cancer antigen that is coexpressed with cancer-testis antigens in non-small cell lung cancer. *Clin. Cancer Res.* **14**, 3291-3298.

Johnson V, Ayaz P, Huddleston P and Rice LM (2011). Design, overexpression, and purification of polymerization-blocked yeast αβ-tubulin mutants. *Biochemistry* **50**, 8636-8644.

Jourdain L, Curmi P, Sobel A, Pantaloni D and Carlier MF (1997). Stathmin: a tubulin-sequestering protein which forms a ternary T2S complex with two tubulin molecules. *Biochemistry* **36**, 10817-10821.

Kaláb P, Weis K and Heald R (2002). Visualization of a Ran-GTP gradient in interphase and mitotic Xenopus egg extracts. *Science* **295**, 2452-2456.

Kaláb P and Heald R (2008). The RanGTP gradient - a GPS for the mitotic spindle. *J. Cell Sci.* **121**, 1577-1586.

Kay BK, Williamson MP and Sudol M (2000). The importance of being proline: the interaction of proline-rich motifs in signaling proteins with their cognate domains. *FASEB J.* **14**, 231-241.

Kelly AE, Sampath SC, Maniar TA, Woo EM, Chait BT and Funabiki H (2007). Chromosomal enrichment and activation of the Aurora B pathway are coupled to spatially regulate spindle assembly. *Dev. Cell* **12**, 31-43.

Kelly AE, Ghenoiu C, Xue JZ, Zierhut C, Kimura H and Funabiki H (2010). Survivin reads phosphorylated histone H3 threonine 3 to activate the mitotic kinase Aurora B. *Science* **330**, 235-239.

Khodjakov A, Cole RW, Oakley BR and Rieder CL (2000). Centrosome-independent mitotic spindle formation in vertebrates. *Curr. Biol.* **10**, 59-67.

Kim Y, Sharov AA, McDole K, Cheng M, Hao H, Fan C-M, Gaiano N, Ko MSH and Zheng Y (2011). Mouse B-type lamins are required for proper organogenesis but not by embryonic stem cells. *Science* **334**, 1706-1710.

Kind J, Pagie L, Ortabozkoyun H, Boyle S, de Vries SS, Janssen H, Amendola M, Nolen LD, Bickmore WA and van Steensel B (2013). Single-cell dynamics of genome-nuclear lamina interactions. *Cell* **153**, 178-192.

Kinoshita K, Arnal I, Desai A, Drechsel DN and Hyman AA (2001). Reconstitution of physiological microtubule dynamics using purified components. *Science* **294**, 1340-1343.

Kita K (2006). Adenomatous polyposis coli on microtubule plus ends in cell extensions can promote microtubule net growth with or without EB1. *Mol. Biol. Cell* **17**, 2331-2345.

Komarova Y, De Groot CO, Grigoriev I, Gouveia SM, Munteanu EL, Schober JM, Honnappa S, Buey RM, Hoogenraad CC, Dogterom M, Borisy GG, Steinmetz MO and Akhmanova A (2009). Mammalian end binding proteins control persistent microtubule growth. *J. Cell Biol.* **184**, 691-706.

Korn ED, Carlier MF and Pantaloni D (1987). Actin polymerization and ATP hydrolysis. *Science* **238**, 638-644.

Kuechler A, Zink AM, Wieland T, Lüdecke H, Cremer K, Salviati L, Magini P, Najafi K, Zweier C, Czeschik JC, Aretz S, Endele S, Tamburrino F, Pinato C, Clementi M, Gundlach J, Maylahn C, Mazzanti L, Wohlleber E, Schwarzmayr T, Kariminejad R, Schlessinger A, Wieczorek D, Strom TM, Novarino G and Engels H (2014). Loss-of-function variants of SETD5 cause intellectual disability and the core phenotype of microdeletion 3p25.3 syndrome. *Eur. J. Human Genet.*

Kuo AJ, Song J, Cheung P, Ishibe-Murakami S, Yamazoe S, Chen JK, Patel DJ and Gozani O (2012). The BAH domain of ORC1 links H4K20me2 to DNA replication licensing and Meier-Gorlin syndrome. *Nature* **484**, 115-119.

Lamichhane R, Solem A, Black W and Rueda D (2010). Single-molecule FRET of protein-nucleic acid and protein-protein complexes: surface passivation and immobilization. *Methods* **52**, 192-200.

Lan W, Zhang X, Kline-Smith SL, Rosasco-Nitcher SE, Barrett-Wilt GA, Shabanowitz J, Hunt DF, Walczak CE and Stukenberg PT (2004). Aurora B phosphorylates centromeric MCAK and regulates its localization and microtubule depolymerization activity. *Curr. Biol.* **14**, 273-286.

Larsson N, Segerman B, Gradin HM, Wandzioch E, Cassimeris L and Gullberg M (1999). Mutations of oncoprotein 18/stathmin identify tubulin-directed regulatory activities distinct from tubulin association. *Mol. Cell. Biol.* **19**, 2242-2250.

Laurell E, Beck K, Krupina K, Theerthagiri G, Bodenmiller B, Horvath P, Aebersold R, Antonin W and Kutay U (2011). Phosphorylation of Nup98 by multiple kinases is crucial for NPC disassembly during mitotic entry. *Cell* **144**, 539-550.

Lemaitre J-M, Géraud G and Méchali M (1998). Dynamics of the genome during early *Xenopus laevis* development: karyomeres as independent units of replication. *J. Cell Biol.* **142**, 1159-1166.

Levy DL and Heald R (2010). Nuclear size is regulated by importin α and Ntf2 in Xenopus. *Cell* **143**, 288-298.

Light WH, Freaney J, Sood V, Thompson A, D'Urso A, Horvath CM and Brickner JH (2013). A conserved role for human Nup98 in altering chromatin structure and promoting epigenetic transcriptional memory. *PLoS Biol.* **11**, e1001524.

Lints TJ, Parsons LM, Hartley L, Lyons I and Harvey RP (1993). Nkx-2.5: a novel murine homeobox gene expressed in early heart progenitor cells and their myogenic descendants. *Development* **119**, 419-431.

Lohka MJ and Masui Y (1983). Formation in vitro of sperm pronuclei and mitotic chromosomes induced by amphibian ooplasmic components. *Science* **220**, 719-721.

Loughlin R, Heald R and Nédélec FJ (2010). A computational model predicts *Xenopus* meiotic spindle organization. *J. Cell Biol.* **191**, 1239-1249.

Lourim D, Kempf A and Krohne G (1996). Characterization and quantitation of three B-type lamins in *Xenopus* oocytes and eggs: increase of lamin LI protein synthesis during meiotic maturation. *J. Cell Sci.* **109**, 1775-1785.

Lu L, Ladinsky MS and Kirchhausen T (2011). Formation of the postmitotic nuclear envelope from extended ER cisternae precedes nuclear pore assembly. *J. Cell Biol.* **194**, 425-440.

Lüke Y, Zaim H, Karakesisoglou I, Jaeger VM, Sellin L, Lu W, Schneider M, Neumann S, Beijer A, Munck M, Padmakumar VC, Gloy J, Walz G and Noegel AA (2008). Nesprin-2 Giant (NUANCE) maintains nuclear envelope architecture and composition in skin. *J. Cell Sci.* **121**, 1887-1898.

Luxton GWG, Gomes ER, Folker ES, Vintinner E and Gundersen GG (2010). Linear arrays of nuclear envelope proteins harness retrograde actin flow for nuclear movement. *Science* **329**, 956-959.

MacNeal RK and Purich DL (1978). Stoichiometry and role of GTP hydrolysis in bovine neurotubule assembly. *J. Biol. Chem.* **253**, 4683-4687.

Madan B, Madan V, Weber O, Tropel P, Blum C, Kieffer E, Viville S and Fehling HJ (2009). The pluripotency-associated gene Dppa4 is dispensable for embryonic stem cell identity and germ cell development but essential for embryogenesis. *Mol. Cell. Biol.* **29**, 3186-3203.

Maeshima K, Iino H, Hihara S, Funakoshi T, Watanabe A, Nishimura M, Nakatomi R, Yahata K, Imamoto F, Hashikawa T, Yokota H and Imamoto N (2010). Nuclear pore formation but not nuclear growth is governed by cyclin-dependent kinases (Cdks) during interphase. *Nat. Struct. Mol. Biol.* **17**, 1065-1071.

Makde RD, England JR, Yennawar HP and Tan S (2010). Structure of RCC1 chromatin factor bound to the nucleosome core particle. *Nature* **467**, 562-566.

Maldonado-Saldivia J, van den Bergen J, Krouskos M, Gilchrist MJ, Lee C, Li R, Sinclair AH, Surani MA and Western PS (2007). Dppa2 and Dppa4 are closely linked SAP motif genes restricted to pluripotent cells and the germ line. *Stem Cells* **25**, 19-28.

Margolis RL and Wilson L (1981). Microtubule treadmills--possible molecular machinery. *Nature* **293**, 705-711.

Masaki H, Nishida T, Sakasai R and Teraoka H (2010). DPPA4 modulates chromatin structure via association with DNA and core histone H3 in mouse embryonic stem cells. *Genes Cells* **15**, 327-337.

McGarry TJ and Kirschner MW (1998). Geminin, an inhibitor of DNA replication, is degraded during mitosis. *Cell* **93**, 1043-1053.

Meyerzon M, Gao Z, Liu J, Wu J-C, Malone CJ and Starr DA (2009). Centrosome attachment to the C. elegans male pronucleus is dependent on the surface area of the nuclear envelope. *Dev. Biol.* **327**, 433-446.

Minshull J, Sun H, Tonks NK and Murray AW (1994). A MAP kinase-dependent spindle assembly checkpoint in *Xenopus* egg extracts. *Cell* **79**, 475-486.

Mitchison TJ and Kirschner MW (1984a). Microtubule assembly nucleated by isolated centrosomes. *Nature* **312**, 232-237.

Mitchison TJ and Kirschner MW (1984b). Dynamic instability of microtubule growth. *Nature* **312**, 237-242.

Mitchison TJ, Wühr M, Nguyen PA, Ishihara K, Groen AC and Field CM (2012). Growth, interaction, and positioning of microtubule asters in extremely large vertebrate embryo cells. *Cytoskeleton* **69**, 738-750.

Moores CA, Yu M, Guo J, Beraud C, Sakowicz R and Milligan RA (2002). A mechanism for microtubule depolymerization by KinI kinesins. *Mol. Cell* **9**, 903-909.

Moores CA and Milligan RA (2008). Visualisation of a kinesin-13 motor on microtubule end mimics. *J. Mol. Biol.* **377**, 647-654.

Mora-Bermúdez F, Gerlich DW and Ellenberg J (2007). Maximal chromosome compaction occurs by axial shortening in anaphase and depends on Aurora kinase. *Nat. Cell Biol.* **9**, 822-831.

Murphy DB and Borisy GG (1975). Association of high-molecular-weight proteins with microtubules and their role in microtubule assembly in vitro. *Proc. Natl. Acad. Sci. U.S.A.* **72**, 2696-2700.

Murray AW and Kirschner MW (1989). Cyclin synthesis drives the early embryonic cell cycle. *Nature* **339**, 275-280.

Murray AW (1991). Cell cycle extracts. *Meth. Cell Biol.* **36**, 581-605.

Nachury MV, Maresca TJ, Salmon WC, Waterman-Storer CM, Heald R and Weis K (2001). Importin beta is a mitotic target of the small GTPase Ran in spindle assembly. *Cell* **104**, 95-106.

Nakamura T, Nakagawa M, Ichisaka T, Shiota A and Yamanaka S (2011). Essential roles of ECAT15-2/Dppa2 in functional lung development. *Mol. Cell. Biol.* **31**, 4366-4378.

Navarro-Lérida I, Pellinen T, Sanchez SA, Guadamillas MC, Wang Y, Mirtti T, Calvo E and Del Pozo MA (2015). Rac1 nucleocytoplasmic shuttling drives nuclear shape changes and tumor invasion. *Dev. Cell* **32**, 318-334.

Nemergut ME, Mizzen CA, Stukenberg PT, Allis CD and Macara IG (2001). Chromatin docking and exchange activity enhancement of RCC1 by histones H2A and H2B. *Science* **292**, 1540-1543.

Neumann FR and Nurse P (2007). Nuclear size control in fission yeast. *J. Cell Biol.* **179**, 593-600.

Neurohr G, Naegeli A, Titos I, Theler D, Greber B, Díez J, Gabaldón T, Mendoza M and Barral Y (2011). A midzone-based ruler adjusts chromosome compaction to anaphase spindle length. *Science* **332**, 465-468.

Nicklas RB (1983). Measurements of the force produced by the mitotic spindle in anaphase. *J. Cell Biol.* **97**, 542-548.

Niclas J, Allan VJ and Vale RD (1996). Cell cycle regulation of dynein association with membranes modulates microtubule-based organelle transport. *J. Cell Biol.* **133**, 585-593.

Niedenthal R (2009). Enhanced detection of in vivo SUMO conjugation by Ubc9 fusion-dependent sumoylation (UFDS). *Meth. Mol. Biol.* **497**, 63-79.

Ohsugi M, Adachi K, Horai R, Kakuta S, Sudo K, Kotaki H, Tokai-Nishizumi N, Sagara H, Iwakura Y and Yamamoto T (2008). Kid-mediated chromosome compaction ensures proper nuclear envelope formation. *Cell* **132**, 771-782.

Olins AL and Olins DE (2004). Cytoskeletal influences on nuclear shape in granulocytic HL-60 cells. *BMC Cell Biol.* **5**, 30.

Orthwein A, Fradet-Turcotte A, Noordermeer SM, Canny MD, Brun CM, Strecker J, Escribano-Diaz C and Durocher D (2014). Mitosis inhibits DNA double-strand break repair to guard against telomere fusions. *Science* **344**, 189-193.

Pajerowski JD, Dahl KN, Zhong FL, Sammak PJ and Discher DE (2007). Physical plasticity of the nucleus in stem cell differentiation. *Proc. Natl. Acad. Sci. U.S.A.* **104**, 15619-15624.

Pope BD, Ryba T, Dileep V, Yue F, Wu W, Denas O, Vera DL, Wang Y, Hansen RS, Canfield TK, Thurman RE, Cheng Y, Gülsoy G, Dennis JH, Snyder MP,

Stamatoyannopoulos JA, Taylor J, Hardison RC, Kahveci T, Ren B and Gilbert DM (2014). Topologically associating domains are stable units of replication-timing regulation. *Nature* **515**, 402-405.

Postow L, Ghenoiu C, Woo EM, Krutchinsky AN, Chait BT and Funabiki H (2008). Ku80 removal from DNA through double strand break-induced ubiquitylation. *J. Cell Biol.* **182**, 467-479.

Ramadan K, Bruderer R, Spiga FM, Popp O, Baur T, Gotta M and Meyer HH (2007). Cdc48/p97 promotes reformation of the nucleus by extracting the kinase Aurora B from chromatin. *Nature* **450**, 1258-1262.

Ravelli RBG, Gigant B, Curmi PA, Jourdain I, Lachkar S, Sobel A and Knossow M (2004). Insight into tubulin regulation from a complex with colchicine and a stathmin-like domain. *Nature* **428**, 198-202.

Reber SB, Over S, Kronja I and Gruss OJ (2008). CaM kinase II initiates meiotic spindle depolymerization independently of APC/C activation. *J. Cell Biol.* **183**, 1007-1017.

Richards A (1917). The history of the chromosomal vesicles in Fundulus and the theory of genetic continuity of chromosomes. *Biol. Bull.* **32**, 249.

Rodionov VI and Borisy GG (1997). Microtubule treadmilling in vivo. *Science* **275**, 215-218.

Roll-Mecak A and Vale RD (2005). The *Drosophila* homologue of the hereditary spastic paraplegia protein, spastin, severs and disassembles microtubules. *Curr. Biol.* **15**, 650-655.

Rowat AC, Jaalouk DE, Zwerger M, Ung WL, Eydelnant IA, Olins DE, Olins AL, Herrmann H, Weitz DA and Lammerding J (2013). Nuclear envelope composition determines the ability of neutrophil-type cells to passage through micron-scale constrictions. *J. Biol. Chem.* **288**, 8610-8618.

Roychowdhury S, Panda D, Wilson L and Rasenick MM (1999). G protein alpha subunits activate tubulin GTPase and modulate microtubule polymerization dynamics. *J. Biol. Chem.* **274**, 13485-13490.

Rual J, Venkatesan K, Hao T, Hirozane-Kishikawa T, Dricot A, Li N, Berriz GF, Gibbons FD, Dreze M, Ayivi-Guedehoussou N, Klitgord N, Simon C, Boxem M, Milstein S, Rosenberg J, Goldberg DS, Zhang LV, Wong SL, Franklin G, Li S, Albala JS, Lim J, Fraughton C, Llamosas E, Cevik S, Bex C, Lamesch P, Sikorski RS, Vandenhaute J, Zoghbi HY, Smolyar A, Bosak S, Sequerra R, Doucette-Stamm L, Cusick ME, Hill DE, Roth FP and Vidal M (2005). Towards a proteome-scale map of the human protein-protein interaction network. *Nature* **437**, 1173-1178.

Salina D, Bodoor K, Eckley DM, Schroer TA, Rattner JB and Burke B (2002). Cytoplasmic dynein as a facilitator of nuclear envelope breakdown. *Cell* **108**, 97-107.

Sampath SC, Ohi R, Leismann O, Salic A, Pozniakovsky A and Funabiki H (2004). The chromosomal passenger complex is required for chromatin-induced microtubule stabilization and spindle assembly. *Cell* **118**, 187-202.

Sato A, Isaac B, Phillips CM, Rillo R, Carlton PM, Wynne DJ, Kasad RA and Dernburg AF (2009). Cytoskeletal forces span the nuclear envelope to coordinate meiotic chromosome pairing and synapsis. *Cell* **139**, 907-919.

Scaffidi P and Misteli T (2006). Lamin A-dependent nuclear defects in human aging. *Science* **312**, 1059-1063.

Scaffidi P and Misteli T (2008). Lamin A-dependent misregulation of adult stem cells associated with accelerated ageing. *Nat. Cell Biol.* **10**, 452-459.

Schlaitz A-L, Thompson J, Wong CCL, Yates JR and Heald R (2013). REEP3/4 ensure endoplasmic reticulum clearance from metaphase chromatin and proper nuclear envelope architecture. *Dev. Cell* **26**, 315-323.

Shiina N, Gotoh Y, Kubomura N, Iwamatsu A and Nishida E (1994). Microtubule severing by elongation factor 1 alpha. *Science* **266**, 282-285.

Siegel D, Schuff M, Oswald F, Cao Y and Knöchel W (2009). Functional dissection of XDppa2/4 structural domains in *Xenopus* development. *Mech. Dev.* **126**, 974-989.

Smyth JT, Beg AM, Wu S, Putney JW and Rusan NM (2012). Phosphoregulation of STIM1 leads to exclusion of the endoplasmic reticulum from the mitotic spindle. *Curr. Biol.* **22**, 1487-1493.

Song L and Rape M (2010). Regulated degradation of spindle assembly factors by the anaphase-promoting complex. *Mol. Cell* **38**, 369-382.

Song L, Craney A and Rape M (2014). Microtubule-dependent regulation of mitotic protein degradation. *Mol. Cell* **53**, 179-192.

Sosa BA, Rothballer A, Kutay U and Schwartz TU (2012). LINC Complexes Form by Binding of Three KASH Peptides to Domain Interfaces of Trimeric SUN Proteins. *Cell* **149**, 1035-1047.

Stead E, White J, Faast R, Conn S, Goldstone S, Rathjen J, Dhingra U, Rathjen P, Walker D and Dalton S (2002). Pluripotent cell division cycles are driven by ectopic Cdk2, cyclin A/E and E2F activities. *Oncogene* **21**, 8320-8333.

Stephens PJ, Greenman CD, Fu B, Yang F, Bignell GR, Mudie LJ, Pleasance ED, Lau KW, Beare D, Stebbings LA, McLaren S, Lin M-L, Mcbride DJ, Varela I, Nik-Zainal SA, Leroy C, Jia M, Menzies A, Butler AP, Teague JW, Quail MA, Burton J, Swerdlow H, Carter NP, Morsberger LA, Iacobuzio-Donahue CA, Follows GA, Green AR, Flanagan AM, Stratton MR, Futreal PA and Campbell PJ (2011). Massive genomic

rearrangement acquired in a single catastrophic event during cancer development. *Cell* **144**, 27-40.

Stetson DB, Ko JS, Heidmann T and Medzhitov R (2008). Trex1 prevents cell-intrinsic initiation of autoimmunity. *Cell* **134**, 587-598.

Subbotin RI and Chait BT (2014). A pipeline for determining protein–protein interactions and proximities in the cellular milieu. *Mol. Cell. Proteomics* **13**, 2824-2835.

Suzuki R, Shindo H, Tase A, Kikuchi Y, Shimizu M and Yamazaki T (2009). Solution structures and DNA binding properties of the N-terminal SAP domains of SUMO E3 ligases from *Saccharomyces cerevisiae* and *Oryza sativa*. *Proteins* **75**, 336-347.

Tan L and Kapoor TM (2011). Examining the dynamics of chromosomal passenger complex (CPC)-dependent phosphorylation during cell division. *Proc. Natl. Acad. Sci. U.S.A.* **108**, 16675-16680.

Theerthagiri G, Eisenhardt N, Schwarz H and Antonin W (2010). The nucleoporin Nup188 controls passage of membrane proteins across the nuclear pore complex. *J. Cell Biol.* **189**, 1129-1142.

Tran PT, Walker RA and Salmon ED (1997). A metastable intermediate state of microtubule dynamic instability that differs significantly between plus and minus ends. *J. Cell Biol.* **138**, 105-117.

Tropini C, Roth EA, Zanic M, Gardner MK and Howard J (2012). Islands containing slowly hydrolyzable GTP analogs promote microtubule rescues. *PLoS One* **7**, e30103.

Tseng BS, Tan L, Kapoor TM and Funabiki H (2010). Dual detection of chromosomes and microtubules by the chromosomal passenger complex drives spindle assembly. *Dev. Cell* **18**, 903-912.

Tung P-Y, Varlakhanova NV and Knoepfler PS (2013). Identification of DPPA4 and DPPA2 as a novel family of pluripotency-related oncogenes. *Stem Cell* **31**, 2330-2342.

Turgay Y, Champion L, Balazs C, Held M, Toso A, Gerlich DW, Meraldi P and Kutay U (2014). SUN proteins facilitate the removal of membranes from chromatin during nuclear envelope breakdown. *J. Cell Biol.* **204**, 1099-1109.

Varga V, Helenius J, Tanaka K, Hyman AA, Tanaka TU and Howard J (2006). Yeast kinesin-8 depolymerizes microtubules in a length-dependent manner. *Nat. Cell Biol.* **8**, 957-962.

Verde F, Labbé J-C, Dorée M and Karsenti E (1990). Regulation of microtubule dynamics by cdc2 protein kinase in cell-free extracts of *Xenopus* eggs. *Nature* **343**, 233-238.

Walczak CE and Heald R (2008). Mechanisms of mitotic spindle assembly and function. *Int. Rev. Cytol.* **265**, 111-158.

Walker RA, O'brien ET, Pryer NK, Soboeiro MF, Voter WA, Erickson HP and Salmon ED (1988). Dynamic instability of individual microtubules analyzed by video light microscopy: rate constants and transition frequencies. *J. Cell Biol.* **107**, 1437-1448.

Walker RA, Inoué S and Salmon ED (1989). Asymmetric behavior of severed microtubule ends after ultraviolet-microbeam irradiation of individual microtubules in vitro. *J. Cell Biol.* **108**, 931-937.

Walther TC, Alves A, Pickersgill H, Loïodice I, Hetzer MW, Galy V, Hülsmann BB, Köcher T, Wilm M, Allen TD, Mattaj IW and Doye V (2003a). The conserved Nup107-160 complex is critical for nuclear pore complex assembly. *Cell* **113**, 195-206.

Walther TC, Askjaer P, Gentzel M, Habermann A, Griffiths G, Wilm M, Mattaj IW and Hetzer MW (2003b). RanGTP mediates nuclear pore complex assembly. *Nature* **424**, 689-694.

Wang F, Dai J, Daum JR, Niedzialkowska E, Banerjee B, Stukenberg PT, Gorbsky GJ and Higgins JMG (2010). Histone H3 Thr-3 phosphorylation by Haspin positions Aurora B at centromeres in mitosis. *Science* **330**, 231-235.

Wang H-W and Nogales E (2005). Nucleotide-dependent bending flexibility of tubulin regulates microtubule assembly. *Nature* **435**, 911-915.

Wang S, Romano FB, Field CM, Mitchison TJ and Rapoport TA (2013). Multiple mechanisms determine ER network morphology during the cell cycle in *Xenopus* egg extracts. *J. Cell Biol.* **203**, 801-814.

Watanabe N, Hunt T, Ikawa Y and Sagata N (1991). Independent inactivation of MPF and cytostatic factor (Mos) upon fertilization of *Xenopus* eggs. *Nature* **352**, 247-248.

Waterman-Storer CM and Salmon ED (1998). Endoplasmic reticulum membrane tubules are distributed by microtubules in living cells using three distinct mechanisms. *Curr. Biol.* **8**, 798-806.

Wiese C, Wilde A, Moore MS, Adam SA, Merdes A and Zheng Y (2001). Role of importin-beta in coupling Ran to downstream targets in microtubule assembly. *Science* **291**, 653-656.

Wittmann T and Hyman AA (1999). Recombinant p50/dynamitin as a tool to examine the role of dynactin in intracellular processes. *Meth. Cell Biol.* **61**, 137-143.

Woo EM (2010). Characterization of a novel chromatin-induced mechanism that couples microtubule disassembly and nuclear re-formation. Ph.D. Thesis. The Rockefeller University (New York).

Woolner S, Miller AL and Bement WM (2009). Imaging the cytoskeleton in live Xenopus laevis embryos. *Meth. Mol. Biol.* **586**, 23-39.

Wright SJ (1999). Sperm nuclear activation during fertilization. *Curr. Top. Dev. Biol.* **46**, 133-178.

Wühr M, Chen Y, Dumont S, Groen AC, Needleman DJ, Salic A and Mitchison TJ (2008). Evidence for an upper limit to mitotic spindle length. *Curr. Biol.* **18**, 1256-1261.

Wühr M, Dumont S, Groen AC, Needleman DJ and Mitchison TJ (2009). How does a millimeter-sized cell find its center? *Cell Cycle* **8**, 1115-1121.

Wühr M, Tan ES, Parker SK, Detrich HW and Mitchison TJ (2010). A model for cleavage plane determination in early amphibian and fish embryos. *Curr. Biol.* **20**, 2040-2045.

Wurzenberger C and Gerlich DW (2011). Phosphatases: providing safe passage through mitotic exit. *Nat. Rev. Mol. Cell Biol.* **12**, 469-482.

Wynne DJ, Rog O, Carlton PM and Dernburg AF (2012). Dynein-dependent processive chromosome motions promote homologous pairing in *C. elegans* meiosis. *J. Cell Biol.* **196**, 47-64.

Xue B, Dunbrack RL, Williams RW, Dunker AK and Uversky VN (2010). PONDR-FIT: a meta-predictor of intrinsically disordered amino acids. *Biochim. Biophys. Acta* **1804**, 996-1010.

Xue JZ, Woo EM, Postow L, Chait BT and Funabiki H (2013). Chromatin-bound *Xenopus* Dppa2 shapes the nucleus by locally inhibiting microtubule assembly. *Dev. Cell* **27**, 47-59.

Xue JZ and Funabiki H (2014). Nuclear assembly shaped by microtubule dynamics. *Nucleus* **5**, 40-46.

Yamagishi Y, Honda T, Tanno Y and Watanabe Y (2010). Two histone marks establish the inner centromere and chromosome bi-orientation. *Science* **330**, 239-243.

Yamamoto A, West RR, McIntosh JR and Hiraoka Y (1999). A cytoplasmic dynein heavy chain is required for oscillatory nuclear movement of meiotic prophase and efficient meiotic recombination in fission yeast. *J. Cell Biol.* **145**, 1233-1249.

Yarden A and Geiger B (1996). Zebrafish cyclin E regulation during early embryogenesis. *Dev. Dyn.* **206**, 1-11.

Zhang C and Clarke PR (2000). Chromatin-independent nuclear envelope assembly induced by Ran GTPase in *Xenopus* egg extracts. *Science* **288**, 1429-1432.

Zierhut C, Jenness C, Kimura H and Funabiki H (2014). Nucleosomal regulation of chromatin composition and nuclear assembly revealed by histone depletion. *Nat. Struct. Mol. Biol.* **21**, 617-625.